OULU 2012
C 423

ACTA UNIVERSITATIS OULUENSIS

Johanna Ketonen

EQUALIZATION AND CHANNEL ESTIMATION ALGORITHMS AND IMPLEMENTATIONS FOR CELLULAR MIMO-OFDM DOWNLINK

UNIVERSITY OF OULU GRADUATE SCHOOL;
UNIVERSITY OF OULU, FACULTY OF TECHNOLOGY,
DEPARTMENT OF COMMUNICATIONS ENGINEERING;
CENTRE FOR WIRELESS COMMUNICATIONS;
INFOTECH OULU

ACTA UNIVERSITATIS OULUENSIS
C Technica 423

JOHANNA KETONEN

EQUALIZATION AND CHANNEL ESTIMATION ALGORITHMS AND IMPLEMENTATIONS FOR CELLULAR MIMO-OFDM DOWNLINK

Academic dissertation to be presented with the assent of the Doctoral Training Committee of Technology and Natural Sciences of the University of Oulu for public defence in OP-sali (Auditorium L10), Linnanmaa, on 27 June 2012, at 1 p.m.

UNIVERSITY OF OULU, OULU 2012

Acta Univ. Oul. C 423, 2012

Supervised by
Professor Markku Juntti
Docent Joseph R. Cavallaro

Reviewed by
Associate Professor Mark C. Reed
Associate Professor Ahmed Eltawil

ISBN 978-951-42-9856-1 (Paperback)
ISBN 978-951-42-9857-8 (PDF)

ISSN 0355-3213 (Printed)
ISSN 1796-2226 (Online)

Cover Design
Raimo Ahonen

JUVENES PRINT
TAMPERE 2012

Ketonen, Johanna, Equalization and channel estimation algorithms and implementations for cellular MIMO-OFDM downlink.
University of Oulu Graduate School; University of Oulu, Faculty of Technology, Department of Communications Engineering; Centre for Wireless Communications; Infotech Oulu, P.O. Box 4500, FI-90014 University of Oulu, Finland
Acta Univ. Oul. C 423, 2012
Oulu, Finland

Abstract

The aim of the thesis is to develop algorithms and architectures to meet the high data rate, low complexity requirements of the future mobile communication systems. Algorithms, architectures and implementations for detection, channel estimation and interference mitigation in the multiple-input multiple-output (MIMO) orthogonal frequency division multiplexing (OFDM) receivers are presented. The performance-complexity trade-offs in different receiver algorithms are studied and the results can be utilized in receiver design as well as in system design.

Implementation of detectors for spatial multiplexing systems is considered first. The linear minimum mean squared error (LMMSE) and the K-best list sphere detector (LSD) are compared to the successive interference cancellation (SIC) detector. The SIC algorithm was found to perform worse than the K-best LSD when the MIMO channels are highly correlated. The performance difference diminishes when the correlation decreases. With feedback to the transmitter, the performance difference is even smaller, but the full rank transmissions still require a more complex detector. A reconfigurable receiver, using a simple or a more complex detector as the channel conditions change, would achieve the best performance while consuming the least amount of power in the receiver.

The use of decision directed (DD) channel estimation is also studied. The 3GPP long term evolution (LTE) based pilot structure is used as a benchmark. The performance and complexity of the pilot symbol based least-squares (LS) channel estimator, the minimum mean square error (MMSE) filter and the DD space-alternating generalized expectation-maximization (SAGE) algorithm are studied. DD channel estimation and MMSE filtering improve the performance with high user velocities, where the pilot symbol density is not sufficient. With DD channel estimation, the pilot overhead can be reduced without any performance degradation by transmitting data instead of pilot symbols.

Suppression of co-channel interference in the MIMO-OFDM receiver is finally considered. The interference and noise spatial covariance matrix is used in data detection and channel estimation. Interference mitigation is applied for linear and nonlinear detectors. An algorithm to adapt the accuracy of the matrix decomposition and the use of interference suppression is proposed. The adaptive algorithm performs well in all interference scenarios and the power consumption of the receiver can be reduced.

Keywords: channel estimation, detection, interference mitigation, LSD, MIMO, OFDM

Ketonen, Johanna, Korjain- ja kanavaestimointialgoritmit ja niiden toteutukset MIMO-OFDM-solukkoalalinkissä.
Oulun yliopiston tutkijakoulu; Oulun yliopisto, Teknillinen tiedekunta, Tietoliikennetekniikan osasto; Centre for Wireless Communications; Infotech Oulu, PL 4500, 90014 Oulun yliopisto
Acta Univ. Oul. C 423, 2012
Oulu

Tiivistelmä

Tämän väitöskirjatyön tavoitteena on kehittää vastaanotinalgoritmeja ja -arkkitehtuureja, jotka toteuttavat tulevaisuuden langattomien tietoliikennejärjestelmien suuren datanopeuden ja pienen kompleksisuuden tavoitteet. Työssä esitellään algoritmeja, arkkitehtuureja ja toteutuksia ilmaisuun, kanavaestimointiin ja häiriönvaimennukseen monitulo-monilähtötekniikkaa (multiple-input multiple-output, MIMO) ja ortogonaalista taajuusjakokanavointia (orthogonal frequency division multiplexing, OFDM) yhdistäviin vastaanottimiin. Algoritmeista saatavaa suorituskyky-hyötyä verrataan vaadittavaan toteutuksen monimutkaisuuteen. Työn tuloksia voidaan hyödyntää sekä vastaanotin- että järjestelmäsuunnittelussa.

Lineaarista pienimmän keskineliövirheen (minimum mean square error, MMSE) ilmaisinta ja listapalloilmaisinta (list sphere detector, LSD) verrataan peräkkäiseen häiriönpoistoilmaisimeen (successive interference cancellation, SIC). SIC-ilmaisimella on huonompi suorituskyky kuin LSD-ilmaisimella radiokanavan ollessa korreloitunut. Korrelaation pienentyessä myös ilmaisimien suorituskykyero pienenee. Erot suorituskyvyissä ovat vähäisiä silloinkin, jos järjestelmässä on takaisinkytkentäkanava lähettimelle. Tällöinkin korkean signaali-kohinasuhteen olosuhteissa LSD-ilmaisimet mahdollistavat tilakanavoidun, suuren datanopeuden tiedonsiirron. Radiokanavan muuttuessa uudelleenkonfiguroitava vastaanotin toisi virransäästömahdollisuuden vaihtelemalla kompleksisen ja yksinkertaisen ilmaisimen välillä.

Kanavaestimointialgoritmeja ja niiden toteutuksia vertaillaan käyttämällä lähtökohtana nykyisen mobiilin tiedonsiirtostandardin viitesignaalimallia. Tutkittavat algoritmit perustuvat pienimmän neliösumman (least squares, LS) ja pienimmän keskineliövirheen menetelmään, sekä päätöstakaisinkytkettyyn (decision directed, DD) kanavaestimointialgoritmiin. DD-kanavaestimaattori ja MMSE-suodatin parantavat vastaanottimen suorituskykyä korkeissa käyttäjän nopeuksissa, joissa viitesignaaleiden tiheys ei ole riittävä. DD-kanavaestimoinnilla datanopeutta voidaan nostaa viitesignaaleiden määrää laskemalla vaikuttamatta suorituskykyyn.

Työssä tarkastellaan myös saman kanavan häiriön vaimennusta. Häiriöstä ja kohinasta koostuvaa kovarianssimatriisia käytetään ilmaisuun ja kanavaestimointiin. Työssä esitetään adaptiivinen algoritmi matriisihajoitelman tarkkuuden ja häiriön vaimennuksen säätämiseen. Algoritmi mahdollistaa hyvän suorituskyvyn kaikissa häiriötilanteissa vähentäen samalla virrankulutusta.

Asiasanat: häiriön vaimennus, ilmaisin, kanavaestimointi, LSD, MIMO, OFDM

Preface

The research for this thesis has been carried out at the Centre for Wireless Communications (CWC) and the Department of Communications Engineering, University of Oulu, Finland. First of all, I want to thank Professor Matti Latva-aho, and Lic. Tech. Ari Pouttu, the directors of CWC during my stay, for giving me the opportunity to work in the inspiring working environment.

I would also like to thank my supervisor, Professor Markku Juntti, for his invaluable guidance and support and for the possibility to start my postgraduate research which has greatly benefitted from his technical precision and high research standards. I would also like to thank Professor Joseph R. Cavallaro for his supervision and for the opportunity to go on research visits to Rice University, USA. I would like to express my gratitude to the reviewers of this thesis Associate Professor Ahmed Eltawil from the University of California, Irvine, USA and Associate Professor (Adjunct) Mark Reed from the Australian National University, Canberra, Australia. Their comments significantly improved the quality of the thesis. Dr. Pertti Väyrynen is acknowledged for proofreading the manuscript as well.

The work presented in this thesis was carried out in the MIMO Techniques for 3G System and Standard Evolution (MITSE) and Cooperative MIMO Techniques for Cellular System Evolution (CoMIT) projects. I would like to thank the project manager of these projects, Lic. Tech Visa Tapio, and my colleagues in those projects. I would also like to thank the technical steering group members of the projects for their helpful comments. I am grateful to my co-authors Dr. Markus Myllylä, Dr. Jari Ylioinas, Dr. Janne Janhunen, Dr. Juha Karjalainen and Tuomo Hänninen for the fruitful co-operation. I would also like to thank my colleagues for the traveling company and for the discussions and inspiring working environment. Special thanks go to Essi Suikkanen, my office mate for six years, for her friendship and support in the research work. The administrative support of Antero Kangas, Elina Komminaho, Sari Luukkonen, Kirsi Ojutkangas, Eija Pajunen, Hanna Saarela, Jari Sillanpää and Timo Äikäs is also appreciated.

The research for this thesis has been financially supported by Infotech Oulu Doctoral Program during 2010-2012. Funding through the projects was provided by the Finnish Funding Agency for Technology and Innovation, Elektrobit, Nokia, Nokia Siemens

Networks, Texas Instruments, Renesas Mobile Europe, Uninord, Xilinx and the Academy of Finland, which is gratefully acknowledged. I was privileged to receive personal grants for Doctoral studies from the following Finnish foundations: Nokia Foundation, Oulun yliopiston tukisäätiö and Tauno Tönningin säätiö. These acknowledgements encouraged me to go on with my research work and they are gratefully recognized.

My deepest gratitude goes to my parents Maarit and Kari for their support and encouragement. I would also like to thank my baby for the figurative and literal kicks towards completing the thesis. My warmest thanks belong to my husband Ilkka for his love and companionship.

Oulu, June, 2012 Johanna Ketonen

Symbols and Abbreviations

$\lvert\cdot\rvert$	absolute value
$(\cdot)^*$	complex conjugate
$\hat{(\cdot)}$	estimate of variable
$\lvert\lvert\cdot\rvert\rvert$	Euclidean norm
$(\cdot)^{\mathrm{H}}$	Hermitian transpose
$(\cdot)^{-1}$	inverse
$(\cdot)^{+}$	Moore-Penrose pseudo-inverse
$(\cdot)^{\dagger}$	pseudo-inverse
$\sqrt{(\cdot)}$	square root
$\otimes$	Kronecker product
$d(\cdot)$	distance
$\det(\cdot)$	determinant
$\mathrm{diag}(\cdot)$	diagonal values of matrix
$E(\cdot)$	expectation of the argument
$e_i(\cdot)$	PED on the ith level in SSFE
$exp(\cdot)$	exponent function
$\mathrm{Im}\{\cdot\}$	imaginary part of the argument
$\mathrm{jacln}(\cdot)$	Jacobian logarithm of the argument
$J_0(\cdot)$	the zeroth-order Bessel function of the first kind
$\ln(\cdot)$	natural logarithm
$\log_2(\cdot)$	base 2 logarithm
$\max(x,y)$	maximum of the arguments
$\min(x,y)$	minimum of the arguments
$p(\cdot)$	likelihood function
$Pr(\cdot)$	probability
$r(\cdot)$	a refinement term
$\mathrm{Re}\{\cdot\}$ or $\{\cdot\}_{re}$	real part of the argument

$\mathbb{C}$	complex plane
δ_m	m dominant eigenvalues
ε	metric for constellation point selection in SSFE

Γ	diagonal matrix with noise variance estimates
γ_j	instantaneous SINR
γ_k	metric for layer selection in SIC detection
γ_{m_R}	noise variance estimate on m_Rth receive antenna
η_{c}	noise vector
κ	ratio of the maximum eigenvalue to the sum of all eigenvalues
Λ	LLR bit metric
λ	wave length
Ω	set of all possible transmitted symbols
Ψ	reduced covariance matrix
ρ_i	signal-to-interference-noise ratio on the ith stream
$\rho(n-n')$	temporal correlation between the channel taps at times n and n'
$\mathbb{R}$	real plane
Σ	diagonal matrix from SVD
$\Sigma^{-1}_{\hat{\mathbf{h}}^{\mathrm{LS}}_{m_R,m_T,l}}$	the cross-covariance matrix between $h_{m_R,m_T,l(n)}$ and $\hat{\mathbf{h}}^{\mathrm{LS}}_{m_R,m_T,l}$
$\Sigma^{\mathrm{H}}_{m_R,m_T,l}$	auto-covariance matrix of $h_{m_R,m_T,l(n)}$
Σ_w	noise covariance matrix
σ^2	noise variance
ς_i	ith singular value
B	bandwidth
B_f	length of MMSE filtering window
$\mathbf{B}$	diagonal matrix for removing LMMSE bias
$\mathbf{B}_d$	the off-diagonal elements of $\mathbf{D}$
$\mathbf{b}$	transmitted binary vector
$\mathbb{B}_{k,\pm 1}$	the set of 2^{NQ-1} bit vectors having $b_k = \pm 1$
b_k	the kth transmitted bit
$\mathbf{b}_{[k]}$	subvector of $\mathbf{b}$ without its kth element
$\mathbf{b}_p$	binary vector on pth subcarrier corresponding to the transmitted symbol
c	speed of light
C	channel capacity
C_0	sphere radius
$\mathbf{C}_{RX}$	receiver spatial correlation matrix
$\mathbf{C}_{TX}$	transmitter spatial correlation matrix

d	distance
D_{det}	latency of the detector
D_{dec}	latency of the decoder
D_{rec}	latency of the receiver
$\mathbf{D}$	diagonal matrix of eigenvalues
$\mathbf{D}_R$	diagonal matrix with diagonals of $\mathbf{R}$
$\mathbf{D}_U$	diagonal matrix with squared diagonals of $\mathbf{R}$
E_s	power spectral density of received signal
$E\{x\}$	symbol expectation
$\mathbf{F}$	the DFT matrix
$\mathbf{F}_k$	kth row of the truncated Fourier matrix
$\overline{\mathbf{F}}$	$NP \times NL$ matrix from the DFT matrix
f_c	center frequency
f_{clock}	clock frequency
f_d	Doppler frequency
$\mathbf{G}$	matrix to be inverted in LMMSE filter calculation
$\mathbf{H}$	channel matrix on any subcarrier
$\underline{\underline{\mathbf{H}}}$	extended channel matrix
$\hat{\mathbf{H}}$	channel estimate
$\mathbf{H}_e$	equivalent channel matrix
$\mathbf{H}_k$	matrix $\mathbf{H}$ with the vectors from previously detected layers removed
$\mathbf{H}_p$	channel matrix on pth subcarrier
$\mathbf{h}_k$	kth vector from matrix $\mathbf{H}$
$\underline{\mathbf{h}}_i$	ith column of matrix $\underline{\underline{\mathbf{H}}}$
$\hat{h}^{(i)}_{m_T,m_R,l}(n)$	channel estimate on the ith iteration for lth tap and m_T, m_Rth antennas
$\hat{\mathbf{h}}^{\mathrm{LS}}_{m_R}(n)$	LS channel estimate for the m_Rth receive antenna at time index n
$\hat{\mathbf{h}}^{\mathrm{LS}}_{m_R,m_T,l}$	the LS channel estimate for the lth tap and m_T, m_Rth antennas
$\hat{\mathbf{h}}^{\mathrm{MMSE}}_{m_R,m_T,l}(n)$	MMSE channel estimate for the m_Rth receive antenna at time index n
$\mathbf{h}_{m_R}$	the time domain channel vector from the transmit antennas to the m_Rth receive antenna
$\mathbf{I}_M$	identity matrix with dimensions of number of receive antennas
$\mathbf{I}_N$	identity matrix with dimensions of number of transmit antennas
$\mathbf{i}_{m_R}$	vector containing interference plus identically distributed complex white Gaussian noise
k	Boltzmann's constant
K	the list size of the tree search detector
L	length of the channel impulse response

$\mathscr{L}$	list of candidates
$\mathscr{L}_{k,\pm 1}$	subset of $\mathbb{B}_{k,\pm 1}$ where $b_k = \pm 1$
L_A	the *a priori* information
L_{A1}	the *a priori* information at the detector input
L_{A2}	the *a priori* information at the decoder input
$\mathbf{L}_{A,[k]}$	L_A values corresponding to $\mathbf{b}$, excluding the value for b_k
L_D	the *a posteriori* information
L_{D1}	the *a posteriori* information at the detector output
L_{D2}	the *a posteriori* information at the decoder output
L_E	the extrinsic information
L_{E1}	the extrinsic information after the detector
L_{E2}	the extrinsic information after the decoder
L_F	free space path loss
LLR_k	log-likelihood ratio if bit k
M	number of receive antennas
$\mathbf{m}$	SSFE node spanning vector
m_R	receive antenna index
m_T	transmit antenna index
N	number of transmit antennas
N_{iter}	number of receiver iterations
N_0	power spectral density of the AWGN process
N_{cand}	size of the output list of a list sphere detector
N_P	number of OFDM symbols with pilot symbols in an MMSE filtering window
N_R	receiver noise floor
N_r	number of pilot symbols
N_s	number of RAM bits used by a state machine
$\mathbf{o}$	time domain received signal
P	number of subcarriers
Q	number of bits per symbol
$\mathbf{Q}$	matrix with orthogonal columns
$\mathbf{Q}_i$	spatial covariance matrix of interference
$\mathbf{Q}_A$	matrix result from SGR
$\underline{\mathbf{Q}}$	extended matrix with orthogonal columns
$\underline{\mathbf{q}}_i$	ith column of matrix $\underline{\mathbf{Q}}$
$\mathbf{R}$	upper triangular matrix with positive diagonal elements

$\underline{\mathbf{R}}$	upper triangular matrix with positive diagonal elements from QRD with extended matrix
$\underline{r}_{i,j}$	i, j element of matrix $\underline{\mathbf{R}}$
$\mathbf{r}$	received signal vector
S	constellation point in symbol expectation calculation
S_i	number of SAGE iterations
T	temperature
T_B	OFDM symbol duration
tp_c	throughput clock cycles
T_r	training period
$\mathbf{U}$	unitary matrix from SVD
$\mathbf{U}_R$	upper triangular matrix from SGR
v	velocity
$\mathbf{V}$	unitary matrix from SVD
$\mathbf{V}_m$	eigenvectors for m dominant eigenvalues
$\mathbf{W}$	LMMSE filter coefficient matrix
$\mathbf{W}_{m_R,m_T,l}(n)$	the MMSE filter for the lth tap from the m_Tth transmit antenna to the m_Rth receive antenna
$\mathbf{w}$	circularly symmetric complex Gaussian distributed noise
$\mathbf{X}(n)$	transmitted signal over P subcarriers and N transmit antennas
$\mathbf{x}$	transmitted signal on any subcarrier
x_l	lth constellation point in Ω
$\mathbf{x}_p$	transmitted signal on pth subcarrier
$\mathbf{x}_i^{2N}$	the last $2N-i+1$ components of vector $\mathbf{x}$
$\tilde{\mathbf{x}}$	estimate of the transmitted signal
$\mathbb{X}_{k,\lambda}^{-1}$	subset of hypersymbols $\{x\}$ for which the λth bit of label b is i
$\hat{\mathbf{x}}_{\mathrm{ML}}$	ML estimate
$\hat{\mathbf{x}}_{\mathrm{MMSE}}$	LMMSE equalized symbol estimate
$\mathbf{y}$	received signal
$\underline{\mathbf{y}}$	extended received signal
$\mathbf{y}_p$	received signal on pth subcarrier
$\overline{\mathbf{y}}_{m_R}(n)$	received signal over all subcarriers on the m_Rth receive antenna at discrete time index n
$\mathbf{z}$	complete data in SAGE estimator
cc	clock cycle
dB	decibel
$^\circ$	degrees

Gb/s	gigabits per second
GHz	gigahertz
Hz	hertz
k	thousand
kbit	kilo bit
kHz	kilohertz
km/h	kilometers per hour
Mbps	megabits per second
MHz	megahertz
mm^2	square millimeters
μs	microsecond
mW	milliwatt
nJ	nano Joule
ns	nanosecond
s	second

2G	second generation
3G	third generation
3GPP	third generation partnership project
4G	fourth generation
ADC	analog to digital converter
AMC	adaptive modulation and coding
AoA	angle of arrival
AoD	angle of departure
APP	*a posteriori* probability
ARQ	automatic repeat request
ASIC	application-specific integrated circuit
ASIP	application-specific instruction set processor
AWGN	additive white Gaussian noise
B3G	beyond third generation
BER	bit error rate
BICM	bit-interleaved coded modulation
BLAST	Bell Laboratories layered space-time
BRAM	block RAM
BS	base station

CCI	co-channel interference
CDMA	code-division multiple access
CIR	channel impulse response
CMOS	complementary metal oxide semiconductor
CoMP	coordinated multi-point
CORDIC	coordinate rotation digital computer
CP	cyclic prefix
CQI	channel quality indicator
CSI	channel state information
DA	data aided
D-BLAST	diagonal Bell Laboratories layered space-time
DD	decision directed
DDCE	decision directed channel estimation
DFT	discrete Fourier transform
DSP	digital signal processing
ED	Euclidean distance
EM	expectation maximization
EVD	eigenvalue decomposition
FD	frequency domain
FEC	forward error control
FER	frame error rate
FFT	fast Fourier transform
FM	fade margin
FPGA	field programmable gate array
GPRS	general packet radio services
GE	gate equivalent
GS	Gram-Schmidt
GSM	Groupe spécial mobile
IEEE	Institute of electrical and electronics engineers
H-BLAST	horizontal Bell Laboratories layered space-time
HDL	hardware description language
HLS	high level synthesis
HSPA	high speed packet access
ICI	intercarrier interference
IFFT	inverse fast Fourier transform

IMT-A	international mobile telecommunications-advanced
IN-SCM	interference and noise spatial covariance matrix
IR-LSD	increasing radius list sphere detector
ISI	intersymbol interference
ITU	International Telecommunication Union
LA	link adaptation
LLR	log-likelihood ratio
LMMSE	linear minimum mean square error
LOS	line-of-sight
LR	lattice reduction
LS	least squares
LSD	list sphere detector
LTE	long term evolution
LTE-A	long term evolution advanced
LUT	lookup table
MAC	multiply and accumulate
MAP	maximum *a posteriori*
MCS	modulation and coding scheme
MIMO	multiple-input multiple-output
MISO	multiple-input single-output
ML	maximum likelihood
MMSE	minimum mean square error
MS	mobile station
MSE	mean square error
NLOS	non line-of-sight
NMT	Nordic mobile telephony
OFDM	orthogonal frequency-division multiplexing
OFDMA	orthogonal frequency division multiple access
OSIC	ordered serial interference cancellation
PAPR	peak-to-average power ratio
PCCC	parallel concatenated convolutional code
PED	partial Euclidean distance
PIC	parallel interference cancellation
PMI	precoding matrix indicator
QAM	quadrature amplitude modulation

QoS	quality of service
QPSK	quadrature phase shift keying
QRD	QR decomposition
RAM	random access memory
RLS	recursive least squares
RTL	register transfer level
RX	receiver
SAGE	space-alternating generalized expectation-maximization
SC-FDMA	single-carrier frequency division multiple access
SD	sphere decoding
SEE	Schnorr Euchner enumeration
SGR	squared Givens rotations
SIC	successive interference cancellation
SIMO	single-input multiple-output
SINR	signal-to-interference-noise ratio
SIR	signal-to-interference ratio
SISO	single-input single-output
SM	spatial multiplexing
SNR	signal-to-noise ratio
SQRD	sorted QR decomposition
SSFE	selective spanning with fast enumeration
STC	space-time code
STBC	space-time block code
STTC	space-time trellis code
SVD	singular value decomposition
TD	time domain
TDMA	time division multiple access
TX	transmitter
TU	typical urban
UMTS	Universal Mobile Telecommunications Services
V-BLAST	Vertical Bell laboratories layered space-time
VHDL	very high speed integrated circuit hardware description language
VLSI	very-large-scale integration
WiMAX	worldwide interoperability for microwave access
WLAN	wireless local are network

ZF	zero-forcing

Contents

1 Introduction

During the last few decades, wireless communication systems have been under major development. The requirements have shifted from the low data rate voice services to real time video transmissions. Support for higher data rates has become more essential and the development towards more advanced wireless systems is still ongoing. Multiple antennas are currently included in many of the wireless standards to achieve the required data rates. This increases the complexity of signal processing algorithms in the receiver. However, the complexity and power consumption of the wireless device should be moderate. This poses challenges in developing algorithms and architectures for the mobile receiver.

The goal of this thesis is to develop receiver algorithms and architectures to meet the high data rate and low complexity requirements of the forthcoming wireless systems. Furthermore, many of the system features are considered when evaluating the suitability of different algorithms for the wireless systems. The work in the thesis concentrates on signal detection, channel estimation and interference mitigation algorithms and their implementation requirements. The evolution of mobile communication systems is reviewed in Section 1.1 and multiple antenna communications are discussed in Section 1.2. The aims and outline of the thesis, including the author's contribution, are covered in Section 1.4.

1.1 Mobile communication systems

The evolution of mobile communication systems has progressed rapidly. The first international cellular networks were deployed in the 1980s, while national car phone systems were employed during the previous decades. The Nordic mobile telephony (NMT) system was the first cellular network used in the Nordic countries [1]. It was based on analog cellular technology, as well as the systems deployed shortly after NMT in North America and Japan. The second generation (2G) cellular systems were pioneered by the Groupe Spécial Mobile (GSM) with a European cellular standard now known globally as the Global Systems for Mobile Communications [2]. The GSM is a digital system using time division multiple access (TDMA) with frequency hopping and frequency shift keying [3]. Simultaneously, TDMA based 2G standards were developed

in the USA and Japan. General packet radio services (GPRS) were included in the GSM standard to enable data transfer and the operating bandwidth was tripled with the introduction of the enhanced data-rates for global evolution (EDGE) [4].

The third generation (3G) mobile communication standards were first being developed by the International Telecommunication Union (ITU) and they were based on wideband code division multiple access (WCDMA) [2]. The standardization was later unified to be performed under the Third Generation Partnership Project (3GPP). The 3G systems further increased the data rates from 2G and added the number of available services [1]. A 3G network was first launched in Japan and shortly after that in Europe, where it was known as Universal Mobile Telecommunications Services (UMTS). The 3GPP 3G system was later further improved with high speed packet access (HSPA) and multiple antennas [5–7].

As the need for higher data rates and a better quality of service (QoS) increased, the 3GPP started the development of the long term evolution (LTE) standard in 2005. LTE uses orthogonal frequency-division multiplexing (OFDM) as the downlink access scheme and single-carrier frequency division multiple access (SC-FDMA) in the uplink [8]. The peak data rates for LTE were defined to be 100 Mbps for downlink and 50 Mbps for uplink [9]. Other requirements for LTE included a scalable bandwidth up to 20 MHz and an increased performance at the cell edge. The evolution of cellular systems is still ongoing. ITU defined the targets for the fourth generation (4G) international mobile telecommunications-advanced (IMT-A) technologies. The LTE-advanced (LTE-A) [10] and the 802.16m mobile worldwide interoperability for microwave access (WiMAX) 2.0 standard from the Institute of Electrical and Electronics Engineers (IEEE) have filled the requirements for IMT-A. The WiMAX 2.0 standard, also known as WirelessMAN-Advanced, reaches the 1 Gb/s data rate requirements with the use of multiple antennas and orthogonal frequency division multiple access (OFDMA) [11–13]. OFDMA is also the access scheme for the LTE-A downlink where up to eight antennas are used to achieve the high data rate requirements [14, 15].

1.2 Multiple antenna communications

Multiple antennas can be used in the transmitter, receiver or both to improve the reliability of the transmission or to increase the data rates. Spatial diversity allows multiple antenna systems to utilize multipath propagation by taking advantage of fading and the channel delay spread [16]. Due to the multiple paths for a signal, combining

them in the receiver can restore and improve the received signal quality. The diversity order increases with the number of spatial streams. Single-input multiple-output (SIMO) antenna configurations can be used for array gain, i.e. enhancing the signal at the receiver by combining the signals from the transmit antennas [17]. SIMO transmission can also be utilized to obtain receive diversity and the diversity order is equal to the number of receive antennas. Multiple-input single-output (MISO) channels can be exploited to achieve transmit diversity [18]. Assuming independently faded streams, the diversity order in the MISO system is equal to the number of transmit antennas [17].

Multiple-input multiple-output (MIMO) schemes can also be used to obtain a diversity gain or an array gain, but unlike in the MISO and SIMO systems, MIMO systems offer also spatial multiplexing (SM) gain [19]. The capacity increase provided by spatial multiplexing is achieved by demultiplexing the data onto different transmit antennas. The capacity grows linearly with the number of transmit and receive antenna pairs in spatial multiplexing MIMO systems if the channel can be estimated in the receiver and the channel paths are independent [20, 21]. Given independently fading MIMO streams, the diversity order of a MIMO system is the product of the number of transmit and receive antennas.

The Bell Labs Layered Space Time (BLAST) architecture demultiplexes the encoded data stream onto separate transmit antennas [20]. The method of dividing a stream into vertical vectors to be transmitted on the antenna array is also known as the vertical BLAST (V-BLAST) architecture [22]. Horizontal transmission, also known as H-BLAST, can also be applied [23]. The streams are then encoded separately for each transmit antenna. The V-BLAST scheme can offer a higher coding gain over the H-BLAST scheme, but the H-BLAST has the advantage of retransmitting only the failed streams [23]. The diagonal BLAST (D-BLAST) architecture [20] applies horizontal encoding after which the codewords are spread over the transmit antennas. The D-BLAST architecture leads to an ideal performance, but the efficiency suffers from the wasted blocks in the beginning and end of the transmission [23].

Transmit diversity in MIMO systems can be achieved with space-time codes (STC) [16]. Using channel coding combined with multiple transmit antennas to achieve diversity was proposed in [24], but space-time codes for multiple antenna communications were introduced in [25], where trellis codes were used to achieve a diversity and coding gain. Space-time trellis codes (STTC) provide a diversity corresponding to the number of transmit antennas but require complex receiver processing. Space-time block codes (STBC) were proposed in [26] for two transmit antennas and were shown to provide a

diversity gain in the order of twice the number of receive antennas and require only simple linear processing at the receiver. STBC for multiple transmit antennas was introduced in [27]. If channel knowledge at the transmitter is available, beamforming can be used to obtain a diversity gain [28, 29].

Both diversity and spatial multiplexing gain can be achieved simultaneously in MIMO communications, but there is a tradeoff between the error probability and data rate [30]. With feedback from the receiver to the transmitter, the transmission can be adapted to perform either spatial multiplexing or to use a diversity mode [31]. Spatial multiplexing can be used in good channel conditions and diversity schemes in poor channels to obtain a good performance in different channel conditions [2]. The modulation can also be adjusted according to the channel conditions [32]. Adaptation of the transmission scheme can be combined with modulation and coding adaptation to approximate the link capacity [33]. Adaptation can be performed by adjusting the rate or power of the transmission [1, 34]. In power adaptation, the transmit power is adjusted to maintain a target error rate and in rate adaptation, the transmission rate is adjusted to the channel conditions. Rate control is more commonly used and more efficient [35, 36]. Link adaptation (LA) and adaptive modulation and coding (AMC) have been extensively studied in the literature [37–40].

1.3 Multicarrier communications and cellular systems

The fading channels exploited by MIMO systems can cause intersymbol interference (ISI) [19]. OFDM suppresses the ISI and it is therefore combined with MIMO transmissions in many communication systems, such as the 3GPP LTE and LTE-A and the WiMAX systems [41]. The idea of OFDM was proposed by Chang in the 1960s [42] and the performance of the OFDM system was considered in [43]. The discrete Fourier transform (DFT) based time-limited multi-tone system was described in [44]. OFDM for mobile communications was proposed in [45], where the results showed significant improvements in performance.

OFDM is a multicarrier (MC) technique where the frequency band is divided into several narrow-band subcarriers which are transmitted in parallel. The duration of each symbol can then be increased, which reduces ISI if the delay spread of the channel is smaller than the duration of the symbol [46]. A MIMO-OFDM transmission system is illustrated in Figure 1. The transmission from each antenna can be reflected from buildings or other structures and arrive at the receiver with delay and attenuation. Due to

the delay in the reflected paths, interference from the previous OFDM symbol is added to the received symbol. Therefore, a cyclic prefix (CP), which contains replicated symbols from the end of the block, is added to the beginning of each block. This eliminates the ISI if the length of the CP is larger than that of the channel [47]. Equalization in the receiver also becomes simpler as ISI is not present. To prevent interference from adjacent subcarriers and to improve the spectral efficiency by overlapping the subcarriers, orthogonality between the carriers is applied [43].

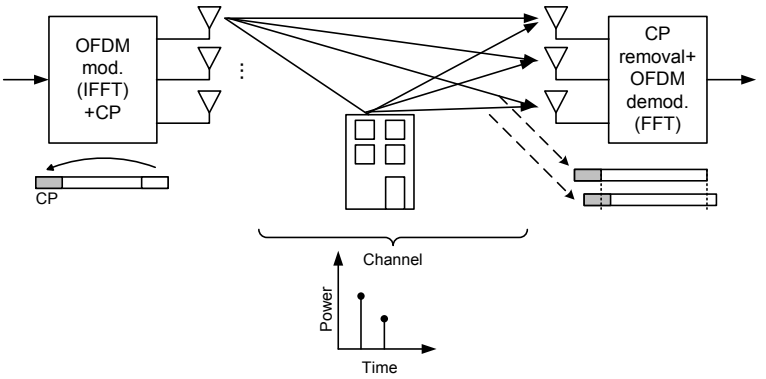

Fig. 1. The wireless MIMO-OFDM transmission system.

The idea of efficient implementation of the DFT by the fast Fourier transform (FFT) [48, 49] motivated the use of OFDM in communication systems [2]. The modulation in OFDM is then performed with an inverse FFT (IFFT) and the demodulation with the FFT. Interleaving and channel coding is often combined with OFDM to increase the robustness of the system [50]. Interleaving the code words over time and frequency prevents a set of contiguous symbols from being exposed to deep fades. If channel state information (CSI) at the transmitter is available, the data and power assigned to each subcarrier can be adapted based on the quality of the subchannel [51].

A high peak-to-average power ratio (PAPR) is one of the drawbacks of OFDM due to the linear combination of the transmitted subcarriers. The peak and average values should be close to each other for an efficient use of the power amplifier [2]. Therefore, high PAPR leads to an increased cost and power consumption in the power amplifiers. Methods to reduce the PAPR, such as clipping and filtering, dummy sequence insertion, selected mapping and pre-coding, can be applied [1, 41]. Another problem in OFDM is the time and frequency offset in the receiver [52]. It can be caused by mismatched

oscillator frequencies in the transceiver or by Doppler spread and can cause ISI and intercarrier interference (ICI) [41]. These offsets can lead to a high error rate, but they can be estimated in the receiver [53]. The frequency offset caused by Doppler spread can change over time and may be more difficult to mitigate. In a scenario with multiple users, orthogonal frequency division multiple access (OFDMA) can be used to allocate a subset of subcarriers from the entire bandwidth to different users. OFDMA can increase the capacity of the system with reasonable subcarrier allocation, but synchronization of the transmissions from different users becomes an issue [41].

The combination of MIMO transmissions and OFDM has gained a great deal of attention from the early combination of MIMO systems and multitone transmission [54] to MIMO-OFDM field trials [55]. MIMO-OFDM in a multiuser scenario has also lead to new problems in optimizing the transmission. MIMO-OFDM is currently adopted in wireless standards, including the 3GPP LTE [8], LTE-A [10] and WiMAX [56].

As the cellular networks consist of cells formed by the transmission range of the base station, transmissions from neighboring cells can cause interference. Co-channel interference (CCI) is a key limiting factor in the forthcoming communication systems. The interference from another cell may be prohibitive for the cell edge user. It may be combatted with interference alignment [57] or scheduling of the time or frequency resources [58]. Schemes such as coordinated multi-point (CoMP) transmission, where the base stations co-operate when transmitting to a user at the cell edge, are currently considered for future wireless systems [59]. Joint processing and coordinated beamforming are the two main considered downlink CoMP transmission schemes [60]. In the joint processing schemes, a resource block is assigned to only one cell edge user from the coordinates cells. In this scheme, the user receives the transmission from multiple cells or only from its own cell, while the other cells are not transmitting on the resource block. Beamforming weights which reduce interference to users in other cells can be used with the coordinated beamforming schemes and allow simultaneous transmission to users in neighboring cells. Both schemes increase the cell edge throughput, but the joint transmission schemes are even more effective than the coordinated beamforming schemes [60].

1.4 Aims, outline and author's contribution

In the future wireless systems, the data rate requirements have increased, but the need for power efficient and low complexity solutions still exists. The goal of this thesis

is to develop algorithms and architectures to meet these requirements. Algorithms, architectures and implementations for detection, channel estimation and interference mitigation in MIMO systems are presented. The performance-complexity trade-offs with realistic system setup and scenarios are obtained through computer simulations and hardware synthesis results. The outcome of the thesis can be used in the mobile receiver design, but the results can also be utilized in system design.

Transmission of independent data streams from different antennas in spatial multiplexing MIMO systems usually causes inter-antenna interference. Advanced receivers are essential in coping with the interference. An optimal detector would be the maximum *a posteriori* probability (MAP) symbol detector which provides soft outputs or log-likelihood ratio (LLR) values to the forward error control (FEC) decoder. Since the computational complexity of the MAP detector is exponential with the number of spatial channels and modulation symbol levels, several suboptimal solutions are considered. The performance-complexity tradeoff of various soft-output MIMO-OFDM detectors is analyzed for application in the evolving next generation cellular standards. Both the information transmission rate and the hardware detection rate combined with the complexity and power consumption are considered when comparing the different detection algorithms. The impact of transmission adaptation on the performance of different detection algorithms is also studied to see if a simpler detector could be used when the transmission is tuned to the channel conditions.

Channel estimation for MIMO-OFDM is also considered. The reference signals used in channel estimation are placed in the OFDM time-frequency grid at certain intervals in most forthcoming systems [61]. The interval may not be sufficiently short when the user velocity is high and the channel is fast fading. The high mobility scenario, which is included in the LTE-A requirements, calls for the use of spatial multiplexing when the channel state information (CSI) at the transmitter becomes outdated for transmission adaptation. Furthermore, the pilot overhead increases with the number of MIMO streams. Additionally, channel estimation based on only pilot symbols does not utilize the channel information available in the data decisions. Decision directed (DD) channel estimation can be used to improve the performance by exploiting the information on the non-pilot symbols or to reduce the pilot overhead by transmitting data symbols instead of pilot symbols. The performance and complexity of channel estimation algorithms is studied using the LTE pilot symbol structure as a benchmark. Two throughput decreasing issues are addressed, namely the fast fading or high mobility scenario with insufficient pilot symbol density and the high pilot overheads from the MIMO pilot symbols. Several

algorithms for channel estimation in high velocity scenarios have been proposed in the literature. However, the actual implementation cost or a performance-complexity comparison of the algorithms has not been previously discussed. Thus, this is the scope of the work in this thesis.

The CoMP schemes may not be able to adapt to the frequently changing channel conditions in high velocity scenarios and their functionality and performance require further study. However, the CCI may be suppressed at the receiver for improved performance and a more efficient use of resources. The complexity and performance of interference suppression combined with two different detection algorithms are presented.

The outline of the thesis is as follows: Chapter 2 consists of the literature review on MIMO receiver algorithms containing previous and parallel work. The system models for the remainder of the thesis are introduced in Chapter 3. The work on detection is discussed first, followed by topics on channel estimation and interference mitigation. MIMO detection algorithms are addressed in Chapter 4. The work presented therein has been previously published in part in [62–66]. Different suboptimal detection algorithms are presented and their performance is compared via computer simulations. The performance is compared in fixed modulation and code rate scenarios, after which the scope is shifted to systems with adaptive modulation and coding. The complexities of the algorithms are compared via the presented implementation results.

Chapter 5 focuses on channel estimation algorithms for MIMO-OFDM. The work has been in part published in [67] and submitted in [68, 69]. The performance of the least-squares (LS), minimum mean square error (MMSE) and the space-alternating generalized expectation-maximization (SAGE) channel estimation algorithms is studied. The theoretical complexity of the channel estimation algorithms is presented and some complexity-performance trade-off aspects of the algorithms are considered as well. The architecture and implementation results in gate counts and power consumption for the pilot symbol based LS, MMSE and the DD SAGE channel estimators are presented for the 2×2 and 4×4 antenna systems. For a more energy efficient solution, a longer latency for the channel estimator is considered. The impact of generating a timely channel estimate for the detector on the performance and complexity is then discussed.

Chapter 6 includes topics on interference mitigation for MIMO-OFDM. The results have been submitted for publication in [70, 71]. The interference and noise spatial covariance matrix measured on the pilot subcarriers is used in data detection and channel estimation. Linear and nonlinear detectors are considered. The impact of the accuracy of the matrix decomposition on the structure of the covariance matrix is studied. An

algorithm to adapt the accuracy of the matrix decomposition and the use of interference suppression is proposed. The different interference mitigation methods are implemented and the performance-complexity tradeoffs are presented. Finally, conclusions and drawn and future work is discussed in Chapter 7.

The thesis is written as a monograph, but part of the results in Chapters 4 and 5 have been published in one journal paper [62] and five conference papers [63–67]. Furthermore, the work done in Chapters 5 and 6 has been submitted to two different journals. The author was the main contributor in all of the papers. The other authors provided help and comments. The novel SSFE-SIC algorithm or the SSFE implementation results from Chapter 4 have not been previously published. Additional simulation results were added to Chapters 5 and 6 that were not included in the journal submissions.

The simulation software was originally developed by Dr. Markus Myllylä and Dr. Nenad Veselinovic and the turbo coding and decoding used in the simulator by Dr. Mikko Vehkaperä. The channel models used in the simulations were generated with the channel simulator from Dr. Esa Kunnari and the original Matlab code for the SAGE channel estimator was produced by Dr. Jari Ylioinas. The author made extensive changes to the simulator before generating the results shown in this thesis.

In summary, the main contributions of the thesis are:

- A performance-complexity comparison of selected detection algorithms for MIMO-OFDM
- The performance of an implemented algorithm defined as goodput, which is a combination of information transmission rate and hardware detection rate
- Evaluation of the detection algorithms, also in a system with adaptive transmission
- Implementation of data aided and decision directed channel estimation algorithms
- Evaluation of the applicability of the channel estimation algorithms for mobile MIMO-OFDM systems with different pilot symbol densities
- Finding the complexity and performance of co-channel interference mitigation
- An adaptive algorithm for CCI mitigation to obtain a good performance with possibility for power savings.

2 Literature review

Receiver algorithms for spatial multiplexing MIMO transmissions are discussed in this chapter. The literature containing previous and parallel work in MIMO detection is reviewed in Section 2.1. Linear detectors and interference cancellation are covered first, followed by tree search algorithms and some implementation related optimizations. Channel estimation is discussed in Section 2.2, where pilot allocation and different channel estimation methods are covered. Section 2.3 includes methods for co-channel interference suppression.

2.1 Detection in MIMO systems

2.1.1 Linear detection and interference cancellation

Minimum mean square error (MMSE) or zero forcing (ZF) equalization principles can be straightforwardly applied in MIMO detection [17, 72]. The ZF equalizer is given by

$$\mathbf{W}_{ZF} = (\mathbf{H}^{\mathrm{H}}\mathbf{H})^{-1}\mathbf{H}^{\mathrm{H}} = \mathbf{H}^{\dagger}, \tag{1}$$

where $\mathbf{H}$ is the channel matrix and $(\cdot)^{\dagger}$ is the pseudo-inverse [73] of the matrix. The ZF receiver suppresses the interference between the MIMO streams, but it enhances the noise and the performance is far from optimal. The MMSE equalizer minimizes the mean square error (MSE), i.e.,

$$\arg\min_{\mathbf{W}} E\{||\mathbf{W}\mathbf{y} - \mathbf{x}||^2\}, \tag{2}$$

where $\mathbf{W}$ is the MMSE filter, $\mathbf{y}$ is the received signal, $\mathbf{x}$ is the transmitted signal and takes the noise term into account [74]. It outperforms the ZF receiver, but at high signal-to-noise ratios (SNR) the performance is equal to that of the ZF receiver. The diversity order for the ZF and MMSE equalizers is only $M - N + 1$, where M is the number of receive antennas and N is the number of transmit antennas [17]. After the equalizer, a decision on the transmitted symbol vector is made either by quantization or by calculating the log-likelihood ratios (LLR) of the transmitted bits by taking into account the residual channel and interference plus noise covariance matrix after equalization [75].

The linear detectors can suffer a significant performance loss in fading channels, in particular with spatial correlation between the antenna elements [76]. The nulling and cancelling or interference cancellation methods consider the other layers as interference while detecting the desired layer [22]. The nulling of each layer can be performed with a ZF or an MMSE equalizer. In successive interference cancellation (SIC), the nulling and cancelling of each layer is performed in a serial matter. The SIC receiver can suffer from error propagation if an incorrectly detected layer is used in the cancellation. Therefore, the ordered serial interference cancellation (OSIC) was proposed in the original papers considering the Bell Laboratories layered space-time (BLAST) architecture [22, 77, 78]. There, the strongest layer, i.e. the layer with the highest signal-to-interference-plus-noise ratio (SINR), is detected first and its interference is cancelled from the other streams. Without error propagation, each cancellation step increases the diversity [17]. In parallel interference cancellation (PIC), all the layers are detected simultaneously and then cancelled from each other followed by another stage of detection [79]. PIC was proposed to reduce the latency from SIC but has a higher computational complexity.

The linear ZF detector is optimal if the channel matrix is orthogonal. However, since this is not usually the case in practice, lattice reduction (LR) can be used to transform the channel matrix to a more orthogonal matrix after which ZF or MMSE filters can be applied [80]. Using LR aided linear equalization can improve the performance significantly [81].

2.1.2 Tree search algorithms

Uncoded systems

The maximum likelihood (ML) detector performs an exhaustive search over all possible transmitted symbol vectors. The complexity of the ML detector is exponential in the number of states (N), but it is the optimal detector for finding the transmitted symbol vector [17]. Sphere detectors (SD) calculate the ML solution by taking into account only the lattice points that are inside a sphere of a given radius [82]. Sphere detection algorithms are based on the QR decomposition (QRD) of the channel matrix, which allows for the tree based search of the lattice points. The choice of the sphere radius has an impact on the performance and complexity. It can be adjusted according to the noise variance [83]. The Pohst enumeration strategy for ML detection, also known as the Viterbo-Boutros (VB) algorithm [83], can be thought of the classical sphere detection

algorithm where the natural spanning of the nodes is applied. The Schnorr-Euchner enumeration (SEE) [84] spans the nodes in a zig-zag order, making the search process faster [85]. Improvements to the VB and Schnorr-Euchner based algorithms were proposed in [86].

The spanning of the tree can be performed in a depth-first, breadth-first or metric-first manner [87]. The VB and SEE are considered to be depth-first algorithms where the tree search is performed one branch at a time from the top of the tree to the last leaf node or until a threshold value is reached. The breadth-first tree search is performed by expanding the nodes on each level of the tree before moving to their leaf nodes. If the number of nodes to continue from each level is limited, sorting has to be performed to find the nodes with the smallest Euclidean distances. In this case, the result may not be the exact ML solution. The M-algorithm [87] and the K-best algorithm [88] are examples of the breadth-first approach. The metric-first or best-first algorithms extend the path with the best metric while maintaining a list of path metrics [89]. The metric-first algorithms can be more efficient than the depth-first and breadth-first algorithms and they find the ML solution [90]. The ever-increasing radius sphere detector (IR-SD) [91] increases the sphere radius during the tree search, which leads to finding the ML solution faster while requiring less storage for the path metrics [92].

Coded systems

In a system with FEC, the optimal method for finding the transmitted symbols is to jointly perform the symbol detection and data decoding [93]. However, the method is infeasible in practice, since the complexity grows exponentially in the dimensions of the search space. The joint detection and decoding method is then usually approximated by separating the detection and decoding problems and exchanging soft information between the detector and decoder. The turbo principle used in decoding [94] can be used to perform detection and decoding iteratively [95, 96]. The MAP detector [97] is the optimal detector for providing the *a posteriori* probabilities (APP) for the decoder. However, its complexity may also be prohibitive. Suboptimal techniques such as MMSE based turbo equalization [98–101] where interference cancellation is performed based on the soft bit decisions from the turbo decoder have been considered.

The MAP detector can be approximated by a list sphere detector (LSD), which provides the log-likelihood ratios (LLR) as APPs for the decoder [102]. The sphere detector algorithms can be modified to provide a list of candidate symbols for the LLR

calculation instead of just one solution. The breadth-first tree search based K-best LSD algorithm is a modification of the K-best algorithm [103]. The *a priori* LLRs from the decoder can be used to reduce the number of visited nodes in the K-best detector [104]. The depth-first [105–107] and metric-first [108, 109] sphere detectors have also been modified to perform well in coded systems.

2.1.3 Optimizations and implementations

As MIMO detection is a complex problem, several implementation friendly modifications to the detection algorithms have been proposed. Sorted QRD (SQRD) can be used in the MMSE based BLAST detection to reduce the computational complexity with no impact on performance [110]. Modifications to the soft output calculation of the detector and the soft symbol calculation from the decoder in a SIC receiver were proposed in [111]. Even lower complexity for the soft output calculation from the ZF or MMSE equalizer can be achieved with the approximate LLR approach [112]. MMSE based preprocessing can also be used for the tree search detectors to improve the performance [113].

Several implementations of the MMSE equalizer can be found from the literature. A direct matrix inversion algorithm is applied for the MMSE filter calculation in [114]. A QR decomposition based matrix pseudo inverse calculation for MMSE-VBLAST is implemented in [115]. An architecture and implementation for an MMSE detector in [116] utilizes Strassen's algorithms in the matrix inversion. The implementations of the QRD based MMSE detector via the coordinate rotation digital computer (CORDIC) and squared Givens rotation (SGR) algorithms were compared in [117]. A modified Gram-Schmidt based sorted QRD implementation was presented in [118], where the QRD can be used for SIC or as preprocessing for tree search algorithms. Further implementations of the QR decomposition can be found in [119–121]. An ASIC implementation of a SISO detector for iterative MIMO decoding utilizing an MMSE-PIC algorithm was discussed in [122].

The silicon complexity analysis of ML detection in [123] concluded that ML detection can be applied for low order modulation, but sphere detection can be applied to achieve performance close to that of ML detection. An implementation of the K-best algorithm with a large list size was reported in [124]. A simplified norm calculation and pre-sorted metric computations for the K-best algorithm were used in [125]. A modification to the M-algorithm was proposed in [126], where the number of nodes extended in each level can be adjusted. Optimizations of a hard-output K-best detector

were presented in [127] and a radius adaptive K-best detector and its implementation were reported in [128]. An architecture and implementation for the K-best algorithm where the nodes are expanded on demand were presented in [129]. An algorithm combining the depth-first and breadth-first approaches in order to reduce the complexity and achieve a close to ML performance was introduced in [130]. The depth-first sphere detector was implemented in [131]. The throughput of the sphere detector was not constant and depended on the SNR as the depth-first tree search approach was utilized. A bounded search for the sphere detector was proposed in [132], which reduces the latency and hardware cost compared to the unbounded sphere detector while maintaining good performance. A flexible implementation of a sphere detector, which could adapt to the antenna configuration and modulation was presented in [133]. Switching between PIC and LSD in an iterative receiver can reduce the required list size and number of iterations [134].

Several tree search algorithms, other than sphere detectors, have been proposed to allow a parallel implementation with fixed complexity and latency. The selective spanning with fast enumeration (SSFE) algorithm [135] and the flex-sphere algorithm [136] use SEE to expand a fixed number of nodes on each level. The fixed sphere decoder in [137] has also similar functionality. The SSFE algorithm does not include sorting and is suitable for programmable platforms. The layered orthogonal lattice detector (LORD) was proposed in [138]. It consists of performing QR decomposition and a SSFE type tree search for different orderings of the channel matrix. An iterative version of the LORD algorithm was proposed in [139].

Comparison of implementations of the different detection algorithms presented in the literature is difficult as the design methods and platforms vary and the performance results are obtained in different scenarios. Therefore, different detection algorithms are compared through a unified simulation and design process in this thesis in order to obtain comparable results.

2.2 Channel estimation in OFDM

Coherent or synchronized transmission [140] is applied in most wireless systems. For coherent detection of the transmitted signal, the channel has to be known or estimated at the receiver [141]. Differential modulation techniques can be used to avoid channel estimation, but the performance degradation is high. In OFDM, channel estimation can be performed with a blind or a non-blind technique [142]. The blind channel estimation

method does not require the use of training sequences or pilot symbols and enables a more efficient use of the available bandwidth. The channel estimates are obtained using the statistical properties of the received data which is collected over a certain time period [143]. A noise subspace method for blind channel estimation for MIMO-OFDM was presented in [143], where the accurate channel estimation results were found by increasing the length of the observation block. With the blind channel estimation methods, decreased performance can be observed in fast fading scenarios. Pilot symbols can be used to improve the channel estimation accuracy of blind channel estimation, resulting in a semi-blind channel estimation scheme [144]. In [144], a subspace based semi-blind channel estimator was presented which is able to track slow variations in the channel. Given the large memory requirements of blind channel estimation and the inability to track fast channel variations, non-blind channel estimation is used in most of the current wireless transmission systems. Pilot aided transmission is used in most of the wireless transmission systems and it will be discussed in more detail. The non-blind channel estimation methods can be divided into two groups, namely the data aided (DA) or decision directed (DD) methods.

2.2.1 Data aided channel estimation

Pilot allocation

A training sequence or pilot symbols known at the receiver are used in estimating the channel with the DA methods. The training sequence is usually inserted in the beginning of the transmission with no simultaneous data transmission. With pilot symbol assisted modulation [145], known symbols are inserted periodically among the data symbols and the peak-to-average power ratio or pulse shape is not affected. Pilot assisted transmission is used widely in wireless communication systems as the periodically transmitted pilot symbols enable more frequent channel estimation in fading channels [146]. The impact of training on the capacity of a fading channel was considered in [147]. It was found that optimal results can be obtained in high signal-to-noise ratios (SNR), but the training schemes are suboptimal at low SNRs. A higher number of pilot symbols leads to better channel estimation accuracy, but since the pilot symbols replace the data symbols, the transmission rate is decreased. Therefore, the placement of the pilot symbols should be designed as a compromise between a good channel estimate and a high transmission rate.

In OFDM, the pilot symbols are usually placed in a time-frequency grid of subcarriers. The pilot symbols placing should be dense enough in frequency domain so that the channel variations are captured accurately. The spacing of the pilot subcarriers then depends on the coherence frequency [142]. Similar criteria for pilot symbol spacing should be applied in the time domain in order to capture the channel variations depending on the Doppler spread. The optimal pilot sequence in MIMO-OFDM should be equispaced, equipowered and phase shift orthogonal in order to obtain the minimum mean square error (MSE) of the least squares (LS) channel estimate [148]. Furthermore, the pilot symbols should be spaced with the maximum distance to prevent the wasting of resources and they should be placed on different subcarriers over consecutive OFDM symbols. In [149], a placement of the pilot symbols that maximizes the capacity assuming a minimum mean square error (MMSE) channel estimate was found. The pilot symbols should then be placed periodically in frequency. The training sequence can also be designed to simplify the channel estimation [150]. Pilot symbol assisted modulation is used in most of the current and upcoming wireless MIMO-OFDM transmission systems, such as the WiMAX, LTE and LTE-A. The pilot symbols are placed at certain intervals in time and frequency. In a MIMO system, when a pilot is transmitted for one antenna, the other antennas transmit nothing [61].

Channel estimation

The channel estimates for the pilot positions are most commonly obtained by maximum likelihood (ML) or MMSE based estimators. Maximum likelihood (ML) channel estimation is equivalent to LS estimation with additive white Gaussian noise when the number of pilot symbols is larger than the channel length [151]. The ML estimator assumes that the channel impulse response (CIR) is deterministic and that there is no knowledge of the channel statistics or the SNR. The CIR is assumed to be random in the MMSE estimation where the SNR and prior information on the channel are exploited. The recursive LS (RLS) algorithm can be used to enhance the channel estimation performance, but it is most suitable for slow fading channels [148]. The MMSE estimator minimizes the MSE of the channel estimates, but the complexity is high compared to the ML or LS estimators. The ML and MMSE methods were compared in [151] and [152] for OFDM systems and the MMSE was found to outperform the ML in low SNRs. The calculation of the MMSE estimate requires a large matrix inversion. A low-complexity approximation of the MMSE estimator was proposed in [153], where the

singular value decomposition (SVD) was used to reduce the complexity. The complexity of the MMSE estimator can also be reduced by considering only the high energy channel taps [152]. The same modification can be extended to the LS estimator.

When the channel is estimated only on the set of pilot subcarriers, the estimates for the data carriers can be obtained through interpolation. The performance of the piecewise constant and piecewise linear interpolation techniques were compared in [154]. In constant interpolation, the channel is assumed to be constant on the subcarriers adjacent to the pilot carriers. In linear interpolation, the channel frequency response is assumed to change linearly between pilot subcarriers. The performance was found to improve with linear interpolation from the constant interpolation to the extent that the number of pilots could be decreased. Higher order polynomial fitting can be used to obtain the channel estimates for the data subcarriers when a priori information on the frequency selectivity of the channel is available [142]. Transform domain techniques may also be used for obtaining the channel estimates for the whole bandwidth. The fast Fourier transform (FFT) is widely used due to its low complexity. The inverse FFT transforms the channel frequency response into time domain where the low power taps can be eliminated and the noise reduced channel can be transformed back to frequency domain with the FFT [142]. MMSE filtering can also be used to predict the channel of the current OFDM symbol based on channel estimates from previous symbols [155], i.e. time and frequency domain correlation of the channel frequency response, can be exploited in the channel estimation. For improved performance in MIMO-OFDM systems, the spatial correlation can be included in the MMSE channel estimation [156].

2.2.2 Decision directed channel estimation

The decision directed channel estimation (DDCE) method uses the detected data symbols and the channel estimates from previous OFDM symbols in calculating the current channel estimate. The performance of the DDCE can degrade if the data symbols are detected incorrectly or if the channel estimate used for initialization is incorrect or outdated due to a fast fading environment. With either of the impairments present, the errors in DDCE will propagate to the following channel estimates. Therefore, the correct initialization is important in DDCE. The performance can be improved by sending pilot symbols more frequently, using prediction algorithms to predict the channel for the next OFDM symbol, filtering the channel estimates with the transform domain techniques or the MMSE filter and using channel coding to improve the data symbol estimates [142].

Iterative channel estimator which utilizes the preamble, pilot symbols and data symbols was proposed in [157].

The expectation maximization (EM) algorithm [158] has been considered widely for DDCE. It can be used to calculate the maximum likelihood (ML) estimate iteratively, avoiding the matrix inversion. It uses the probabilities of the transmitted symbols from the decoder, which makes the EM algorithm attractive for coded OFDM transmission systems [142]. The EM algorithm includes a maximization and an expectation step. The channel is estimated with the maximization step and the expectation step estimates the component of the transmitted signal. The steps are alternated iteratively to obtain a correct channel estimate. The channel estimate converges to the ML estimate when a high enough number of iterations is performed. The DDCE can be used together with pilot aided channel estimation to improve the estimation accuracy in fast fading scenarios.

The space-alternating generalized expectation-maximization (SAGE) algorithm [159] updates the parameters sequentially instead of simultaneously as in the classical EM algorithm. This leads to a faster convergence with the SAGE algorithm. Two different EM algorithms were introduced for channel estimation in OFDM in [160]. The EM and SAGE algorithms were compared and the SAGE was found to converge faster and have a lower complexity. The SAGE algorithm has been considered for channel estimation jointly with detection and decoding in [161] and for MIMO-OFDM in [162].

Implementation of channel estimation algorithms

Implementations of channel estimation algorithms have not been reported in the literature as extensively as the implementations of detection algorithms. In fact, most of the reported implementations deal with the ML or filtering type solutions. An implementation of an OFDM receiver with a transform domain channel estimator was presented in [163]. A modification to the maximum likelihood estimator and its implementation can be found in [164]. An implementation for an approximate linear MMSE channel estimator was reported in [165] and in [166] a singular value decomposition (SVD) based MMSE channel estimator for MIMO-OFDM systems was presented. Data carriers are used in channel estimation for calculating channel variations in [167]. However, implementation results for a decision directed channel estimator have not been presented in the literature. Furthermore, a performance or complexity comparison of different types of channel estimators has not been previously carried out.

2.3 Interference mitigation

Signals from base station in other cells can cause interference on the desired signal in an OFDM system. The co-channel interference can be measured on the pilot subcarriers and the interference-plus-noise correlation matrix [168] can be used in both channel estimation and in whitening the received signal for detection. The interference can be synchronous or asynchronous. With synchronous interference, the interferers cyclic prefix (CP) is aligned with the desired signals CP [142]. Channel estimation algorithms for channels in the presence of co-channel interference were presented in [169]. If the interference is synchronous, a structured model for the covariance can be used with few parameters.

CCI suppression for receive diversity schemes have been considered in the literature as the degrees of freedom can be used for eliminating the interference [170]. In a scheme with a higher number of receive than transmit antennas, each additional receive antenna can be used to eliminate an interfering signal. The suppression of asynchronous interference was considered in [171] and [172]. It was shown in [172] that the circular-convolution methods can fully suppress the asynchronous interference only if the number of receive antennas is higher than that of channel paths. It was then proposed to exploit the CP with a semi-blind asynchronous interference suppressor, which was found to suppress both the synchronous and asynchronous interference. A suppression method for asynchronous CCI for MIMO-OFDM was discussed in [171], where the interference spatial covariance matrix was exploited. With asynchronous interference, the channel of the interfering signal cannot be measured on the subcarriers, and thus, the conventional interference cancellation cannot be applied effectively. Therefore, the covariance of the interference was obtained by measuring the interference on the subcarriers, after which Cholesky decomposition and low-pass smoothing was applied.

A semi-structured interference suppression method for OFDM was presented in [173]. A low-rank model for the CCI part of the spatial covariance matrix was applied in [174]. The structured covariance model leads to a fewer number of estimated parameters which could have errors. Therefore, the total number of errors in the estimates can be decreased. The low-rank model can be obtained from an eigenvalue decomposition of the spatial covariance matrix which can then be used in the ML detection of the received signal. A model averaged interference mitigation method for MIMO-OFDM was proposed in [175], where the interference and noise spatial covariance matrix (IN-SCM) was parameterized via a number of low rank models. A low complexity

maximum a posteriori receiver was derived to regulate the log-likelihood ratio (LLR) values. In addition, a probability for the number of interferers was obtained and used in the LLR calculation.

Implementations for the aforementioned interference mitigation methods have not been presented in the literature to the best of our knowledge. However, some implementations of the SVD can be found. The SVD can be used for the matrix decomposition needed in the nonlinear detection and matrix structuring when suppressing the interference. In the case of a covariance matrix, the SVD can be replaced with a more simple eigenvalue decomposition (EVD). Coordinate rotation digital computer (CORDIC) algorithms are often used in the calculation of the SVD [176]. A very-large-scale integration (VLSI) implementation of the SVD was presented in [177]. Implementations combining the QRD and SVD were presented in [178, 179] and field programmable gate array (FPGA) implementations of the SVD were reported in [180, 181]. Nevertheless, the performance-complexity trade-offs of interference mitigation methods have not been discussed in the literature.

2.4 Design methodology

High level synthesis (HLS) is used to obtain the implementation results in this thesis. Even though HLS tools have been developed for decades, only the tools developed in the last decade have gained a more widespread interest. The main reasons for this are the use of an input language, such as C, familiar to most designers, the good quality of results and their focus on digital signal processing (DSP) [182]. HLS tools are especially interesting in the context of rapid prototyping where they can be used for architecture exploration and to produce designs with different parameters [183].

The design process starts with a high level description of the functionality of the block. In this work, C code is used as the input language to the HLS tool. Bit-accurate or fixed point data types are assigned to the variables in the design. The word lengths for the fixed point variables are found by performing computer simulations with the fixed length variables and comparing the performance to that obtained with floating point variables. The high level description may have to be modified before being suitable for the HLS tool. In general, HLS tools first compile the input description, after which they allocate hardware resource and schedule the design before generating the register transfer level (RTL) implementation [184]. Without any timing and allocation constraints in the input file, the generation of different architectures by changing the

parameters in the tool is possible. After obtaining the RTL with the desired timing and complexity results, synthesis is performed with application-specific integrated circuit (ASIC) or field programmable gate array specific tools to obtain the final complexity results.

The benefits of using a HLS tool include a more unified design flow, low design effort, reduced verification burden and more generic designs [185]. The unified design flow allows the designer to return to the specifications and generate a new architecture without a time consuming design process. Without the need to manually design the architecture or scheduling, the chance of errors is reduced. With generic designs, the implementation can be easily modified by making minor changes to the input or constraints. However, using HLS requires knowledge of hardware design and architecture exploration, familiarity with the tool specific options and the generation of a suitable input code to the tool. Thus, the learning curve for using HLS can be lengthy. Also, the resulting RTL from a HLS tool may not be as optimized as a corresponding hand written RTL. HLS tools have been used in the implementation of MIMO detection algorithms on FPGA [109, 186] and ASIC [187]. Despite their many advantages, HLS tools have not yet been extensively utilized in the implementations presented in the literature.

Catapult ® C Synthesis tool [188] was used in the implementation of the receiver algorithms in this thesis. It synthesizes algorithms written in ANSI C++ and SystemC into high-performance, concurrent hardware. This single source methodology allows designers to pick the best architecture for a given performance/area/power specification while minimizing design errors and reducing the overall verification burden. While the results may not always be as optimal as with hand-coded HDL, the tool allows experimenting with different architectures in a short amount of time and the comparison of different algorithms can be made, provided they are implemented with the same tool. The complexity results can be close to the hand-coded ones with small designs [186]. There can be a higher difference with large designs.

3 System, signal and channel models

The system model, signal models for detection and channel estimation and the used channel model are presented in this chapter. A common system model for the remainder of the thesis is presented in Section 3.1. As the notations in the signal models differ for the detection and channel estimation related work, the signal model for detection is introduced in Section 3.2 and for channel estimation in Section 3.3. Transmission adaptation is also briefly described in Section 3.3 and the reference symbol structure is discussed in Section 3.3. The channel models used in computer simulations are presented in Section 3.4.

3.1 System model

An OFDM based MIMO transmission system with N transmit (TX) and M receive (RX) antennas, where $N \leq M$, is considered. A layered space-time architecture with horizontal encoding is applied. The cyclic prefix of an OFDM symbol is assumed to be long enough to eliminate the intersymbol interference. The system model is illustrated in Figure 2. The blocks with solid lines are common for all scenarios throughout the thesis. The blocks with dashed lines are used in parts of the thesis. Precoding and CQI calculation are used only in part of the results in Chapters 4 and 6 and channel estimation is used in Chapters 5 and 6.

The LTE standard specifies a maximum of two separately encoded data streams [189]. Therefore, two streams of data bits are encoded separately in the transmitter, after which they are interleaved. Two separately encoded streams are also used in the 4×4 antenna system. Each separate stream is then multiplexed onto two transmit antennas. The bit streams are modulated onto quadrature amplitude modulation (QAM) symbols. Precoding is performed when transmission adaptation is used before transforming the symbols to time domain with the IFFT. In the receiver, the symbols are transformed into frequency domain with the FFT. The soft detector provides soft output LLRs for the decoder. Feedback from the decoder can be used in the detector. The soft symbol estimates from the decoder can also be used in the channel estimation or only the received symbols with the known pilot symbols may be utilized. The channel quality indicator (CQI) is calculated when transmission adaptation is used.

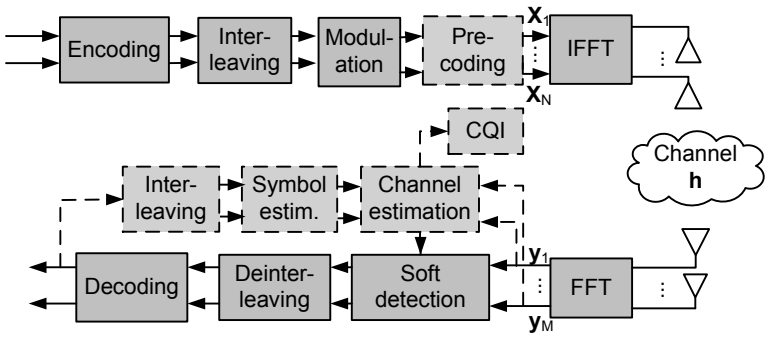

Fig. 2. The MIMO-OFDM system model.

The received frequency domain signal vector $\overline{\mathbf{y}}(n)$ at a discrete time index n after the discrete Fourier transform (DFT) can be described as

$$\overline{\mathbf{y}}(n) = \mathbf{X}(n)\overline{\mathbf{F}}\mathbf{h}(n) + \mathbf{w}(n), \tag{3}$$

where $\mathbf{X}(n) = [\mathbf{X}_1, ..., \mathbf{X}_N] \in \mathbb{C}^{P \times NP}$ is the transmitted signal over P subcarriers and N transmit antennas, $\overline{\mathbf{y}} = [\mathbf{y}_1, .., \mathbf{y}_P] \in \mathbb{C}^{P \times M}$, $\mathbf{w} \in \mathbb{C}^{P \times M}$ contains circularly symmetric complex Gaussian distributed noise with variance σ^2, $\overline{\mathbf{F}} = \mathbf{I}_N \otimes \mathbf{F}$ is a $NP \times NL$ matrix from the DFT matrix with $[\mathbf{F}]_{u,s} = \frac{1}{\sqrt{P}} e^{-j2\pi us/P}$, $u = 0, ..., P-1$, $s = 0, ..., L-1$, L is the length of the channel impulse response and $\mathbf{h} \in \mathbb{C}^{NL \times M}$ is the time domain channel matrix.

Parallel concatenated convolutional coding (PCCC) is used in the turbo encoding as specified in [190] for LTE. The encoder consists of two 8-state constituent encoders and one turbo code internal interleaver. The rate of the constituent encoders is 1/2. Encoding is performed over one OFDM symbol. The turbo decoder consists of two MAP decoders and an interleaver [97]. Eight iterations in the turbo decoder are performed. The log-likelihood ratios in the decoder are calculated with the soft-input soft-output APP module [191].

3.2 Signal model for detection

The received frequency domain (FD) signal on the pth subcarrier at discrete time index n can be described with the equation

$$\mathbf{y}_p(n) = \mathbf{H}_p(n)\mathbf{x}_p(n) + \eta_p(n), \quad p = 1, 2, \ldots, P, \tag{4}$$

where P is the number of subcarriers, $\mathbf{x}_p \in \mathbb{C}^N$ is the transmitted signal on pth subcarrier, $\mathbf{y}_p \in \mathbb{C}^M$ is the pth vector from $\overline{\mathbf{y}}$, $\eta_p \in \mathbb{C}^M$ is a vector containing circularly symmetric complex Gaussian distributed noise with variance σ^2 and $\mathbf{H}_p \in \mathbb{C}^{M\times N}$ is the frequency domain channel matrix containing complex Gaussian fading coefficients. Bit-interleaved coded modulation (BICM) is applied. The entries of $\mathbf{x}_p$ are drawn from a complex QAM constellation Ω and $|\Omega| = 2^Q$, where Q is the number of bits per symbol. The set of possible transmitted symbol vectors is Ω^N. The binary vector $\mathbf{b}_p$ corresponding to $\mathbf{x}_p$ has elements b^j, where $j = (k-1)Q, ..., kQ-1$ with the kth element of $\mathbf{x}_p$. The time index n will be omitted in the sequel in the detection related work.

A real valued system model is sometimes assumed for simpler processing in the sphere detector. The real valued received signal can then be expressed as

$$\begin{bmatrix} \mathrm{Re}\{\mathbf{y}_p\} \\ \mathrm{Im}\{\mathbf{y}_p\} \end{bmatrix} = \begin{bmatrix} \mathrm{Re}\{\mathbf{H}_p\} & -\mathrm{Im}\{\mathbf{H}_p\} \\ \mathrm{Im}\{\mathbf{H}_p\} & \mathrm{Re}\{\mathbf{H}_p\} \end{bmatrix} \begin{bmatrix} \mathrm{Re}\{\mathbf{x}_p\} \\ \mathrm{Im}\{\mathbf{x}_p\} \end{bmatrix} + \begin{bmatrix} \mathrm{Re}\{\eta_p\} \\ \mathrm{Im}\{\eta_p\} \end{bmatrix}, \tag{5}$$

where $\mathrm{Re}\{\cdot\}$ and $\mathrm{Im}\{\cdot\}$ denote the real and imaginary parts of the signal. The dimensions of the real valued signals are then twice of those of the complex valued signals.

Transmission adaptation

Feedback from the receiver to the transmitter can be used to improve the performance of the system. Several metrics for the channel quality and transmission adaptation have been used in the literature, but the channel capacity was chosen for the metric in this work as the aim is to study the impact of adaptation on different receiver algorithms and not to optimize the adaptation. The channel capacity or signal-to-interference-noise ratio (SINR) based channel quality indicator is calculated in the receiver and then sent back to the transmitter. The CQI includes the indices to adapt modulation, code rate and transmission rank for the downlink transmission. A suitable precoding matrix from a predefined codebook is also informed in the form of a precoding matrix indicator (PMI) [189]. The channel capacities with different precoding matrices are calculated in the receiver and the highest capacity achieving precoding matrix is selected. A lookup table is used to select the best modulation, code rate and transmission rank combination for the calculated capacity while maintaining the target frame error rate (FER).

The Shannon capacity on a subcarrier p with no CSI at the transmitter and perfect CSI at the receiver can be calculated as [141]

$$C = \log(\det(\mathbf{I} + \frac{E_s}{\sigma^2 M}\mathbf{H}_P^{\mathrm{H}}\mathbf{H}_p)) \tag{6}$$

and it can be summed over all the subcarriers in the frame to obtain the threshold used in the modulation and coding scheme (MCS) selection. Different MCS can be applied for blocks of subcarriers to achieve a better performance in a frequency selective channel. If precoding is used, $\mathbf{H}$ in (6) is replaced by $\mathbf{PH}$ and the $\mathbf{P}$ with the largest capacity is selected. The instantaneous SINR can also be used in the MCS selection and it can be calculated for the jth stream as

$$\gamma_j = \frac{1}{[(\mathbf{I} + \frac{E_s}{\sigma^2 M}\mathbf{H}_p^{\mathrm{H}}\mathbf{H}_p)^{-1}]_{jj}}. \tag{7}$$

The capacity based MCS selection is assumed here. The subscript p will be omitted for clarity in the sequel.

3.3 Signal model for channel estimation and interference mitigation

The received frequency domain signal vector $\overline{\mathbf{y}}(n)$ on the m_Rth receive antenna at a discrete time index n after the discrete Fourier transform (DFT) can be described as

$$\overline{\mathbf{y}}_{m_R}(n) = \mathbf{X}(n)\overline{\mathbf{F}}\mathbf{h}_{m_R}(n) + \mathbf{i}_{m_R}(n), \tag{8}$$

where $\overline{\mathbf{y}}_{m_R} = [y_{m_R,1}, .., y_{m_R,P}]^{\mathrm{T}} \in \mathbb{C}^P$ and $\mathbf{h}_{m_R} \in \mathbb{C}^{NL}$ is the time domain channel vector from the transmit antennas to the m_Rth receive antenna. In the system model for Chapter 6, $\mathbf{i}_{m_R} \in \mathbb{C}^P$ contains interference plus identically distributed complex white Gaussian noise with the spatial covariance $\mathbf{Q}_i$ and in Chapter 5, it is assumed that $\mathbf{i}_{m_R}$ contains only noise. The entries of the diagonal matrix $\mathbf{X}_{m_T} \in \mathbb{C}^{P\times P}$ are from a complex QAM constellation Ω and $m_T = 1, ..., N$ and $m_R = 1, ..., M$.

The cell-specific reference signal or pilot symbol positions in LTE resource elements are illustrated in Fig. 3, where the downlink slot consist of OFDM symbols i, where $i = 0, .., 6$ for the normal cyclic prefix [61]. Each element in the grid corresponds to a resource element. Reference signals are transmitted in the first, second and fifth OFDM symbols. The reference signals in the first antenna port are illustrated with black, in the second with vertical stripes, in the third with horizontal stripes and in the fourth port with diagonal stripes. Nothing is transmitted on the other antenna ports when a reference signal is transmitted on one antenna port. The reference signals for each antenna port are mapped to every 6th resource element in frequency. Quadrature phase shift keying (QPSK) modulated reference signals are assumed.

The pilot overhead in the 2×2 MIMO is roughly 9.5% and in the 4×4 MIMO 14%. With 8×8 MIMO, the pilot overhead is more than 20% when the demodulation reference signals are used. In LTE-A, user specific or demodulation reference signals are specified to support up to eight transmit antennas [61]. With spatial multiplexing, demodulation reference signals can be transmitted for all antennas in the last two OFDM symbols in a slot. Reference signals for up to four antennas can be transmitted in the same subcarrier and orthogonal cover codes are used to achieve time and frequency domain orthogonality. The demodulation reference signals can be used with precoding, so that the channel estimate obtained from the reference signals corresponds to the precoded channel. The demodulation reference signals are not considered in this work.

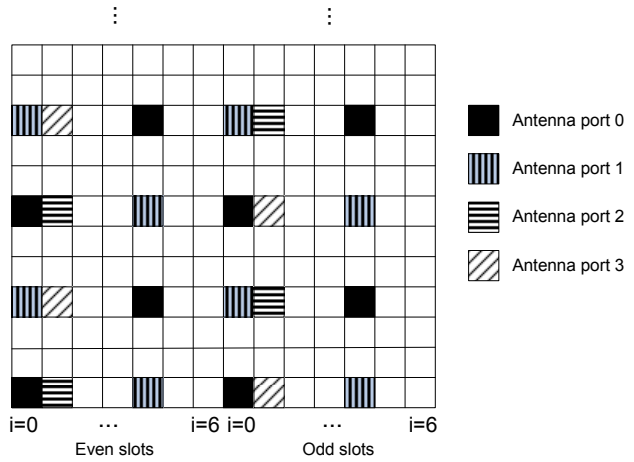

Fig. 3. The LTE pilot structure ([67], published by permission of IEEE).

3.4 Channel model

Several MIMO channel models have been proposed to account for the spatial correlation and frequency selectivity found in many propagation environments [192]. The models can be divided into narrowband and wideband channel and time-varying and time-invariant channels. The models can also be divided into physical models and analytical models [192]. Physical models characterize the wave propagations, while analytical models characterize the channel impulse response mathematically. The physical models may not describe the channel accurately with a low number of parameters, however

[193]. The analytical models can be accurate, but only for the specified scenario. Nevertheless, physical models seem to have gained more interest. Two different physical channel models were used in the generation of simulation results in this thesis. A stochastic small-scale fading model [194] is used for the majority of the thesis. The geometry-based stochastic Winner channel model [195] is employed to verify the channel estimation results in Chapter 5. The Winner model was also used in [65] to compare different detection algorithms.

The typical urban (TU) channel [194, 196] with base station (BS) azimuth spread of 2 or 5 degrees was applied in most of the work. The simulator for the MIMO fading channel model was introduced in [194] and it includes temporal, spatial and spectral correlation. The TU channel parameters are shown in Table 1. Slightly different path delays and powers were used for the generated channels in Chapters 4 and 5. The spatial correlation matrix for the receiver can be written as

$$\mathbf{C}_{RX} = \begin{bmatrix} 1 & -0.7+0.34j & 0.49-0.36j & -0.38+0.34j \\ -0.7+0.34j & 1 & -0.7+0.34j & 0.49-0.36j \\ 0.49-0.36j & -0.7+0.34j & 1 & -0.7+0.34j \\ -0.38+0.34j & 0.49-0.36j & -0.7+0.34j & 1 \end{bmatrix}, \tag{9}$$

where each element corresponds to the correlation between the first antenna and each of the next four antennas. For a 2×2 antenna case, the first two elements of the matrix are used. The spatial correlation matrix for the transmitter depends on the BS azimuth spread. For BS azimuth spread of 2 degrees, the first row of the matrix is $[1; 0.8+0.3j; 0.42+0.44j; 0.14+0.39j]$, and for BS azimuth spread of 5 degrees, the first row is $[1; 0.46+0.2j; 0.13+0.15j; 0.03+0.09j]$. The correlation matrix $\mathbf{C}_{TX}$ for the transmitter can be formed from the vectors in a similar manner as in $\mathbf{C}_{RX}$. The channel spatial correlation model can be obtained from $\mathbf{C}_{TX} \otimes \mathbf{C}_{RX}$, where $\otimes$ is the Kronecker product. The channel with BS azimuth spread of 2 degrees is denoted as a correlated channel and with 5 degrees as a moderately correlated channel. In addition, a spatially uncorrelated channel is considered as well. The base station antenna separation is 4 λ and the mobile station (MS) antenna separation is $\lambda/2$.

The Winner channel model [195] was used for part of the results in Chapter 5. The channel parameters are presented in Table 2. The Winner C1 suburban macro-cell channel with no line-of-sight (NLOS) components and a line-of-sight (LOS) component were used. The Winner channel models are based on channel measurements. The suburban macro-cell mobile stations are outdoors and the base stations are above rooftops. The model generates more taps for the LOS channel than the NLOS channel

Table 1. TU channel model parameters.

	Chapter 4	Chapters 5,6
Number of paths	6	6
Path delays (ns)	[0,200,500,1600,2300,5000]	[0,310,710,1090,1730,2510]
Path power	$-$[3,0,2,6,8,10] dB	$-$[0,1,9,10,15,20] dB
BS antenna spacing	4 λ	4 λ
MS antenna spacing	$\lambda/2$	$\lambda/2$
BS average AoD	50 $^\circ$	50 $^\circ$
MS average AoA	67.5 $^\circ$	67.5 $^\circ$
BS azimuth spread	2 $^\circ$ / 5 $^\circ$	2 $^\circ$ / 5 $^\circ$
MS azimuth spread	35 $^\circ$	35 $^\circ$

as the delays are longer and the number of clusters is higher.

Table 2. Winner C1 channel model parameters.

	LOS	NLOS
Number of clusters	15	14
Path delays (ns)	[0,...,960]	[0,...,770]
Path power	$-$[0,...,32.6] dB	$-$[3,...,22.4] dB
BS antenna spacing	4 λ	4 λ
MS antenna spacing	$\lambda/2$	$\lambda/2$
Cluster departure azimuth spread	5 $^\circ$	2 $^\circ$
Cluster arrival azimuth spread	5 $^\circ$	10 $^\circ$

4 Detection in MIMO-OFDM systems

Different detection algorithms and their implementations for MIMO-OFDM systems are presented in this chapter. The performance of the algorithms is compared via computer simulations. The performances are compared both with a fixed modulation and coding scheme and in schemes with adaptive transmission. Perfect CSI at the receiver is assumed in this chapter. The complexities of the detector algorithms are obtained via very-large-scale integration (VLSI) implementations.

The communication system performance is characterized by frame error rate, which is usually transformed to data transmission throughput. The frame is defined to be erroneous when it contains erroneous bits. Given an ideal automatic repeat request (ARQ) procedure, the transmission throughput is decreased with every re-transmission. The transmission throughput is then defined to be equal to the nominal information transmission rate of information bits times (1-FER). In other words, the throughput measure characterizes the rate and the reliability. However, in real systems, the number of ARQ re-transmissions would be limited. The latency of the implementation is also analyzed, and reflected as a detection rate of a particular implementation. The detection rate refers to the nominal rate by which the algorithm can make data decisions, but it tells nothing about the reliability of the decisions. When both the throughput and detection rate are considered, the performance of the algorithm can be evaluated more reliably. Even though the transmission throughput of an algorithm can be high, the detector may not be able to process the data with the required speed. The definition for goodput in this work differs from the one generally used in network theory for application level throughput [197]. The minimum of the detection rate and transmission throughput is referred to as goodput in this chapter. When combined with the complexity and power consumption of the algorithm, the cost and performance of different algorithms can be compared.

The main contributions of this chapter are provision of a performance-complexity comparison of selected detection algorithms for MIMO-OFDM and evaluation of the detection algorithms, also in a system with adaptive transmission. A modification to the K-best tree search is presented and an algorithm combining a tree search algorithm and interference cancellation is introduced.

The chapter is organized as follows: the system model was presented in Section

3.1, where transmission adaptation is also briefly addressed. Section 4.1 presents the optimal ML and MAP detection methods. LMMSE and interference cancellation are discussed in Section 4.2 and tree search detection algorithms are introduced in Section 4.3. Performance of different types of detectors is compared in Section 4.4 and their implementation complexities are presented in Section 4.5. Finally, the results are discussed in Section 4.6. The chapter contains some previously published material. The simulation results from Sections 4.4.2, 4.4.3 and 4.4.4 were published in [62] and part of the results from Section 4.4.6 was published in [63]. The algorithm description in 4.3.3 or the related simulation results in 4.4.5 have not been previously published, however. The implementation results in Section 4.5 were generated for this thesis, but the architecture descriptions and similar results have been published [62, 63] with the exception of the tree search comparison in Section 4.5.5.

4.1 ML and MAP detection

The ML detection method minimizes the average error probability and it is the optimal method for finding the closest lattice point [17]. The ML detector calculates the Euclidean distances (EDs) between the received signal vector $\mathbf{y}$ and lattice points $\mathbf{Hx}$, and returns the vector $\mathbf{x}$ with the smallest distance, i.e. it minimizes

$$\hat{\mathbf{x}}_{\mathrm{ML}} = \arg\min_{\boldsymbol{x}\in\Omega^N} ||\mathbf{y} - \mathbf{Hx}||^2. \tag{10}$$

The ML detector performs an exhaustive search over all possible lattice points and the complexity is exponential in N.

The ML detector is optimal for uncoded systems, but for coded systems, as pointed out in Section 2.1.2, APPs for the decoder are required. The optimal receiver would perform detection and decoding jointly, but its complexity would be prohibitive as it depends on the length of the code block [102]. The optimal receiver is then approximated with an iterative receiver [96]. A structure of such a receiver is presented in Figure 4. The detector calculates *a posteriori* soft output values L_{D1} using the *a priori* information L_{A1}. The contribution of the *a priori* information is subtracted from L_{D1} to obtain the extrinsic information L_{E1}. The soft in soft out (SISO) decoder uses the de-interleaved L_{E1} as *a priori* information L_{A2} to produce the *a posteriori* values L_{D2}. The extrinsic information L_{E2} is again obtained by subtracting the *a priori* values from the *a posteriori* values. The interleaved L_{E2} can then be used as *a priori* information for the detector.

The MAP detector provides the optimal APPs or LLRs [95] for the decoder. The *a*

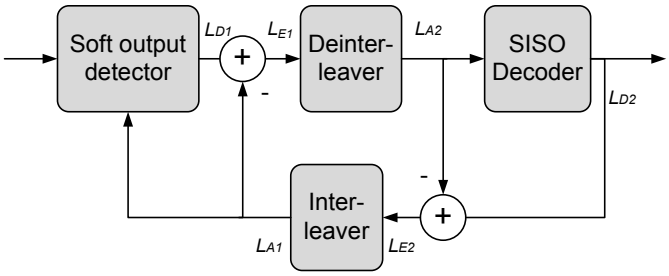

Fig. 4. The iterative receiver.

posteriori LLR $L_D(b_k)$ for the transmitted bit k is

$$L_D(b_k|\mathbf{y}) = \ln\frac{\Pr(b_k=+1|\mathbf{y})}{\Pr(b_k=-1|\mathbf{y})}. \tag{11}$$

Given the interleaving of $\mathbf{b}$, the bits are approximately statistically independent and $L_D(b_k|\mathbf{y})$ can be written as [102]

$$L_D(b_k|\mathbf{y}) = L_A(b_k) + \underbrace{\ln\frac{\sum_{\mathbf{b}\in\mathbb{B}_{k,+1}} p(\mathbf{y}|\mathbf{b})\exp(\frac{1}{2}\mathbf{b}_{[k]}^T\mathbf{L}_{A,[k]})}{\sum_{\mathbf{b}\in\mathbb{B}_{k,-1}} p(\mathbf{y}|\mathbf{b})\exp(\frac{1}{2}\mathbf{b}_{[k]}^T\mathbf{L}_{A,[k]})}}_{L_E(b_k|\mathbf{y})}, \tag{12}$$

where $\mathbb{B}_{k,a}$ is the set of 2^{NQ-1} bit vectors having $b_k = a, a \in \{-1,1\}$, $\mathbf{b}_{[k]}$ is a subvector of $\mathbf{b}$ without b_k and vector $\mathbf{L}_{A,[k]}$ includes all L_A values except for b_k. The likelihood function $p(\mathbf{y}|\mathbf{b})$ can be written as

$$p(\mathbf{y}|\mathbf{b}) = \exp(-\frac{1}{2\sigma^2}||\mathbf{y}-\mathbf{H}\mathbf{x}||^2) \tag{13}$$

when the noise in the system is white Gaussian. The complexity of (12) can be reduced by only considering a subset of $\mathbb{B}_{k,a}$. With (12) and (13), $L_E(b_k|\mathbf{y})$ can be rewritten as

$$L_E(b_k|\mathbf{y}) = \ln\frac{\sum_{\mathbf{b}\in\mathscr{L}_{k,+1}} \exp(-\frac{1}{2\sigma^2}||\mathbf{y}-\mathbf{H}\mathbf{x}||^2 + \frac{1}{2}\mathbf{b}_{[k]}^T\mathbf{L}_{A,[k]})}{\sum_{\mathbf{b}\in\mathscr{L}_{k,-1}} \exp(-\frac{1}{2\sigma^2}||\mathbf{y}-\mathbf{H}\mathbf{x}||^2 + \frac{1}{2}\mathbf{b}_{[k]}^T\mathbf{L}_{A,[k]})}, \tag{14}$$

where $\mathscr{L}_{k,+1}\bigcap\mathbb{B}_{k,+1}$ is a list of candidate points $\mathbf{x}$. The list $\mathscr{L}$ can be obtained by neglecting the insignificant elements in $\mathbb{B}$ such that the K candidate points in $\mathscr{L}$ include

$\hat{\mathbf{x}}_{\mathrm{ML}}$ and $2^{MQ} > K \geq 1$ [102]. This can be achieved for example with a list sphere detector.

The approximation of the logarithm in $L_E(b_k|\mathbf{y})$ can be calculated using a small look-up table and the Jacobian logarithm [198]

$$\mathrm{jacln}(a_1, a_2) := \ln(e^{a_1} + e^{a_2}) = \max(a_1, a_2) + \ln(1 + \exp(-|a_1 - a_2|)). \quad (15)$$

The Jacobian logarithm in (15) can be computed without the logarithm or exponential functions by storing $r(|a_1 - a_2|)$ in a look-up table, where $r(\cdot)$ is a refinement of the approximation $\max(a_1, a_2)$. Max-log approximation further simplifies (14) when the refinement term is left out with negligible loss in performance. With these simplifications, (14) can be written as

$$\begin{aligned} L_E(b_k|\mathbf{y}) = &\max_{b \in \mathcal{L}_{k,+1}} \left\{ -\frac{1}{2\sigma^2}||\mathbf{y} - \mathbf{H}\mathbf{x}||^2 + \frac{1}{2}\mathbf{b}_{[k]}^T \mathbf{L}_{A,[k]} \right\} \\ &- \max_{b \in \mathcal{L}_{k,-1}} \left\{ \frac{1}{2\sigma^2}||\mathbf{y} - \mathbf{H}\mathbf{x}||^2 + \frac{1}{2}\mathbf{b}_{[k]}^T \mathbf{L}_{A,[k]} \right\}. \end{aligned} \quad (16)$$

4.2 Linear detection and interference cancellation

4.2.1 LMMSE detection

The linear MMSE filter can be calculated as

$$\mathbf{W} = (\mathbf{H}^{\mathrm{H}}\mathbf{H} + \sigma^2 \mathbf{I}_M)^{-1}\mathbf{H}^{\mathrm{H}} = \mathbf{G}^{-1}\mathbf{H}^{\mathrm{H}}, \quad (17)$$

where $\mathbf{H}$ is the channel matrix, σ^2 is the noise variance, $(\cdot)^{\mathrm{H}}$ is the complex conjugate transpose and $\mathbf{I}_M$ is a $M \times M$ identity matrix. The received signal vector is then filtered to obtain the equalized signals as

$$\hat{\mathbf{x}}_{MMSE} = \mathbf{W}\mathbf{y}. \quad (18)$$

As discussed in Section 2.1.1, the LMMSE detector minimizes the mean square error between the output $\hat{\mathbf{x}}_{MMSE}$ and the transmitted signal $\mathbf{x}$. The LMMSE filter can also be calculated using an extended channel matrix $\underline{\mathbf{H}} \in \mathbb{C}^{(M+N)\times N}$ [199] as

$$\mathbf{W} = (\underline{\mathbf{H}}^{\mathrm{H}}\underline{\mathbf{H}})^{-1}\underline{\mathbf{H}}^{\mathrm{H}}, \quad (19)$$

where the extended channel matrix and received vector $\underline{\mathbf{y}} \in \mathbb{C}^{(M+N)}$ can be expressed as

$$\underline{\mathbf{H}} = \begin{bmatrix} \mathbf{H} \\ \sigma \mathbf{I}_N \end{bmatrix} \quad \text{and} \quad \underline{\mathbf{y}} = \begin{bmatrix} \mathbf{y} \\ \mathbf{0}_{N\times 1} \end{bmatrix} \quad (20)$$

and $\mathbf{0}_{N\times 1}$ denotes a vector of zeros. The equalized signals can then be obtained from

$$\hat{\mathbf{x}}_{MMSE} = \underline{\mathbf{H}}^{+}\underline{\mathbf{y}}, \tag{21}$$

where $(\cdot)^{+}$ denotes the Moore-Penrose pseudo-inverse of the matrix [200]. The bias in the LMMSE filter can be removed by $\mathbf{W} = \mathbf{B}\mathbf{G}^{-1}\mathbf{H}^{\mathrm{H}}$ [112], where $\mathbf{B}$ is a diagonal matrix with i,ith element

$$B_{i,i} = \frac{\rho_i + 1}{\rho_i}. \tag{22}$$

The SINR on stream i can be calculated as [17]

$$\rho_i = \frac{1}{\sigma^2 \mathbf{G}^{-1}_{i,i}} - 1. \tag{23}$$

Matrix inversion

The matrix inversion required in the LMMSE filter calculation can be calculated with different approaches. The direct approach is used for the 2×2 antenna system in this work. The direct matrix inversion is calculated as

$$\mathbf{G}^{-1} = \frac{1}{|\mathbf{G}|}\begin{bmatrix} g_{2,2} & -g_{1,2} \\ -g_{2,1} & g_{1,1} \end{bmatrix}. \tag{24}$$

The positive semi-definite nature of the matrix $\mathbf{G}$ in (17) simplifies the calculation of the matrix inverse. The determinant $|\mathbf{G}|$ is a real valued and no complex division is required.

The direct approach can, however, be too complex for large matrices. The QR decomposition can be utilized in the matrix inversion. Two methods are used to calculate the LMMSE filter in this work. The squared Givens rotations (SGR) [201] are used for calculating the inverse of $\mathbf{G}$. The modified Gram-Schmidt algorithm [200] is employed to perform a QR decomposition on the extended channel matrix $\underline{\mathbf{H}} = \underline{\mathbf{Q}}\underline{\mathbf{R}}$, where $\underline{\mathbf{R}} \in \mathbb{C}^{(M+N)\times N}$ has orthonormal columns and $\underline{\mathbf{R}} \in \mathbb{C}^{N\times N}$ is an upper triangular matrix. The LMMSE filter is then obtained from

$$\mathbf{W} = \underline{\mathbf{R}}^{-1}\underline{\mathbf{Q}}^{\mathrm{H}}. \tag{25}$$

The modified Gram-Schmidt algorithm is described as Algorithm 1. The factorization can also be performed with sorting in order to obtain an optimal detection order [202]. The sorted QRD (SQRD) can be used as a basis for interference cancellation in a

V-BLAST architecture or instead of the conventional QRD used as preprocessing in tree search algorithms.

Algorithm 1. Modified Gram-Schmidt

Input: $\underline{\mathbf{H}}$
Outputs: $\underline{\mathbf{Q}}, \underline{\mathbf{R}}$
$\underline{\mathbf{Q}} = \underline{\mathbf{H}}$
for $i = 1,...,N$
  $norm_i = ||\underline{\mathbf{h}}_i||^2$
end
for $i = 1,...,N$
  $\underline{r}_{i,i} = \sqrt{norm_i}$
  $\underline{\mathbf{q}}_i = \underline{\mathbf{q}}_i / \underline{r}_{i,i}$
  for $j = i+1,...,N$
    $\underline{r}_{i,j} = \underline{\mathbf{q}}_i^{\mathrm{H}} \underline{\mathbf{q}}_j$
    $\underline{\mathbf{q}}_j = \underline{\mathbf{q}}_j - \underline{r}_{i,j} \underline{\mathbf{q}}_i$
    $norm_j = norm_j - \underline{r}_{i,j}^2$
  end
end

The SGR algorithm is used to calculate the inverse of $\mathbf{G}$, after which the result has to be multiplied with $\mathbf{H}^{\mathrm{H}}$. The decomposition of the $M \times M$ matrix with squared Givens rotations can be written as [201]

$$\mathbf{G} = \mathbf{Q}_A \mathbf{D}_U^{-1} \mathbf{U}_R, \tag{26}$$

where $\mathbf{Q}_A = \mathbf{Q}\mathbf{D}_R \in \mathbb{C}^{M \times M}$, $\mathbf{D}_U = \mathbf{D}_R^2 \in \mathbb{R}^{M \times M}$, $\mathbf{U}_R = \mathbf{D}_R \mathbf{R} \in \mathbb{C}^{M \times M}$ and $\mathbf{D}_R = \mathrm{diag}(\mathbf{R}) \in \mathbb{R}^{M \times M}$. Equation (18) can be rewritten as

$$\begin{aligned}
\mathbf{Q}_A^{\mathrm{H}} \mathbf{G} \hat{\mathbf{x}}_{MMSE} &= \mathbf{Q}_A^{\mathrm{H}} \mathbf{H}^{\mathrm{H}} \mathbf{y} \\
\mathbf{D}_R \mathbf{Q}^{\mathrm{H}} \mathbf{G} \hat{\mathbf{x}}_{MMSE} &= \mathbf{Q}_A^{\mathrm{H}} \mathbf{H}^{\mathrm{H}} \mathbf{y} \\
\mathbf{D}_R \mathbf{Q}^{\mathrm{H}} \mathbf{Q} \mathbf{D}_R \mathbf{D}_U^{-1} \mathbf{U}_R \hat{\mathbf{x}}_{MMSE} &= \mathbf{Q}_A^{\mathrm{H}} \mathbf{H}^{\mathrm{H}} \mathbf{y} \\
\mathbf{D}_R^2 \mathbf{D}_R^{-2} \mathbf{U}_R \hat{\mathbf{x}}_{MMSE} &= \mathbf{Q}_A^{\mathrm{H}} \mathbf{H}^{\mathrm{H}} \mathbf{y} \\
\hat{\mathbf{x}}_{MMSE} &= \mathbf{U}_R^{-1} \mathbf{Q}_A^{\mathrm{H}} \mathbf{H}^{\mathrm{H}} \mathbf{y},
\end{aligned} \tag{27}$$

where $\mathbf{Q}_A$ and $\mathbf{U}_R$ are obtained with the SGR. Since $\mathbf{U}_R$ is an upper triangular matrix, its inversion can be obtained through back substitution or with an algorithm presented in [203]. The latter was used in this work and the algorithm is presented as Algorithm 2.

Algorithm 2. Inversion of triangular matrix

Input: $\mathbf{U}_R$
Output: $\mathbf{U}_R^{-1}$
$\mathbf{A} = \mathbf{0}_{M\times M}$
for $i = 1,...,M$
  $\mathbf{A}_{i,i} = \frac{1}{\mathbf{U}_{R_{i,i}}}$
end
for $i = 1,...,M-1$
  for $j = i+1,...,M$
    $t = 0$
    for $k = 1,...,j-1$
      $t = t + \mathbf{A}_{i,k}\mathbf{U}_{R_{k,j}}$
    end
    $\mathbf{A}_{i,j} = -t\mathbf{A}_{j,j}$
  end
end
$\mathbf{U}_R^{-1} = \mathbf{A}$

LLR calculation

The log-likelihood ratios for the FEC decoder can be calculated with a soft demodulator which takes as input the LMMSE equalizer outputs $\hat{\mathbf{x}}_{MMSE}$, the equivalent channel $\mathbf{H}_e = \mathrm{diag}(\mathbf{WH})$ and the covariance of the residual interference $\mathbf{N}_0 = \mathbf{H}_e - \mathbf{H}_e\mathbf{H}_e^{\mathrm{H}}$. The process of producing LLRs with the soft demodulator is described as Algorithm 3.

Algorithm 3. Soft demodulation

Inputs: $\mathbf{H}_e, \mathbf{N}_0, \hat{\mathbf{x}}_{MMSE}$
Output: LLR
for $k = 1, ..., N$
  for $i = 1, ..., Q$
  $s_1 = s_0 = -\infty$
    for $j = 1, ..., \Omega$
      $d = \hat{\mathbf{x}}_{MMSE_k} - \mathbf{H}_{ek} x_j$
      $di = |d|^2$
      $lm = -di/\mathbf{N}_{0k}$
      if $b_{i,j} = 1$
        $s_1 = \text{maxx}(s_1, lm)$
      else
        $s_0 = \text{maxx}(s_0, lm)$
      end
    end
    $LLR_{ki} = s_1 - s_0$
  end
end
Function $c = \text{maxx}(a, b)$
  if $a > b$
    $c = a + \log(1 + e^{-|a-b|})$
  else
    $c = b + \log(1 + e^{-|a-b|})$
  end

The LLRs can be calculated from the LMMSE equalizer outputs $\hat{\mathbf{x}}_{MMSE}$ as presented in [112] by using an approximate log-likelihood criterion. Instead of calculating the Euclidean distance between the LMMSE equalizer output and the possible transmitted symbols as in Algorithm 3, Gray labeling of the signal points is exploited. This reduces the latency and complexity but was shown to have only a minor impact on the performance. The bit-metric approximations $\hat{L}(b^j|\hat{\mathbf{x}}, \mathbf{W})$ in [112] are calculated as

$$\rho_k \Lambda(b^j, \hat{\mathbf{x}}) = \min_{\tilde{x}_k \in \mathbb{X}_{k,j}^{-1}} |\hat{x}_k - \tilde{x}_k|^2 - \min_{\tilde{x}_k \in \mathbb{X}_{k,j}^{1}} |\hat{x}_k - \tilde{x}_k|^2, \tag{28}$$

where $k = \lfloor j/Q \rfloor + 1$, $\mathbb{X} = \{x_k : b^j = i\}$ is the subset of hypersymbols $\{x\}$ for which the jth bit of label b is i and ρ_k is the SINR of layer k. $\Lambda(b^j, \hat{\mathbf{x}})$ can be simplified by considering $\hat{x}_k$ in only one quadrature dimension given by j. The symbol mapping of real symbols to LLR values with 64-QAM is shown in Figure 5. For example, the first bit is one in the positive side of the axis and zero on the negative size. The LLR then grows based on how far the symbol value is from zero. The same process applies to the imaginary parts of the symbols.

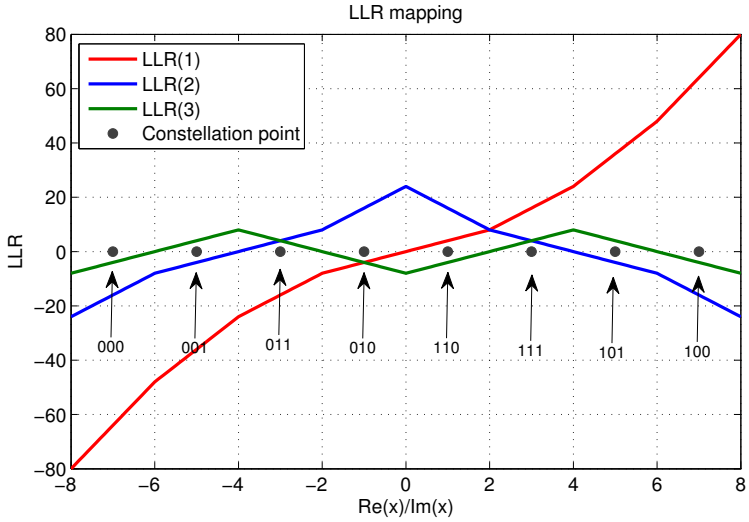

Fig. 5. The mapping of symbols to LLRs.

4.2.2 The SIC algorithm

Instead of jointly detecting signals from all the antennas, the strongest signal can be detected first and its interference is cancelled from each received signal in the SIC receiver. Then, the second strongest signal is detected and cancelled from the remaining signals, and so on. The detection method is called successive nulling and interference

cancellation [22], as discussed in Section 2.1.1. With the horizontal layering of the encoded streams, the detected layers can be decoded separately. Therefore, decoding can be performed only on the strongest layer first and on the remaining layers after interference cancellation.

The soft SIC receiver is illustrated in Figure 6. The first layer is detected with the LMMSE detector. The LLR block calculates LLRs from the LMMSE equalizer outputs. The deinterleaved stream is decoded with a turbo decoder and symbol expectations are calculated. The expectations are cancelled from the second layer, which is then decoded. The layer detected in the first iteration is not updated during the second iteration.

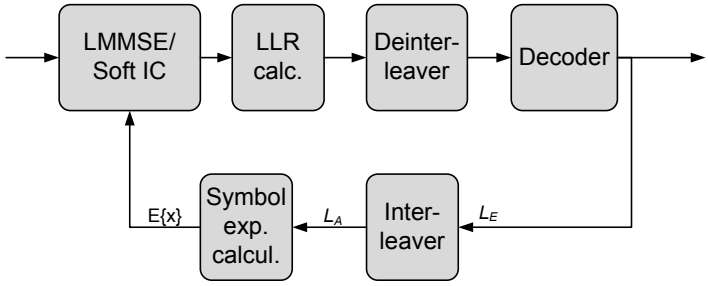

Fig. 6. The soft IC receiver ([62], published by permission of IEEE).

The weight matrix is calculated with the LMMSE algorithm. The layer for detection can be chosen according to the post-detection SNR and the corresponding nulling vector is chosen from the weight matrix $\mathbf{W}$ [22]. All the weight matrices in an OFDM symbol are calculated and the layer to be detected is chosen according to the average over all the subcarriers. The metric for the layer selection on the kth stream over the subcarriers can be calculated as

$$\gamma_k = \sum_{p=1}^{P} [(\mathbf{H}_p^{\mathrm{H}} \mathbf{H}_p + \sigma^2 \mathbf{I})^{-1}]_{kk}. \tag{29}$$

The layers can then be ordered according to the magnitude of γ_k.

After the first iteration, the cancelled symbol expectation is used to update the weight matrix. The weight matrix on the second iteration is calculated as

$$\mathbf{W} = (E\{x\}E\{x\}^* \mathbf{h}_k \mathbf{h}_k^{\mathrm{H}} + \mathbf{H}_k(\mathbf{I} - (E\{x\}E\{x\}^*)\mathbf{H}_k^{\mathrm{H}} + \sigma^2 \mathbf{I}_M))^{-1} \mathbf{h}_k^{\mathrm{H}}, \tag{30}$$

where $\mathbf{h}_k$ is the kth vector from matrix $\mathbf{H}$, k is the layer to be detected, $\mathbf{H}_k$ is matrix

H with the vectors from previously detected layers removed and $E\{x\}$ is the symbol expectation.

The detected layer is decoded and symbol expectations from the soft decoder outputs are calculated as [204]

$$E\{x\} = (\frac{1}{2})^Q \sum_{x_l \in \Omega} x_l \prod_{i=1}^{Q} (1 + b_{i,l} \tanh(L_A(b_i)/2)), \tag{31}$$

where $L_A(b_i)$ are the LLRs of coded bits corresponding to x and $b_{i,l}$ are bits corresponding to constellation point x_l. The expectation calculation in (31) can be simplified to the form

$$E\{x\}_{\text{re}} = \text{sgn}(L_A(b_i))S|\tanh(L_A(b_{i+2}))|. \tag{32}$$

The constellation point S is chosen from {1,3,5,7} depending on the signs of $L_A(b_{i+1})$ and $L_A(b_{i+2})$.

4.3 Tree search algorithms

The search over the lattice points can be performed with a tree structure due to the QR decomposition applied on the channel matrix. The sphere detector is a well known and commonly used tree search based algorithm for MIMO detection. The SD algorithms solve the ML solution with a reduced number of considered candidate symbol vectors as stated in Section 2.1.2. They take into account only the lattice points that are inside a sphere of a given radius. The condition that the lattice point lies inside the sphere can be written as

$$||\mathbf{y} - \mathbf{H}\mathbf{x}||^2 \leq C_0. \tag{33}$$

After QR decomposition of the channel matrix **H** in (69), it can be rewritten as

$$||\mathbf{y}' - \mathbf{R}\mathbf{x}||^2 \leq C_0', \tag{34}$$

where $C_0' = C_0 - ||(\mathbf{Q}')^{\text{H}}\mathbf{y}||^2$, $\mathbf{y}' = \mathbf{Q}^{\text{H}}\mathbf{y}$, $\mathbf{R} \in \mathbb{C}^{N \times N}$ is an upper triangular matrix with positive diagonal elements, $\mathbf{Q} \in \mathbb{C}^{M \times N}$ and $\mathbf{Q}' \in \mathbb{C}^{M \times (M-N)}$ are orthogonal matrices.

The squared partial Euclidean distance (PED) of $\mathbf{x}_i^N$, i.e. the square of the distance between the partial candidate symbol vector and the partial received vector, can be calculated as

$$d(\mathbf{x}_i^N) = \sum_{j=i}^{N} \left| y_j' - \sum_{l=j}^{N} r_{j,l} x_l \right|^2, \tag{35}$$

where $i = N \ldots, 1$, $y_j^{'}$ is the jth element of $\mathbf{y}'$, $r_{j,l}$ is the j,lth element of the matrix $\mathbf{R}$, x_l is the lth element of the candidate vector $\mathbf{x}_i^N$ and $\mathbf{x}_i^N$ denotes the last $N-i+1$ components of vector $\mathbf{x}$ [86].

List sphere detectors can be used to approximate the MAP detector and to provide soft outputs for the decoder [102]. A list of candidates $\mathscr{L}$ and their Euclidean distances are used to calculate the *a posteriori* probabilities L_D of the coded bits in $\mathbf{b}_p$.

A LSD structure is presented in Figure 7. The channel matrix $\mathbf{H}$ is first decomposed as $\mathbf{H} = \mathbf{QR}$ in the QR-decomposition block. The Euclidean distances between the received signal vector $\mathbf{y}$ and the possible transmitted symbol vectors are calculated in the LSD block. The candidate symbol list $\mathscr{L}$ from the LSD block is demapped to a binary form. The LSD block can be substituted with any tree search algorithm that produces a list of candidate symbols. The log-likelihood ratios are calculated from the list of Euclidean distances in the LLR block. Limiting the range of LLRs reduces the required list size [205].

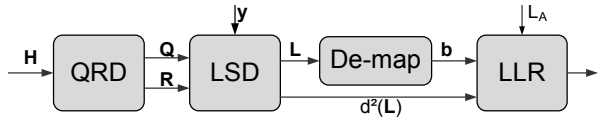

Fig. 7. The list sphere detector ([62], published by permission of IEEE).

4.3.1 The K-best LSD algorithm

The tree search can be performed in a breadth-first, depth-first or metric-first manner, as discussed in Section 2.1.2. The breadth-first approach is considered in this thesis because it can be easily pipelined and parallelized and provides a fixed detection rate. The breadth-first K-best LSD can also be more easily implemented and provide the high and constant detection rates required in the LTE. The K-best algorithm [88] is a breadth-first search based algorithm, which keeps the K nodes which have the smallest accumulated Euclidean distances at each level. If the PED is larger than the squared sphere radius C_0, the corresponding node will not be expanded. No sphere constraint is assumed, i.e. $C_0 = \infty$, but a set the value for K is used instead, as is common with the K-best algorithms. The K-best algorithm without the sphere constraint can also be seen as the M-algorithm [87]. The K-best LSD algorithm description is given as Algorithm 4.

The main loop of the algorithm runs from $i = 1, ..., 2N$ in a real valued system.

Algorithm 4. The K-best LSD algorithm

Inputs: $\mathbf{Q}, \mathbf{R}, \mathbf{y}$, C_0', K, P (modulation used, P-QAM)
Preprocessing:
  Calculate: $\mathbf{y}'$
Algorithm:
for $i = 1, ..., N$
1. Denote the partial candidate by $\mathbf{x}_{i+1}^N$.
    1.1 Determine all admissible candidate child nodes x_i with given C_0'
      and calculate the corresponding PEDs $d(\mathbf{x}_i^N)$.
    1.2 Store the partial candidates and their PEDs to a temporary stack memory.
2. Sort the partial candidates according to their PEDs and store the K smallest PEDs and the corresponding symbol vectors to the final list stack memory.
end
Give the candidates and their EDs as outputs.

The K-best tree search with no sphere constraint is illustrated in Figure 8. A list size of two is assumed. The tree search proceeds level by level, expanding all the child nodes of each parent node. If the number of child nodes exceeds the list size, sorting is performed to find the K nodes with the smallest partial Euclidean distances. The tree search starts from the top of the tree on the first level in the figure. Both nodes are spanned, and on the second level, all the child nodes are spanned as well. Sorting is performed to find the two nodes with the smallest PEDs. The tree search continues until the fourth level is reached and the two leaf nodes with the smallest Euclidean distances are given as output.

Enhanced tree search

The breadth-first tree search can be modified to decrease the latency. With the novel search strategy [64], two or more PEDs can be calculated in parallel and the largest ones are discarded. With 64-QAM, instead of having to sort 64 PEDs, there are only 32 PEDs to be sorted on each level when two PEDs are calculated in parallel. On the first level, the PEDs are calculated as with the original breadth-first search, as shown in Figure 9.

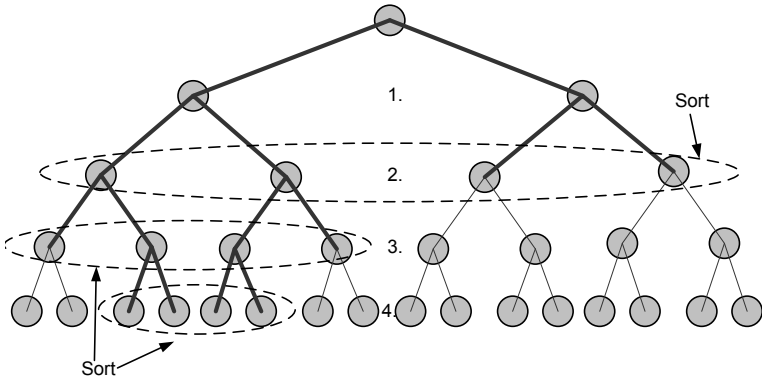

Fig. 8. The K-best tree search.

On subsequent levels, half the nodes are discarded before sorting, as shown in the figure, as lighter nodes.

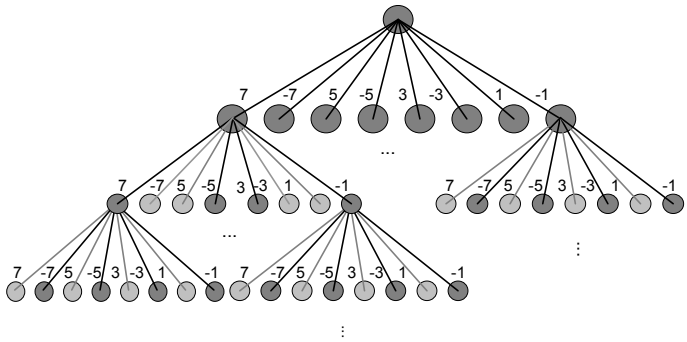

Fig. 9. The modified tree search ([62], published by permission of IEEE).

4.3.2 Selective spanning with fast enumeration

The selective spanning with fast enumeration algorithm [135] can also be thought of as a breadth-first tree search algorithm. The algorithm spans each level of the tree based on the node spanning vector $\mathbf{m} = [m_1, ..., m_M]$. The number of spans for each node on a level is specified with the element of $\mathbf{m}$ corresponding to that level. As the spanned nodes are not discarded, the length of the final candidate list can be obtained by multiplying the elements of $\mathbf{m}$. For example, in a 2×2 antenna and 64-QAM system,

the vector $\mathbf{m} = [64, 8]$ would lead to a final candidate list of 512. For the same real valued system, the vector $\mathbf{m} = [8, 8, 8, 8]$ would lead to a final list size of 4,096. In practice, smaller list sizes should be aimed at. In this work, a real valued system model is used. Such a system model simplifies the Euclidean distance calculation and the slicing operation as the closest constellation point selection can be done on a one dimensional axis.

The PED on each level of the tree search can be calculated as

$$d_i(\mathbf{x}^i) = d_{i+1}(\mathbf{x}^{i+1}) + \left\| e_i(\mathbf{x}^i) \right\|^2, \tag{36}$$

where $d_{i+1}(\mathbf{x}^{i+1})$ is the PED from the previous level and $i = N, ..., 1$. The slicer unit selects a set of closest constellation points $\mathbf{x}^i$, minimizing

$$\left\| e_i(\mathbf{x}^i) \right\|^2 = \left\| \underbrace{y_i' - \sum_{j=i+1}^{M} r_{i,j} x_j}_{b_{i+1}(\mathbf{x}^{i+1})} - r_{i,i} x_i \right\|^2. \tag{37}$$

Minimizing $\left\| e_i(\mathbf{x}^i) \right\|^2$ is equivalent to the minimization of $\| e_i(\mathbf{x}^i)/r_{ii} \|^2$

$$\left\| \frac{e_i(\mathbf{x}^i)}{r_{i,i}} \right\|^2 = \left\| \underbrace{b_{i+1}(\mathbf{x}^{i+1})/r_{i,i}}_{\varepsilon} - x_i \right\|^2. \tag{38}$$

The closest constellation points based on ε are selected in the slicer unit.

The real valued axis for 64-QAM is shown in Figure 10. The slicing order given ε is also depicted. If five constellation points are sliced, the slicer would select the constellation points in the order of $\{5, 3, 7, 1, -1\}$. The process is similar to the Schnorr-Euchner enumeration (SEE). The SSFE algorithm could then be thought of as the M-algorithm combined with SEE. The SSFE algorithm does not require sorting, which makes it more attractive for implementation than the M-algorithm or the K-best detector. The SSFE algorithm is summarized as Algorithm 5.

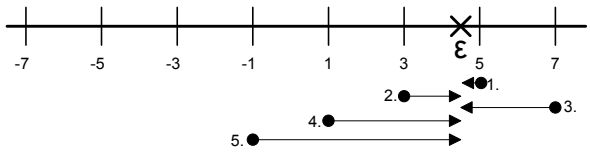

Fig. 10. The slicing operation in SSFE with 64-QAM.

Algorithm 5. The SSFE algorithm

Inputs: $\mathbf{Q}, \mathbf{R}, \mathbf{y}$, $\mathbf{m}$, P (modulation used, P-QAM)
Preprocessing:
  Calculate: $\mathbf{y}'$
  Calculate: $\mathbf{h}_i = 1/\mathbf{R}_{i,i}$
Algorithm:
for $i = 1, ..., N$
1. Calculate ε for each candidate in $\mathbf{x}^i$
2. Slice the $\mathbf{m}_i$ closest points
3. Calculate the PEDs to the sliced lattice points
end
Give the candidates and their EDs as outputs.

4.3.3 Tree search with interference cancellation

A system with two separately encoded streams in the 4×4 antenna case is assumed. If MMSE-SIC is used, two strongest layers are cancelled from the other two layers and only MMSE is used in separating the two strongest or weakest layers. This can degrade the performance, especially in low rank channels. A tree search algorithm can be used to separate the streams, which were not used for interference cancellation. In the SSFE-SIC algorithm, the strongest stream is detected with the SSFE detector. The LLRs are calculated from the final list and decoding is performed. The tree search has to be performed for the whole received symbol vector in the first iteration to achieve a sufficiently good performance. Symbol expectations can be calculated from the outputs of the decoder as in (31). The symbol expectations are cancelled from the receiver symbol vector with $\mathbf{r} = \mathbf{y} - \mathbf{H}E\{\mathbf{x}\}$. A partial tree search is performed on $\mathbf{r}$ in order to separate the final two streams.

4.4 Numerical throughput examples

4.4.1 Simulation model

The communication system, i.e. the transmission throughput performance of the SIC detector, is compared to that of the K-best LSD and the LMMSE detectors. The simulation parameters are based on the LTE standard [189] and are summarized in Table 3. In the horizontally encoded system, two data streams are encoded separately and then mapped onto different layers. The strongest layer can be detected and decoded first and then cancelled from the remaining layer. In the 4×4 antenna system, each of the two streams is multiplexed onto two antennas; the first stream is multiplexed onto the first and second antenna and the second stream onto the third and fourth antenna. The most recent versions of the 3GPP LTE specifications also include the 2×2 vertically encoded case, where a single code word is multiplexed onto two layers. In this scenario, decoding of the layers cannot be performed separately.

The transmission throughput is calculated as the nominal information transmission rate of information bits times (1−FER). A 5 MHz bandwidth was assumed in the simulations. The signal-to-noise ratio represents E_s/N_0, where E_s is the symbol energy. Each SNR point includes transmission of 1,000 frames. Perfect channel state information was assumed in the receiver. The number of turbo decoder iterations in the simulations was eight. The typical urban (TU) channel [194, 196] with base station (BS) azimuth spread of 2 or 5 degrees was applied. The channel with BS azimuth spread of 2 degrees is denoted as a correlated channel and with 5 degrees as the moderately correlated channel, as explained in Section 3.4. A spatially uncorrelated channel was considered as well. Parameters of the used channel models were shown in Table 1.

Table 3. Simulation parameters.

Coding	Turbo coding with 1/2 code rate
Channel model	Typical urban
User velocity	30, 120 km/h
Number of subcarriers	512 (300 used)
Bandwidth	5 MHz
Symbol duration	71.4 μs

4.4.2 2×2 MIMO system

The throughput performances of the LMMSE, SIC and K-best detectors with 4-QAM, 16-QAM and 64-QAM and two transmit and receive antennas are illustrated in Figures 11–13. The highly correlated TU channel is applied in Figure 11 and a spatially uncorrelated channel in Figure 12; both figures assume horizontal encoding denoted as H-BLAST. A moderately correlated channel and vertical coding (denoted as V-BLAST) was assumed in Figure 13. A real valued signal model was assumed in the K-best LSD and QRD of the channel matrix $\mathbf{H}$ with no sorting of the layers.

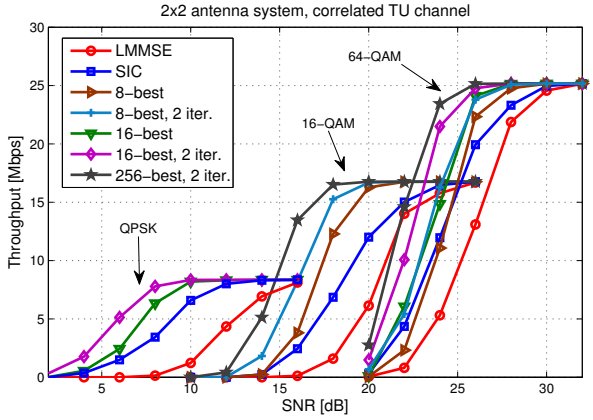

Fig. 11. Data transmission throughput vs. SNR in a 2×2 H-BLAST system and correlated TU channel ([62], published by permission of IEEE).

The results in Figure 11 show that the K-best LSD outperforms the SIC receiver with all modulations under high correlation. Only the 8-best LSD with 64-QAM performs worse than the SIC in low SNRs. Using the turbo decoder outputs to update the LLRs in the LSD receiver improves the performance by roughly 1 dB compared to the LSD without any iterations. With 64-QAM, approximately the same performance is achieved with 8-best and two iterations as with 16-best without iterations. Performing interference cancellation improves the performance up to 4 dB compared to the LMMSE receiver. Turbo decoding for the bit LLRs is performed once both in the SIC receiver and the K-best receiver with no iterations. The iterative K-best LSD includes turbo decoding of the bit LLRs twice.

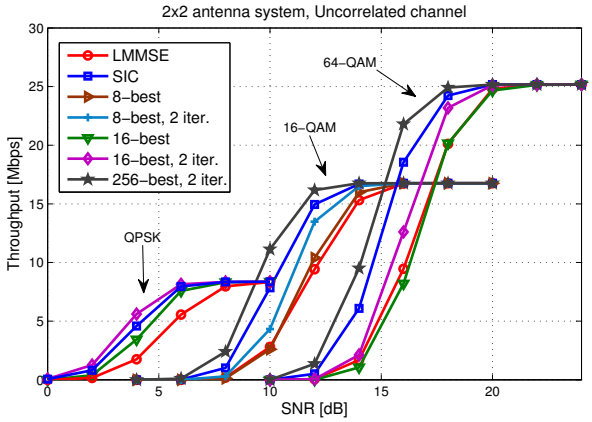

Fig. 12. Data transmission throughput vs. SNR in a 2×2 H-BLAST system and uncorrelated channel ([62], published by permission of IEEE).

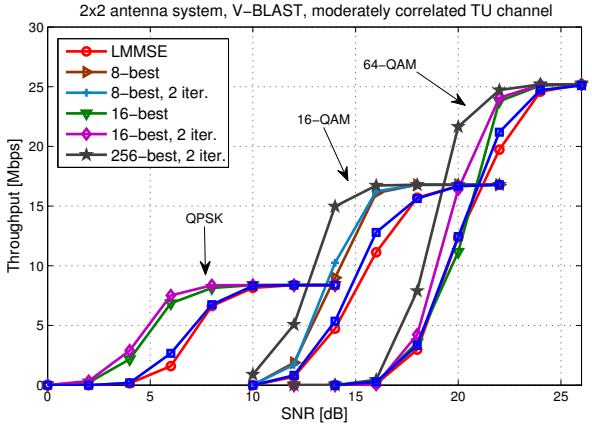

Fig. 13. Data transmission throughput vs. SNR in a 2×2 V-BLAST system and moderately correlated channel ([62], published by permission of IEEE).

The SIC receiver also outperforms the K-best LSD when the channel has no correlation, as presented in Figure 12. With highly correlated channels, the initial decisions in the SIC receiver are more likely to be incorrect, which is found to lead to error propagation.

The SIC receiver improves the performance of the LMMSE receiver only very marginally in the vertically encoded system, as illustrated in Figure 13. This is

understandable and not surprising at all, because both layers have to be decoded before soft interference cancellation can be performed. Thus, the SIC receiver provides no benefit compared to the plain LMMSE receiver in the vertically encoded case, and it will be considered for the horizontally encoded case only in the sequel. The K-best LSD, on the other hand, performs similarly to the horizontally encoded case.

4.4.3 4×4 MIMO system

The data transmission throughput vs. SNR with four transmit and receive antennas is presented in Figure 14. Two streams are encoded separately and the first stream is multiplexed onto the first two antennas and the second stream onto the third and fourth antenna [189]. Two iterations are performed with the SIC receiver. The symbols from the strongest layers are detected and decoded first and then cancelled from the remaining layers. The streams from the spatially multiplexed layers are separated only with the LMMSE equalizer in the SIC receiver. Interference cancellation is performed only between the two horizontally encoded streams. In the correlated TU channel, the K-best LSD outperforms the SIC and LMMSE receivers. In the uncorrelated channel, the difference in performance is smaller and the SIC receiver outperforms the K-best LSD. This is due to the fact that the LMMSE detector is able to separate the MIMO streams under low correlation and the feedback from the decoder is more likely to be correct. With moderate correlation, the SIC performance is close to that of the K-best LSD. The performance of the SIC receiver is worse in the 4×4 antenna case than in the 2×2 case because cancellation is performed between the two streams and only LMMSE detection is used in the vertically encoded streams. This is due to the encoding structure, which was described in the beginning of Section 4.4.

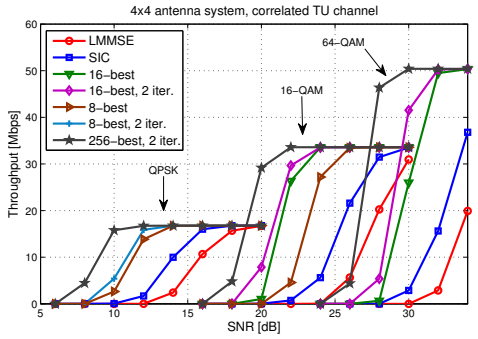

(a)

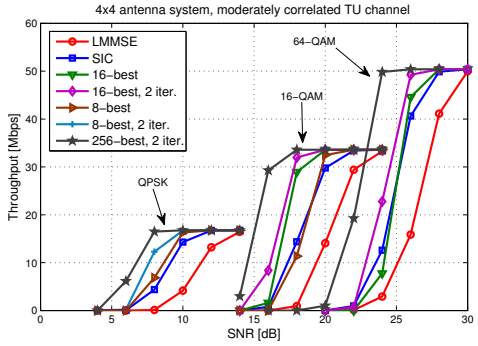

(b)

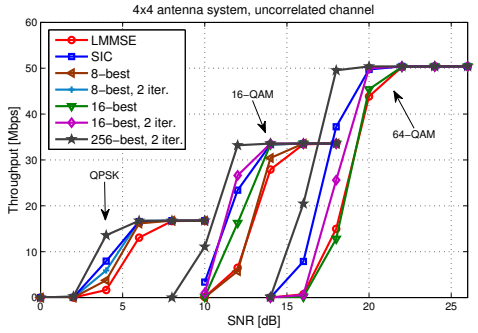

(c)

Fig. 14. Data transmission throughput vs. SNR in a 4×4 system in (a) a highly correlated (b) moderately correlated and (c) uncorrelated channel ([62], published by permission of IEEE).

4.4.4 Preprocessing, enhanced tree search and LLR calculation

Different methods for the QRD in the tree search algorithms can be applied. The basic QRD decomposes the channel matrix $\mathbf{H}$, while the MMSE-QRD performs QR decomposition on the extended channel matrix $\underline{\mathbf{H}}$. The MMSE-SQRD improves the performance by including the noise term in the preprocessing. The sorted QRD sorts the channel matrix according to its column norms while performing the QRD [110]. This approach leads to an improved tree search order where the best layer is expanded first. The SQRD can also be performed on the extended channel matrix to further improve the performance. The FER performances of the different preprocessing approaches are presented in Figure 15 in a 4×4 16-QAM case. The K-best LSD with the list sizes of 4, 8 and 16 was used as the tree search algorithm. Including the noise variance in the preprocessing has a high impact on the performance. It can be seen from the fact that the highest performance gain is obtained by the extended channel matrix. Sorting in the QRD brings only a little additional gain. Also, the larger the list size, the lower the impact of the preprocessing. With more complex preprocessing, even small list sizes can be used.

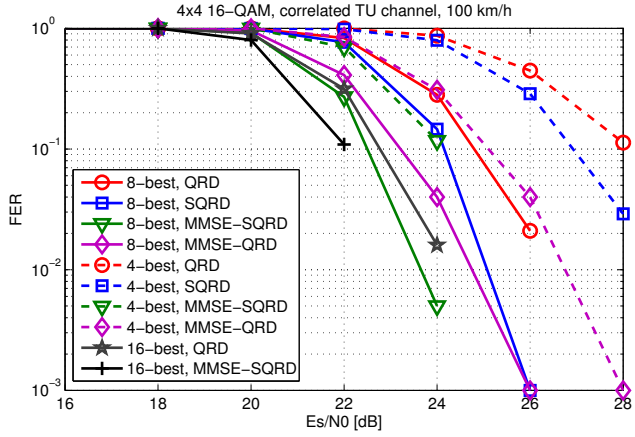

Fig. 15. FER vs. SNR in a 4×4 system in a highly correlated channel with different QRD preprocessors.

The impact of the enhanced tree search described in Section 4.3.1 on the performance in a 2×2 64-QAM case is shown in Figure 16. It can be seen that the performance degradation is minimal, but the detection rate will be doubled. The new strategy is the most beneficial with high order modulations, when the nodes have several branches. When a lower order modulation is used, the performance degrades more with the new strategy because a smaller amount of bit combinations is included in the LLR calculation.

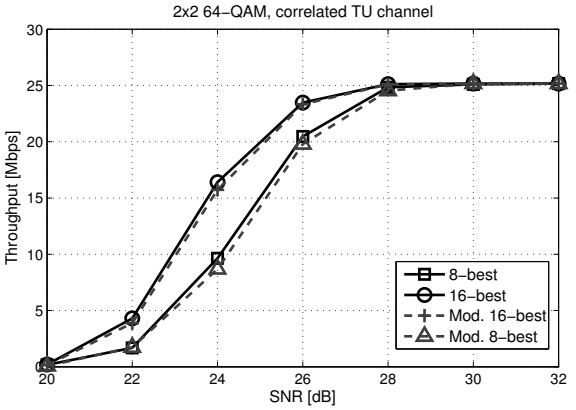

Fig. 16. Data transmission throughput vs. SNR in a 2×2 system in a highly correlated channel with the modified tree search ([62], published by permission of IEEE).

The LLR calculation in the K-best LSD is simplified from (15) by leaving out the refinement part from (15). The impact of using the simplified LLR calculation is presented in Figure 17. The simplification has again only a small impact on the performance. Comparison of implementation estimations showed that the complexity is reduced approximately four times with the simplified LLR calculation. Also the SIC receiver is simplified from using soft demodulation presented as Algorithm 3 for LLR calculation compared to using the approximate log-likelihood criterion. The symbol expectations are also calculated with (32).

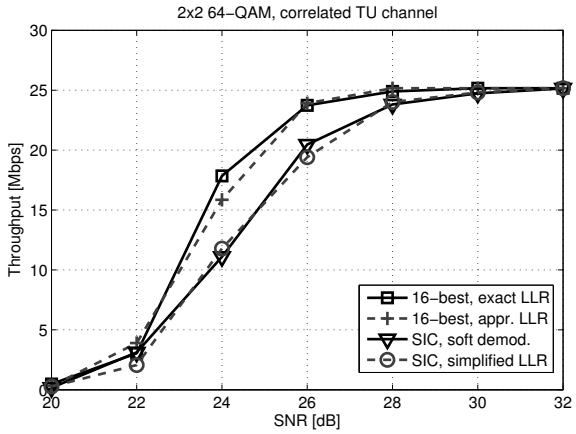

Fig. 17. Data transmission throughput vs. SNR in a 2×2 system in a highly correlated channel with the simplified LLR calculation ([62], published by permission of IEEE).

4.4.5 Performance comparison of K-best and SSFE

The performances of the tree search algorithms with different list sizes are compared in Figures 18 and 19. The performance of the SSFE-SIC algorithm from Section 4.3.3 is also shown. The SSFE node spanning vector $\mathbf{m}$ is shown in the figure for the first four levels of the real valued tree search. In the last four levels, only one node is expanded. The last value of $\mathbf{m}$ corresponds to the first level in the tree. A 4×4 antenna system with 16-QAM and a correlated channel is assumed in Figure 18. There, the K-best with the list size of 16 and 8-best with two iterations perform best. The performance of the SSFE-SIC is degraded by the incorrect symbol decisions from the decoder feedback. SSFE with one global iteration and a final list size of 12 has a performance difference of almost 2 dB compared to the 8-best. The SSFE may not always find the best branches on each level, but the K-best detector goes through all the child branches on a level and finds the ones with the smallest distances. The SSFE detector also goes through only one branch in the bottom levels of the tree.

A 4×4 antenna system with 64-QAM and a moderately correlated channel is assumed in Figure 19. The difference in performance is smaller than in the correlated

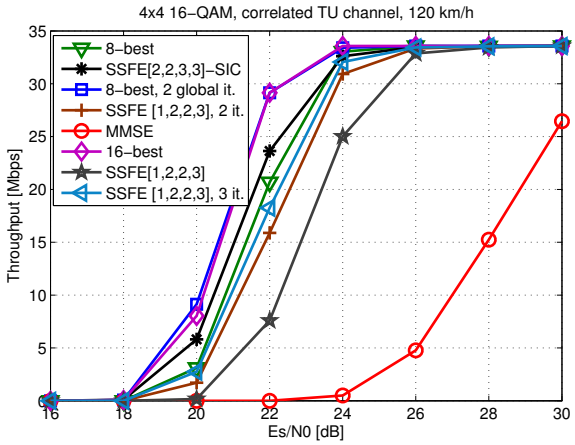

Fig. 18. Data transmission throughput vs. SNR of K-best and SSFE in a correlated channel with 4×4 16-QAM.

channel. The best performance is obtained with the SSFE-SIC algorithm with a sufficiently large tree search size. Updating of the LLRs gives a good performance with both K-best and SSFE. Even though the SSFE might be better suitable for implementation, the performance of the SSFE is still worse than that of the K-best. Therefore, as the K-best algorithm gives the most constant performance in most scenarios, it will be the main tree search algorithm considered in the remainder of the thesis. Nevertheless, detailed complexity comparisons are provided in Section 4.5.5.

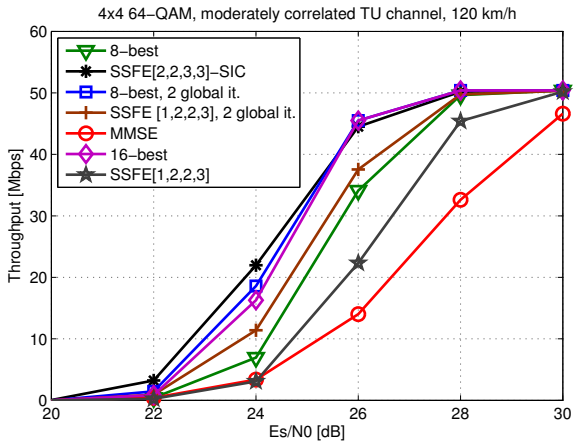

Fig. 19. Data transmission throughput vs. SNR of K-best and SSFE in a moderately correlated channel with 4×4 64-QAM.

4.4.6 Performance with AMC

The performances of the receiver algorithms with adaptive transmission are compared in this section. The capacity metric for adaptation is used, but several other metrics also exist. The goal is to study the impact of adaptation on the performance of the receiver algorithms and not to find the ideal adaptation metric, which is an open research topic.

In the simulations with AMC, a 5 MHz bandwidth was used and a correlated typical urban channel with BS azimuth spread of 2 degrees was applied. The user velocity was 30 km/h. The modulations used in the AMC scheme were QPSK, 16-QAM and 64-QAM and the code rates were 1/3, 1/2, 2/3, 3/4 and 4/5. The precoding matrices from [189] were used. The transmission was adapted by calculating the capacity at the receiver as in (6) and sending the suggested CQI to the transmitter. The extended channel matrix is used in the QRD for the K-best detectors.

The performance of the LMMSE receiver in a 4×4 system with different fixed modulation, coding schemes and transmission ranks is presented in Figure 20. The throughput with adaptive modulation and coding and precoding is also shown. Precoding improves the throughput from the fixed MCS upper bound up to 5 dB because it finds the best precoding weights for the transmission streams. In the 2×2 antenna system, the performance is not greatly improved with precoding.

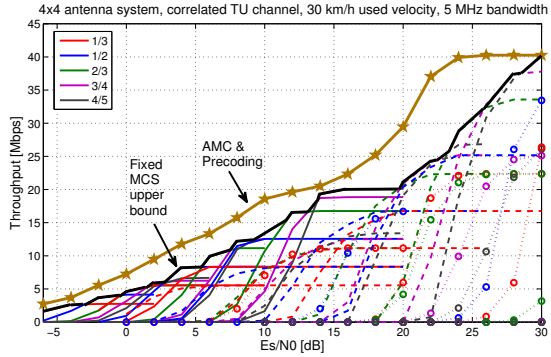

Fig. 20. Data transmission throughput vs. SNR with fixed MCSs and AMC with precoding ([63], published by permission of IEEE).

The performance of the receiver algorithms with AMC is presented in Figure 21 in a 2×2 antenna case. The transmission was adapted to use mostly rank 1 transmission in the lower SNRs. When rank 2 transmission is used, the K-best LSD receiver with a list size of 8 performs the best and the LMMSE receiver has the worst performance. Updating the LLRs from the decoder improves the performance of the K-best by 1 dB. Since the transmission is already adapted to the channel, a better receiver does not give a high gain in performance.

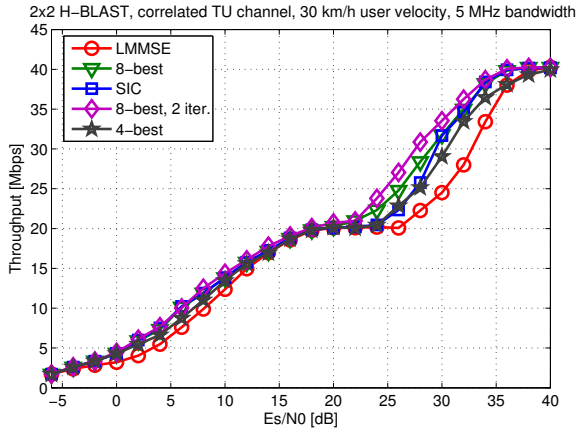

Fig. 21. Data transmission throughput vs. SNR in a correlated 2×2 channel ([63], published by permission of IEEE).

The performance of the algorithms in a channel with less correlation than in Figure 21 is shown in Figure 22. The difference in performance is smaller when the channel conditions are improved. The same was seen in the fixed modulation and code rate cases earlier in the chapter. With lower correlation in the channel and transmission adapted to the channel conditions, a simpler receiver also succeeds in separating the MIMO streams.

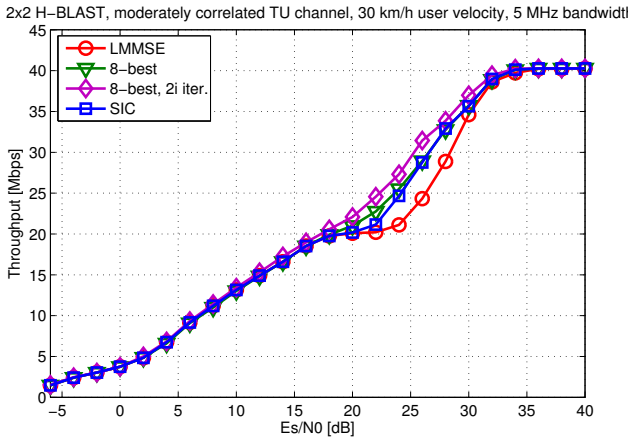

Fig. 22. Data transmission throughput vs. SNR in a moderately correlated 2×2 channel ([63], published by permission of IEEE).

The performance in a 4×4 antenna system is shown in Figure 23. The transmission rank of the precoding matrix was one, two or four. The performances of the algorithms are similar with rank one transmissions as in the 2×2 antenna system. With higher SNRs and transmission rank, the performance improves with the more complex receivers. The SIC receiver does not improve the performance much from the LMMSE in the high SNRs when rank 4 transmission is used. This is partly due to the encoding structure and the two strongest streams are cancelled from the other streams and only MMSE is used to separate the remaining streams. However, the LSD receivers improve the performance greatly with rank 4 transmission since a more advanced detector is needed to separate the streams.

The performance difference of LMMSE and K-best in a 4×4 antenna system with all the ranks from one to four is illustrated in Figure 24. The performance difference between the receivers is smaller from Figure 23 when the additional rank is utilized in

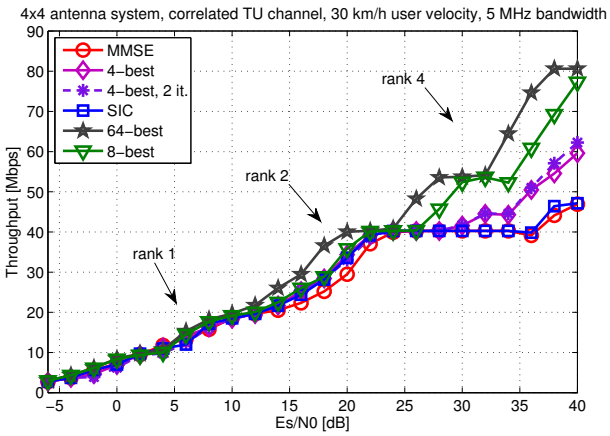

Fig. 23. Data transmission throughput vs. SNR in a 4×4 system with AMC and precoding with transmission ranks 1, 2 and 4 ([63], published by permission of IEEE).

the transmission. However, there is still a several dB performance difference in the higher SNRs. What is more, the adaptation process is more time consuming with all transmission ranks. The capacity has to be calculated with 64 different combinations of the precoding matrices and transmission ranks.

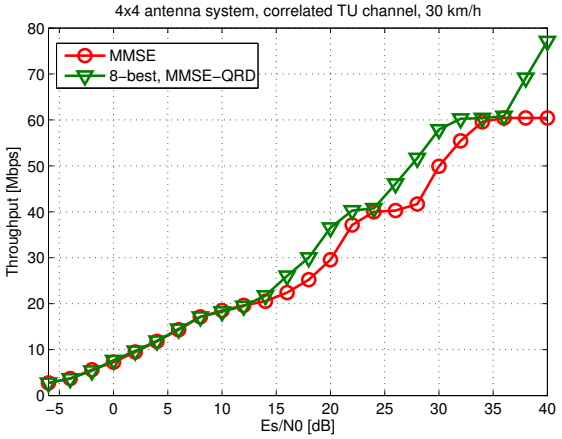

Fig. 24. Data transmission throughput vs. SNR in a 4×4 system with AMC and precoding with transmission ranks 1-4.

4.5 Implementation results

The theoretical complexity of the receivers with $M = N$ is presented in Table 4, where the number of multiplication and addition operations is specified. In the squared Givens rotations (SGR) and the Gram-Schmidt based QRD, the division and square root were approximated with additions and shifts [206]. The largest term in the SGR comes from matrix multiplications and in the QRD from multiple iterations of vector multiplications. The number of operations in the K-best algorithm depends on the list size K. If K is larger than $\sqrt{|\Omega|}^{(l-1)}$, it is used as K. In the first level l, the number of multiplications is $2\sqrt{|\Omega|}$ and additions $\sqrt{|\Omega|}$. The LLR calculation operations for the linear receivers depend on the modulation. The constant multiplications with a power of 2 were calculated as shifts. The number of multiplications is lower in the K-best LSD than in the SIC with 4×4 QPSK. The number of multiplications in the K-best algorithm increases with the list size and modulation. The modulation order does not have a major impact on the complexity with the SIC receiver. The impact of this can be seen later in the implementation results. The SIC receiver includes more multiplications than the K-best algorithm with 4×4 QPSK and the implementation gate count is also higher. With 64-QAM, the number of multiplications and gates is higher with the K-best.

As discussed in Section 2.4, the implementation results were generated with the Catapult C HLS tool. The FPGA complexity results are presented in slices and dedicated digital signal processing (DSP) slices. The DSP slices include an 18×18-bit multiplier. The VHDL from Catapult C was synthesized to a Xilinx Virtex-5 FPGA with Mentor Graphics Precision Synthesis. The ASIC results are presented in gate equivalents (GE) and power consumption estimates. The Synopsys Design Compiler was used in synthesizing the VHDL along with the UMC 0.18 μm complementary metal oxide semiconductor (CMOS) technology.

Simulations were performed to confirm that the used word lengths did not result in performance degradation compared to the floating point word lengths. The most critical part in terms of word lengths in the detector is the preprocessing, i.e. the QRD or LMMSE. Figure 25 includes simulation results for both the LMMSE detector and the K-best LSD with the list size of 16. In the K-best, the word lengths in the tree search and LLR calculation are 16 bits. The word lengths in the QRD are from 18 to 20 bits. The LMMSE filter calculation was performed with the extended channel matrix as in (19). The need to increase the word lengths in the LMMSE filter increases with the SNR. The 26 bit word length in the division and square root operations and the 24 bit

Table 4. The theoretical complexity of the receivers as numbers of arithmetic operations ([62], published by permission of IEEE).

Block	Multiplications	Additions
$(\mathbf{H}^{\mathrm{H}}\mathbf{H}+\sigma^2\mathbf{I}_M)$	$4M^3$	
SGR $(\mathbf{Q},\mathbf{R})$	$4M^3$+$4.5M^2$+$7.5M$-12	
MMSE-QRD $(\underline{\mathbf{Q}},\underline{\mathbf{R}})$	$2M(16M^3-6M^2+M+5)$	$32M^4-20M^3+62M^2+86M$
$\mathbf{R}$ inverse	$\sum_{j=1}^{M-1} j^2$	
$\mathbf{R}^{-1}\mathbf{QH}$	$8M^3$	
Detection	$4M^2$	$3M^2-M$
LLR (MMSE/SIC)	[2|8|16]M	$MQ/4$
Expectation calc.	$4M$	
SIC	$2M^2+4M$	$4M^2-M$
QRD	$2M(8M^3-2M^2+3M+1)$	$16M^4-12M^3+66M^2+86M$
Matrix-vector mult.	$4M^2$	$4M^2-2M$
K-best LSD	$\sum_{l=2}^{2M} K\sqrt{\lvert\Omega\rvert}(l+1)$	$K\sum_{l=2}^{2M}\sqrt{\lvert\Omega\rvert}(l+1)$
LLR (K-best)	K	$QM+32$

word length in the matrix elements is enough for the lower SNRs, but higher word lengths are required for the higher SNRs. However, the high SNRs may not be feasible in the LMMSE detector and a compromise can be used to lower the complexity of the LMMSE filter while maintaining a good performance in the lower SNRs.

4.5.1 Preprocessing

Preprocessing of the channel matrix is utilized in every detector type in this thesis. The LMMSE and SIC detectors require the LMMSE filter calculation and the tree search detectors need the results from the QR decomposition of the channel matrix. Two preprocessing methods were considered in Section 4.2. The SGR based QRD is used for the LMMSE coefficient calculation and the Gram-Schmidt algorithm is employed to perform the QRD on the channel matrix. The Gram-Schmidt process is also utilized in the LMMSE filter calculation for the extended channel matrix.

A simplified architecture for the SGR based LMMSE filter calculation is presented in Figure 26. The dashed rectangle represents $M/2(M-1)$ iterations with the operations

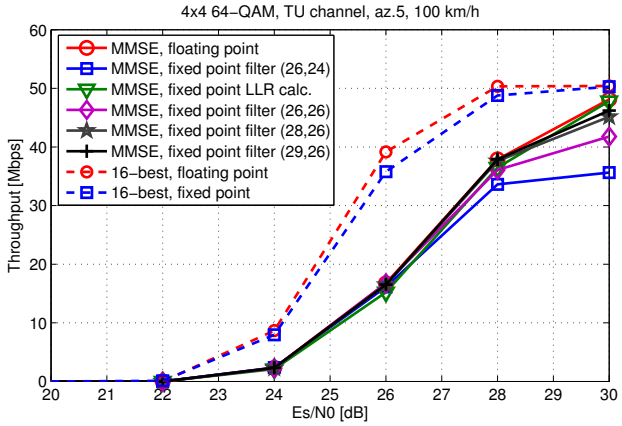

Fig. 25. Data transmission throughput vs. SNR with 4×4 64-QAM fixed point arithmetics.

inside the rectangle. After the iterations, the outputs $\mathbf{Q}_A$ and $\mathbf{U}_R$ are used to calculate the final coefficient matrix $\mathbf{W}$. The upper triangular matrix $\mathbf{U}_R$ is inverted, after which the coefficient matrix is obtained as $\mathbf{W} = \mathbf{U}_R^{-1}\mathbf{Q}_A^{\mathrm{H}}\mathbf{H}^{\mathrm{H}}$.

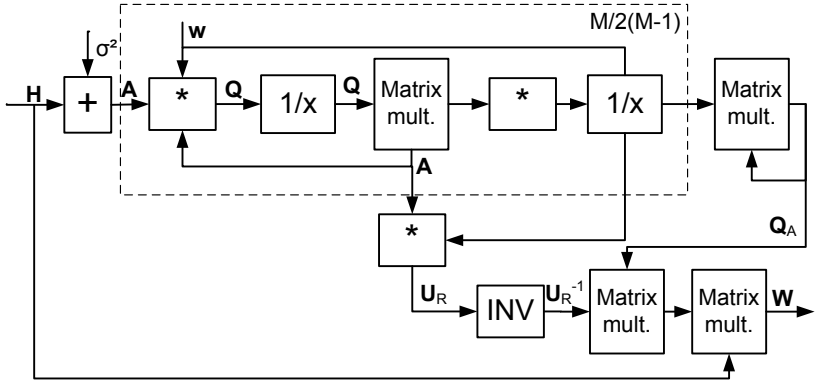

Fig. 26. Architecture of the SGR based calculation of the LMMSE filter.

The architecture of the Gram-Schmidt (GS) QRD is shown in Figure 27. The column norms of the channel matrix $\mathbf{H}$ are calculated first. The following process is then iterated $2M$ times in the case of real valued signal model. The square root and division operations are performed on one norm value in each iteration. The elements

of matrix **R** and columns of matrix **Q** are updated with the multiply and accumulate (MAC) operations. The number of MAC operations is $2M$ with the channel matrix **H** and $4M$ with the extended channel matrix $\underline{\mathbf{H}}$. The updating of **R** and **Q** is iterated as $j = i+1,...,2M$ for each outer iteration i. The iterations increase the latency of the GS QRD unless several intermediate registers are added and the architecture is copied into several stages. If the architecture is used for the LMMSE filter calculation, a matrix multiplication and an inversion of **R** is added.

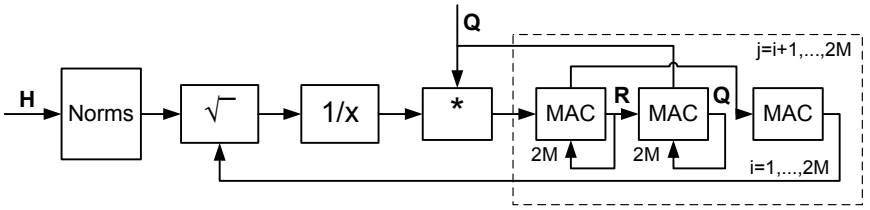

Fig. 27. Architecture of the Gram-Schmidt based QRD.

The implementation results for the 4×4 antenna system preprocessing are shown in Table 5. The table includes implementation results for the Gram-Schmidt QRD in the 8×8 real valued channel matrix and the 8×16 real valued extended channel matrix cases and for the SGR QRD of the complex valued 4×4 channel matrix. Also, the blocks for inversion of the upper triangular matrices and matrix multiplications are included. The word lengths in the GS QRD are from 18 to 20 bits and from 20 to 26 bits for the extended channel matrix. The high word length requirement and increased number of iterations in the extended GS QRD double the power consumption compared to the QRD with the regular channel matrix. The word lengths for the SGR are from 18 to 20 bits as in [187], but some scaling is assumed. However, the numerical accuracy is more problematic with the SGR LMMSE filter and the GS method is utilized in the sequel. When the implementation latencies are roughly the same, the power consumption of the GS LMMSE is higher. A faster SGR was also implemented in the case of the need to calculate all the coefficient matrices before starting the SIC detection. However, it is assumed in the sequel that only a portion of the LMMSE coefficient matrices are needed to determine the SIC detection order and that the order remains the same for a few channel coherence periods. Thus, the GS based QRD is used for preprocessing in the LMMSE, SIC and K-best detectors.

Table 5. The 4×4 preprocessing ASIC implementation results.

Block	Gates	Power	Clock	Latency	Throughput
GS QRD	248.7 k	210.5 mW	125 MHz	175 cc	176 cc
GS QRD	380 k	237 mW	124 MHz	85 cc	40 cc
GS QRD ext.	350.3 k	440 mW	97 MHz	505 cc	504 cc
$\mathbf{R}^{-1}$	38.3 k	41.2 mW	100 MHz	455 cc	456 cc
Matrix mult.	26.4 k	39.9 mW	140 MHz	258 cc	256 cc
SGR QRD	443 k	260 mW	137 MHz	404 cc	400 cc
SGR $\mathbf{U}_R^{-1}\mathbf{Q}_A^{\mathrm{H}}\mathbf{H}^{\mathrm{H}}$	26.2 k	36.3 mW	140 MHz	258 cc	256 cc
SGR QRD	399.5 k	550 mW	124 MHz	63 cc	40 cc
SGR $\mathbf{U}_R^{-1}\mathbf{Q}_A^{\mathrm{H}}\mathbf{H}^{\mathrm{H}}$	84.7 k	126.2 mW	140 MHz	45 cc	40 cc
Total: GS LMMSE	415 k	522 mW	97 MHz	1218 cc	504 cc
Total: SGR LMMSE	469.2 k	296 mW	137 MHz	662 cc	400 cc
Total: SGR LMMSE	484 k	676 mW	124 MHz	108 cc	40 cc

4.5.2 *K*-best LSD

The K-best LSD receiver includes the QRD block, the K-best LSD block and the LLR calculation block. The QR decomposition block is based on the modified Gram-Schmidt QRD algorithm from [110]. Ordering of the channel matrix is not utilized in the architecture. The top level architecture of the K-best LSD for a 2×2 antenna system is shown in Figure 28. The 4×4 antenna system LSD is based on the same architecture, but four more PED calculation blocks and sorters are added to the design.

The K-best LSD architecture is modified from [66]. A 2×2 and a 4×4 antenna system with a real signal model [207] is assumed. The received signal vector $\mathbf{y}$ is multiplied with matrix $\mathbf{Q}$ in the matrix multiplication block. Matrix $\mathbf{R}$ is multiplied with the possible transmitted symbols after the QRD is performed, i.e. when the channel realization changes. Partial Euclidean distances between the last symbol in vector $\mathbf{y}'$ and possible transmitted symbols are calculated in block PED1 in a 2×2 antenna system with $d(\mathbf{x}_4^2) = ||y_4^{'} - r_{4,4}^{'}||^2$. The resulting lists of symbols and PEDs are not sorted at the first stage. The distances are added to the partial Euclidean distances $d(\mathbf{x}_3^2) = ||y_3^{'} - (r_{3,3}^{'} + r_{3,4}^{'})||^2$ calculated in the PED2 block. The lists are sorted and K partial symbol vectors with the smallest PEDs are kept. PED3 block

calculates $d(\mathbf{x}_2^2) = ||y_2^{'} - (r_{2,2}^{'} + r_{2,3}^{'} + r_{2,4}^{'})||^2$, which are added to the previous distance and sorted. The last PED block calculates the partial Euclidean distances $d(\mathbf{x}_1^2) = ||y_1^{'} - (r_{1,1}^{'} + r_{1,2}^{'} + r_{1,3}^{'} + r_{1,4}^{'})||^2$. After adding the previous distances to $d(\mathbf{x}_1^2)$, the lists are sorted and the final K symbol vectors are demapped to bit vectors and their Euclidean distance is used in the LLR calculation.

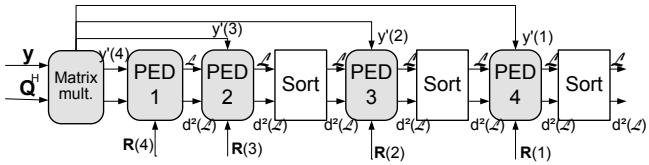

Fig. 28. The top level architecture of the 2×2 K-best LSD ([62], published by permission of IEEE).

The modified K-best LSD tree search was used in the implementation in most of the 64-QAM results. The architecture of the second stage parallel Euclidean distance calculation and insertion sorting is illustrated in Figure 29. Two PEDs are calculated in parallel and the smallest one is added to the list. The latency of each stage is then halved from that of the original K-best tree search.

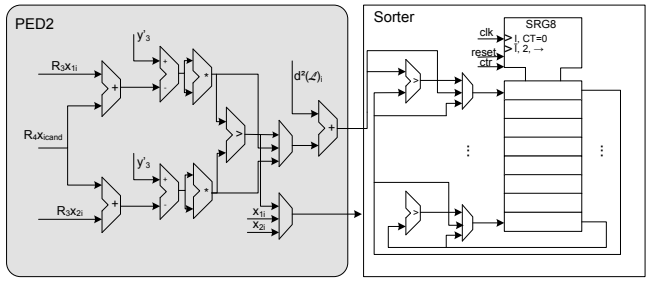

Fig. 29. Parallel PED calculation and sorting ([62], published by permission of IEEE).

The 2×2 FPGA implementation results are shown in Table 6 for the preprocessing, Table 7 for the K-best tree search and Table 8 for the LLR calculation. The 4×4 FPGA implementation results are presented in Table 9 for the preprocessing, Table 10 for the tree search and Table 11 for the LLR calculation. Seven 18 Kbit BRAMs are needed to store the results of the QRD in a 5 MHz bandwidth. In the iterative 2×2 64-QAM 16-best LSD, additional 9 BRAMs are needed to store the list and LLRs from the

previous iteration. The ASIC implementation results are shown in Table 12 for the 2×2 preprocessing, Table 13 for the K-best tree search and Table 14 for the LLR calculation. The 4×4 ASIC implementation results are presented in Tables 15, 16 and 17.

The latency and throughput of each block is expressed in clock cycles (cc). The throughput cycles express the number of cycles after which the block can take a new input, i.e. the pipelined throughput of the block. The QRD was scheduled to be performed in the channel coherence time so that 1,200 subcarriers would be processed during the coherence period. Assuming that the preprocessing can be performed at a different clock frequency than the detection, the maximum velocity for the 2×2 FPGA results would be almost 300 km/h. The velocity can be calculated as

$$v = \frac{3.6 f_{clock} c}{P f_c t p_c}, \tag{39}$$

where f_{clock} is the clock frequency, c is the speed of light, P is the number of subcarriers, f_c is the center frequency and tp_c is the number of throughput cycles. The maximum velocity in the 4×4 FPGA case would then be 95 km/h. The velocities for the preprocessing implemented with the ASIC technology would be 312 km/h in the 2×2 case and 213 km/h in the 4×4 case given a 100 MHz clock frequency. However, the QRD could be clocked at a higher clock frequency.

The word lengths for the K-best LSD and LLR calculation are mainly 16 bits and computer simulations have been performed to confirm that there is no performance degradation [64]. The sorters are insertion sorters. The list size values of 16 and 8 are used in the implementation. The sorters have 16 or 8 registers in which the smallest Euclidean distances are kept during the sorting depending on the list size. A full list is used in the 2×2 QPSK case and no sorting is required. This decreases the complexity of the detector. The LSD is the timing bottleneck in the receiver. The QRD has the highest latency, but it is performed only once in the channel coherence time. The list $\mathscr{L}$ from the first iteration is used in calculating the LLRs in the second iteration. The non-iterative LLR block has the same latency as the K-best block.

The LLR calculation block was designed both for the iterative and non-iterative receiver. Using the decoder soft outputs in calculating the LLRs adds to the complexity. An iterative receiver would include both the LLR block and the iterative LLR block. The iterative LLR block was designed to have the same latency as the LLR block without iterations. However, the latency of the decoder would reduce the data rate of the iterative receiver. If extra iterations are not needed, only one LLR block would be included in the receiver.

Table 6. The 2×2 Preprocessing FPGA implementation results.

Block	Slices	DSPs	Clock	Latency	Throughput
QRD	1136	5	139 MHz	174 cc	175 cc
$1/\sigma^2$	45	1	157 MHz	27 cc	28 cc
4-QAM $\mathbf{Rx}$	151	5	159 MHz	10 cc	11 cc
16-QAM $\mathbf{Rx}$	351	6	137 MHz	23 cc	25 cc
64-QAM $\mathbf{Rx}$	652	6	136 MHz	47 cc	49 cc

Table 7. The 2×2 K-best FPGA implementation results.

Modulation	K	Slices	DSPs	Clock	Latency	Throughput
4-QAM	16	372	12	206 MHz	22 cc	16 cc
16-QAM	16	771	5	189 MHz	151 cc	32 cc
64-QAM	8	1080	15	189 MHz	320 cc	32 cc
64-QAM	16	2427	15	194 MHz	293 cc	64 cc

Table 8. The 2×2 LLR FPGA implementation results.

Modulation	K	Slices	DSPs	Clock	Latency	Throughput
Non-iter.						
4-QAM	16	171	1	206 MHz	35 cc	16 cc
16-QAM	16	247	1	194 MHz	48 cc	32 cc
64-QAM	8	330	1	194 MHz	48 cc	32 cc
64-QAM	16	346	1	195 MHz	125 cc	64 cc
Iter.						
4-QAM	16	196	1	209 MHz	35 cc	16 cc
16-QAM	16	284	1	216 MHz	49 cc	32 cc
64-QAM	8	403	1	194 MHz	49 cc	32 cc
64-QAM	16	425	1	209 MHz	126 cc	64 cc

Table 9. The 4×4 Preprocessing FPGA implementation results.

Block	Slices	DSPs	Clock	Latency	Throughput
QRD	2243	14	96 MHz	377 cc	378 cc
$1/\sigma^2$	45	1	157 MHz	27 cc	28 cc
4-QAM $\mathbf{Rx}$	568	17	137 MHz	36 cc	37 cc
16-QAM $\mathbf{Rx}$	1242	1	93 MHz	73 cc	75 cc
64-QAM $\mathbf{Rx}$	2319	36	104 MHz	40 cc	40 cc

Table 10. The 4×4 K-best FPGA implementation results.

Modulation	K	Slices	DSPs	Clock	Latency	Throughput
4-QAM	8	1800	12	192 MHz	177 cc	16 cc
16-QAM	16	2131	12	183 MHz	315 cc	32 cc
16-QAM	16	3909	12	129 MHz	564 cc	64 cc
64-QAM	8	3016	24	180 MHz	320 cc	32 cc
64-QAM	16	7116	22	220 MHz	607 cc	64 cc

Table 11. The 4×4 LLR FPGA implementation results.

Modulation	K	Slices	DSPs	Clock	Latency	Throughput
Non-iter.						
4-QAM	8	233	1	211 MHz	34 cc	16 cc
16-QAM	8	412	1	194 MHz	48 cc	32 cc
16-QAM	16	423	1	170 MHz	124 cc	64 cc
64-QAM	8	485	1	184 MHz	53 cc	32 cc
64-QAM	16	594	1	211 MHz	125 cc	64 cc
Iter.						
4-QAM	8	233	1	183 MHz	34 cc	16 cc
16-QAM	8	517	1	183 MHz	49 cc	32 cc
16-QAM	16	542	1	190 MHz	126 cc	64 cc
64-QAM	8	750	1	157 MHz	49 cc	32 cc
64-QAM	16	788	1	149 MHz	126 cc	64 cc

Table 12. The 2×2 Preprocessing ASIC implementation results.

Block	Gates	Power	Clock	Latency	Throughput
QRD	39.5 k	36.1 mW	150 MHz	119 cc	120 cc
$1/\sigma^2$	3 k	5 mW	150 MHz	30 cc	31 cc
4-QAM $\mathbf{Rx}$	6.5 k	8.3 mW	100 MHz	10 cc	11 cc
16-QAM $\mathbf{Rx}$	13.7 k	15.4 mW	100 MHz	21 cc	23 cc
64-QAM $\mathbf{Rx}$	24 k	37.1 mW	100 MHz	35 cc	37 cc

Table 13. The 2×2 K-best ASIC implementation results.

Modulation	K	Gates	Power	Clock	Latency	Throughput
4-QAM	16	33.8 k	162 mW	280 MHz	19 cc	16 cc
16-QAM	8	97 k	341 mW	280 MHz	304 cc	32 cc
16-QAM	8	125 k	454 mW	280 MHz	180 cc	16 cc (P)
64-QAM	8	150 k	551.4 mW	280 MHz	311 cc	32 cc (P)
64-QAM	16	217.2 k	717.3 mW	280 MHz	592 cc	64 cc

Table 14. The 2×2 LLR ASIC implementation results.

Modulation	K	Gates	Power	Clock	Latency	Throughput
Non-iter.						
4-QAM	16	10.9 k	43.7 mW	280 MHz	37 cc	16 cc
16-QAM	8	11.3 k	44.7 mW	280 MHz	65 cc	32 cc
64-QAM	8	14.4 k	57.4 mW	280 MHz	65 cc	32 cc
64-QAM	16	17 k	66 mW	280 MHz	129 cc	64 cc
Iter.						
4-QAM	16	10.8 k	42.2 mW	280 MHz	37 cc	16 cc
16-QAM	8	12.5 k	53.5 mW	280 MHz	69 cc	32 cc
64-QAM	8	15.9 k	71.3 mW	280 MHz	66 cc	32 cc
64-QAM	16	18.8 k	78.3 mW	280 MHz	130 cc	64 cc

Table 15. The 4×4 Preprocessing ASIC implementation results.

Block	Gates	Power	Clock	Latency	Throughput
QRD	249 k	211 mW	125 MHz	175 cc	176 cc
$1/\sigma^2$	3 k	5 mW	150 MHz	30 cc	31 cc
4-QAM **Rx**	14 k	17.3 mW	100 MHz	20 cc	40 cc
16-QAM **Rx**	30 k	36 mW	100 MHz	37 cc	40 cc
64-QAM **Rx**	23 k	22.8 mW	100 MHz	43 cc	40 cc

Table 16. The 4×4 K-best ASIC implementation results.

Modulation	K	Gates	Power	Clock	Latency	Throughput
4-QAM	16	33.8 k	162 mW	280 MHz	19 cc	16 cc
16-QAM	8	97 k	341 mW	280 MHz	304 cc	32 cc
16-QAM	8	125 k	454 mW	280 MHz	180 cc	16 cc (P)
16-QAM	16	148.4 k	500 mW	280 MHz	557 cc	64 cc
64-QAM	8	150 k	551.4 mW	280 MHz	311 cc	32 cc (P)
64-QAM	16	217.2 k	717.3 mW	280 MHz	592 cc	64 cc

Table 17. The 4×4 LLR ASIC implementation results.

Modulation	K	Gates	Power	Clock	Latency	Throughput
Non-iter.						
4-QAM	8	11.8 k	51 mW	280 MHz	35 cc	16 cc
16-QAM	8	17.3 k	68 mW	280 MHz	65 cc	32 cc
16-QAM	16	20.2 k	79 mW	280 MHz	129 cc	64 cc
64-QAM	8	21.1 k	87 mW	280 MHz	65 cc	32 cc
64-QAM	16	24.5 k	96.6 mW	280 MHz	129 cc	64 cc
Iter.						
4-QAM	8	12.5 k	54.7 mW	280 MHz	36 cc	16 cc
16-QAM	8	20.9 k	90.7 mW	280 MHz	69 cc	32 cc
16-QAM	16	23.9 k	99.7 mW	280 MHz	133 cc	64 cc
64-QAM	8	29.1 k	130 mW	280 MHz	67 cc	32 cc
64-QAM	16	32.1 k	138 mW	280 MHz	131 cc	64 cc

4.5.3 Soft interference cancellation

The SIC receiver consists of a LMMSE detector, a LLR calculation block, a symbol expectation calculation block and an interference cancellation block, as presented in Figure 6. The top level architecture of the LMMSE detector for a 2×2 antenna system is presented in Figure 30. The channel matrix $\mathbf{H}$ is first multiplied by its complex conjugate transpose and the noise variance σ^2 is added to the diagonal elements. The resulting 2×2 matrix $\mathbf{G}$ is positive definite and symmetric. This simplifies the matrix inversion, which is performed by dividing the elements with the determinant, switching the diagonals and negating the off-diagonal elements. The determinant is real valued and the off-diagonal elements are complex conjugates. Therefore, fewer operations are needed.

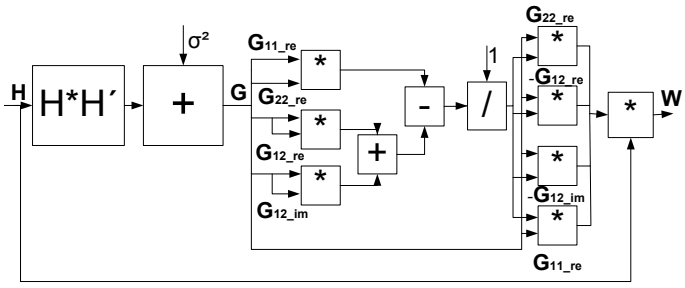

Fig. 30. The top level architecture of the 2×2 LMMSE detector ([62], published by permission of IEEE).

The architecture for the real part of the symbol expectation calculation in the 16-QAM case is presented in Figure 31. The imaginary part is calculated in parallel in the same manner from LLRs $L_A(b_i)$ and $L_A(b_{i+2})$ from the decoder. The lookup table (LUT) is used to find the tanh value.

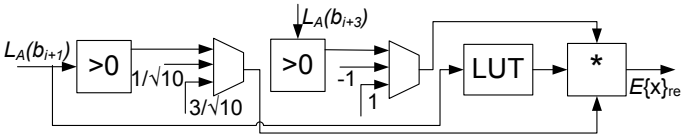

Fig. 31. The architecture of the symbol expectation calculation ([62], published by permission of IEEE).

The complexity of the SIC receiver for a 2×2 system is presented in Table 18 with an FPGA implementation and in Table 20 using ASIC technology. The word lengths were determined with computer simulations. In symbol expectation and LLR calculation blocks, the word lengths range from 6 to 16 bits. In the LMMSE block, word lengths up to 22 bits were used. In addition, four 18-kbit block RAMs are used to store the channel matrix $\mathbf{H}$ and the received symbol vector $\mathbf{y}$ and a BRAM is used in the interleaver. The LLR calculation block also includes detection, i.e. multiplying the received signal with the weight matrix $\mathbf{W}$ and another block for only LLR calculation in the SIC receiver. The clock frequency in the ASIC implementation is 100 MHz and the minimum clock frequency is 126 MHz in the FPGA implementation. The clock frequency on FPGA is limited by the used implementation tools. Higher clock frequencies could be obtained on FPGAs with some optimization.

The complexity of the SIC receiver for a 4×4 system is presented in Table 19 for the FPGA implementation and in Table 21 for the ASIC implementation. The LMMSE detector is the most complex part of the receiver taking 94 percent of the slices and almost 69 percent of the gates. The LMMSE detector is based on the Gram-Schmidt QRD of the extended channel matrix and the LMMSE filter is obtained as in (25). The number of BRAMs needed to store the channel matrix, the weight matrix $\mathbf{W}$ and the received signal is eleven. There are two LLR calculation blocks in the receiver in order to perform the first and second iteration in parallel. The decoder is not included in the total complexity.

The LLR calculation block produces $Q(N/2)$ bit LLRs in the given latency period. $N/2$ symbol expectations for a subcarrier are calculated in the given period. The latencies in the ASIC implementation were set to achieve the detection rates needed to process the data according to LTE time frames in a 20 MHz bandwidth. 20 MHz is the maximum bandwidth in LTE, but lower bandwidths, such as the 5 MHz bandwidth used in the simulations, are also possible.

Table 18. The 2×2 SIC FPGA implementation results.

Block	Modulation	Slices	DSPs	Clock	Latency	Throughput
LMMSE	-	698	13	126 MHz	62 cc	63 cc
LLR	4-QAM	23	12	238 MHz	2 cc	1 cc
LLR	16-QAM	41	26	165 MHz	4 cc	1 cc
LLR	64-QAM	106	40	155 MHz	5 cc	1 cc
Symbol exp.	4-QAM	3	2	100 MHz	1 cc	1 cc
Symbol exp.	16-QAM	8	2	100 MHz	2 cc	1 cc
Symbol exp.	64-QAM	27	2	138 MHz	3 cc	1 cc
SIC	-	48	16	135 MHz	2 cc	1 cc

Table 19. The 4×4 SIC FPGA implementation results.

Block	Modulation	Slices	DSPs	Clock	Latency	Throughput
LMMSE	-	8509	43	139 MHz	2074 cc	982 cc
LLR	4-QAM	72	40	180 MHz	2 cc	1 cc
LLR	16-QAM	112	66	148 MHz	4 cc	1 cc
LLR	64-QAM	243	96	155 MHz	5 cc	1 cc
Symbol exp.	4-QAM	11	4	704 MHz	2 cc	1 cc
Symbol exp.	16-QAM	29	4	347 MHz	2 cc	1 cc
Symbol exp.	64-QAM	53	20	138 MHz	3 cc	1 cc
SIC	-	165	43	149 MHz	3 cc	1 cc

Table 20. The 2×2 SIC ASIC implementation results.

Block	Modulation	Gates	Power	Clock	Latency	Throughput
LMMSE	-	48 k	40 mW	100 MHz	60 cc	40 cc
LLR	4-QAM	12.4 k	30 mW	100 MHz	6 cc	3 cc
LLR	16-QAM	18.6 k	33 mW	100 MHz	11 cc	3 cc
LLR	64-QAM	30.3 k	45 mW	100 MHz	9 cc	3 cc
Symbol exp.	4-QAM	488	0.58 mW	100 MHz	1 cc	2 cc
Symbol exp.	16-QAM	1335	1.2 mW	100 MHz	2 cc	2 cc
Symbol exp.	64-QAM	3521	3.2 mW	100 MHz	2 cc	2 cc
SIC	-	17.5 k	22.3 mW	100 MHz	5 cc	3 cc

Table 21. The 4×4 SIC ASIC implementation results.

Block	Modulation	Gates	Power	Clock	Latency	Throughput
LMMSE	-	415 k	522 mW	134 MHz	1218 cc	504 cc
LLR	4-QAM	35.9 k	82.6 mW	100 MHz	6 cc	3 cc
LLR	16-QAM	45.8 k	91 mW	100 MHz	12 cc	3 cc
LLR	64-QAM	72.6 k	114 mW	100 MHz	7 cc	3 cc
Symbol exp.	4-QAM	664	0.56 mW	100 MHz	1 cc	1 cc
Symbol exp.	16-QAM	2346	1.2 mW	100 MHz	1 cc	1 cc
Symbol exp.	64-QAM	3146	2.2 mW	100 MHz	1 cc	1 cc
SIC	-	59 k	72 mW	100 MHz	5 cc	3 cc

4.5.4 Latency and receiver comparison

The processing latency of a receiver can be expressed as

$$D_{\text{rec}} = D_{\text{det}} + (D_{\text{LLR}} + D_{\text{dec}})N_{\text{iter}}, \tag{40}$$

where D_{det} is the latency of the detector, D_{LLR} is the latency of LLR calculation, D_{dec} is the latency of the decoder and N_{iter} is the number of iterations. LLR calculation and decoding can be performed simultaneously and in a pipelined manner with detection and their latency does not have to be included in the throughput latency. In an iterative

receiver, the throughput latency is determined by the minimum of D_{det} and $D_{\text{LLR}} + D_{\text{dec}}$. The detection rate of a receiver can be calculated as

$$\frac{QN}{D_{\text{rec}}}, \tag{41}$$

where Q is the number of bits per symbol and N is the number of transmit antennas.

The timing of the K-best receiver is shown in Figure 32. The detector and the LLR calculation are pipelined and have the same throughput period. The iterative LLR calculation can begin after the code block has been decoded. It can be performed simultaneously with the detection of the next code block. A code block size of 6,144 bits was assumed in the latency calculations.

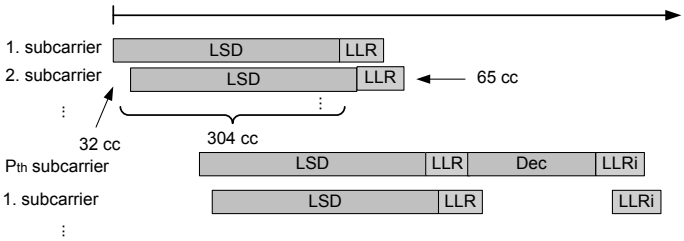

Fig. 32. The timing and latencies in the K-best receiver with 4×4 16-QAM.

The timing of the SIC receiver is illustrated in Figure 33, where the block latencies are presented in clock cycles. The throughput period is shown as the time after processing of the next subcarrier can begin. The weight matrices are calculated when the channel realization changes, i.e. once in the channel coherence time. It is assumed that not all the weight matrices have to be included in the decision on the layer to be detected and that the layer order will remain the same for several channel realizations. The latency of the LMMSE receiver does not depend on the modulation. The latency of turbo decoding is included in the total latency estimate and it is calculated from the results given in [208], where the decoding rate is 1.28 Gb/s. The turbo decoder limits pipelining in the SIC receiver in a way that all the subcarriers have to be decoded before moving to the symbol expectation calculation. The LLR1 block includes detection and LLR calculation and it can start to process the next OFDM symbol while the second layer in the previous symbol is being calculated.

A summary of the implementation results on FPGA is presented in Table 22 for a 2×2 antenna system and in Table 23 for a 4×4 system. The detection rate of

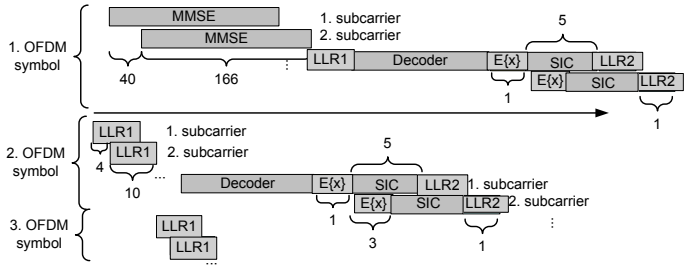

Fig. 33. The timing and latencies in the SIC receiver with 4×4 16-QAM ([62], published by permission of IEEE).

each detector and the required rate for an LTE system are also presented. In the LTE specifications, a 0.5 ms slot has been allocated for 7 or 6 (depending on the length of the cyclic prefix length) OFDM symbols [189]. In a 20 MHz bandwidth, each OFDM symbol contains 1,200 subcarriers. A part of the subcarriers is reserved for pilot symbols that do not have to be detected. In a 2×2 system, roughly 10 percent of the subcarriers in a slot are pilot symbols and in a 4×4 system, more than 16 percent of the subcarriers contain pilot symbols. The required detection rates are then calculated from the data subcarriers. Any other control signal or other overhead is not included in the required rates. The FPGA results were generated to take full advantage of the platform and the clock frequencies and detection rates are as high as possible with the given platform and algorithm. The K-best detection rate is restricted by the sorting in the algorithm. The LMMSE and SIC receivers have a higher detection rate than necessary. Several K-best detectors could be used in parallel to achieve the required detection rate.

Table 22. The 2×2 receiver FPGA complexity and throughput.

	Modulation	Slices	DSPs	Clock	Det. rate	Req. rate
LMMSE	4-QAM	713	23	126 MHz	252 Mbps	60 Mbps
SIC	4-QAM	772	43	126 MHz	210 Mbps	60 Mbps
16-best	4-QAM	1875	24	206 MHz	51.5 Mbps	60 Mbps
LMMSE	16-QAM	722	30	126 MHz	504 Mbps	121 Mbps
SIC	16-QAM	795	65	126 MHz	361 Mbps	121 Mbps
8-best	16-QAM	2550	18	189 MHz	47.3 Mbps	121 Mbps
8-best iter.	16-QAM	2762	18	189 MHz	45.5 Mbps	121 Mbps
LMMSE	64-QAM	755	37	126 MHz	756 Mbps	182 Mbps
SIC	64-QAM	879	79	126 MHz	476 Mbps	182 Mbps
8-best	64-QAM	3243	28	180 MHz	67.5 Mbps	182 Mbps
16-best	64-QAM	4606	28	194 MHz	36.4 Mbps	182 Mbps
Available		8160	288			

Table 23. The 4×4 receiver FPGA complexity and throughput.

	Modulation	Slices	DSPs	Clock	Det. rate	Req. rate
LMMSE	4-QAM	8566	79	139 MHz	612 Mbps	115 Mbps
SIC	4-QAM	8758	130	139 MHz	406 Mbps	115 Mbps
8-best	4-QAM	4889	52	192 MHz	96 Mbps	115 Mbps
LMMSE	16-QAM	8589	92	139 MHz	1.2 Gbps	230 Mbps
SIC	16-QAM	8815	156	139 MHz	615 Mbps	230 Mbps
8-best	16-QAM	6073	29	183 MHz	91.5 Mbps	230 Mbps
8-best iter.	16-QAM	6516	29	183 MHz	85.4 Mbps	230 Mbps
16-best	16-QAM	7863	29	129 MHz	32.3 Mbps	230 Mbps
LMMSE	64-QAM	8655	107	138 MHz	1.6 Gbps	345 Mbps
SIC	64-QAM	5970	202	138 MHz	721 Mbps	345 Mbps
8-best	64-QAM	8108	76	180 MHz	135 Mbps	345 Mbps
8-best iter.	64-QAM	8782	76	157 MHz	107.8 Mbps	345 Mbps
16-best	64-QAM	12317	74	211 MHz	79 Mbps	345 Mbps
Available		8160	288			

The ASIC implementation results are summarized in Table 24 for the 2×2 antenna system and in Table 25 for the 4×4 case. The LMMSE and SIC receiver were designed to have a 100 MHz clock frequency. They achieve the required detection rates in most cases. Based on the synthesis results, the SIC receiver could be easily clocked with a higher frequency in order to achieve the required rates. The K-best detector has a 280 MHz clock frequency, but it achieves the required rates only with the lower modulation orders. In the other cases, the number of tree search and LLR blocks would have to be doubled to achieve the required rates. The (P) in the table denotes the parallel K-best detector presented in Section 4.3.1. The iterative K-best receivers include two LLR calculation blocks. One block calculates the LLRs on the first iteration and the other block uses the feedback from the decoder. Decoding latency of two code words is included in detection rate results of the iterative K-best. The SIC receivers include the decoding latency of one code block in the detection rate results. The complexities of the different receivers do not differ greatly, but the power consumption of the K-best detector can be higher due to the higher clock frequency.

Table 24. The 2×2 receiver ASIC complexity and throughput.

	Modulation	Gates	Power	Clock	Det. rate	Req. rate
LMMSE	4-QAM	57.2 k	61.3 mW	100 MHz	66.7 Mbps	60 Mbps
SIC	4-QAM	78.3 k	92.6 mW	100 MHz	63.3 Mbps	60 Mbps
16-best	4-QAM	93.6 k	254 mW	280 MHz	70 Mbps	60 Mbps
LMMSE	16-QAM	60.2 k	64.3 mW	100 MHz	133 Mbps	121 Mbps
SIC	16-QAM	85.4 k	96.7 mW	100 MHz	120.7 Mbps	121 Mbps
8-best	16-QAM	105 k	238 mW	280 MHz	70 Mbps	121 Mbps
8-best iter.	16-QAM	112 k	273 mW	280 MHz	68.1 Mbps	121 Mbps
8-best (P)	16-QAM	116 k	287 mW	280 MHz	140 Mbps	121 Mbps
LMMSE	64-QAM	65.9 k	72.5 mW	100 MHz	200 Mbps	182 Mbps
SIC	64-QAM	99.3 k	110.6 mW	100 MHz	172.9 Mbps	182 Mbps
8-best (P)	64-QAM	137.5 k	326 mW	280 MHz	105 Mbps	182 Mbps
16-best (P)	64-QAM	161 k	404 mW	280 MHz	52.5 Mbps	182 Mbps

Table 25. The 4×4 receiver ASIC complexity and throughput

	Modulation	Gates	Power	Clock	Det. rate	Req. rate
LMMSE	4-QAM	444.5 k	587 mW	100 MHz	133 Mbps	115 Mbps
SIC	4-QAM	511 k	662 mW	100 MHz	120.7 Mbps	115 Mbps
8-best	4-QAM	367.3 k	604 mW	280 MHz	140 Mbps	115 Mbps
LMMSE	16-QAM	451 k	598 mW	100 MHz	266.7 Mbps	230 Mbps
SIC	16-QAM	522 k	686 mW	100 MHz	220.7 Mbps	230 Mbps
8-best	16-QAM	397 k	661 mW	280 MHz	140 Mbps	230 Mbps
8-best iter.	16-QAM	400.3 k	684 mW	280 MHz	126 Mbps	230 Mbps
LMMSE	64-QAM	459 k	607 mW	100 MHz	400 Mbps	345 Mbps
SIC	64-QAM	550 k	710 mW	100 MHz	304.7 Mbps	345 Mbps
8-best (P)	64-QAM	448 k	877 mW	280 MHz	210 Mbps	345 Mbps
16-best (P)	64-QAM	518.4 k	1052 mW	280 MHz	105 Mbps	345 Mbps

The performance, complexity and power consumption of the LMMSE, SIC and K-best are further illustrated in Figures 34 and 35. The goodput was defined to be the lesser of the detection rate and transmission throughput. Even though the information

transmission rate of the K-best detector is higher than that of the SIC or LMMSE, the hardware detection rate of a single detector is lower. The number of detectors was increased to achieve the required rates, but this resulted also in an increase in the complexity and power consumption. The results in Figures 34 and 35 are very similar. In some cases, the SIC detector achieves a higher goodput with a lower amount of power consumption than the K-best detector. The complexity, however, can be very close to that of the 8-best detector. This can also be calculated from the theoretical complexity in Table 4. The power consumption results may differ from the theoretical results due to the different clock frequencies. The LMMSE has the lowest power consumption, but it may not achieve any goodput in difficult channel conditions. It can be seen that the 16-best detector has a very high complexity and power consumption, while the goodput is at the same level as with the 8-best. The 8-best provides a fair amount of goodput in all scenarios.

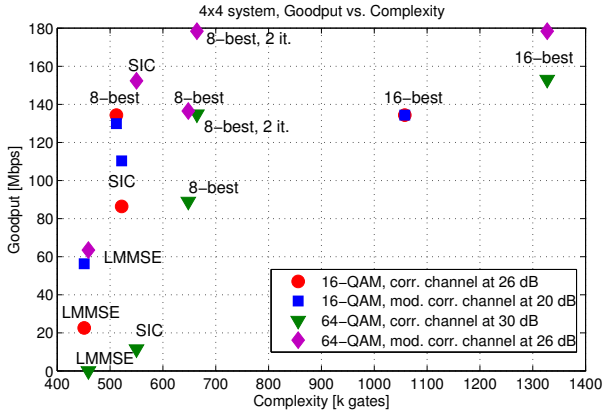

Fig. 34. Complexity-performance trade-off in a 4×4 antenna system.

4.5.5 SSFE and K-best comparison

The complexity and performance of two tree search algorithms are compared. The performance of the algorithms was discussed in Section 4.4.5. The complexity results for the SSFE and K-best detectors are presented in Table 26 in the 16-QAM case and in Table 27 in the 64-QAM case. The SSFE list size is 12 and the node spanning vector is [3,2,2,1,1,1,1,1] as in the simulation results. The clock frequency of the detectors

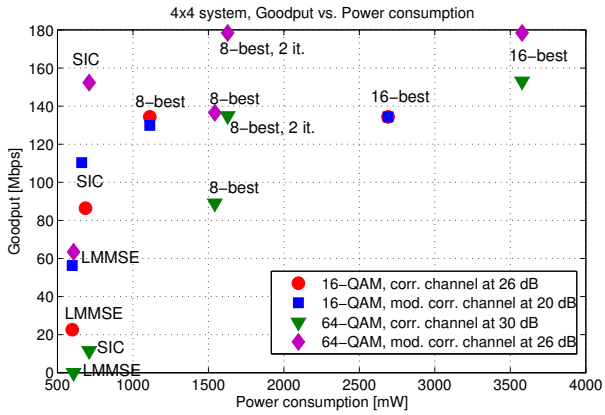

Fig. 35. Power consumption-performance trade-off in a 4×4 antenna system.

was 280 MHz except for the 64-QAM SSFE where only a 269 MHz clock frequency was achieved. In the receiver with two global iterations, the tree search is performed only once and the complexity is the same as with one iteration. However, the LLR calculation is different in the two cases as the feedback from the decoder is used in the iterative detector. Decoding reduces the detection rate in the iterative receiver. The 8-best detector has a lower complexity and power consumption than the SSFE in the 16-QAM case, but the detection rate is also lower. The power consumption is also lower in the 64-QAM case, but the detection rate of the SSFE is higher. The higher list size of the SSFE increases its complexity and power consumption. The SSFE-SIC from Section 4.3.3 was not implemented as it required a high list size to perform well. Therefore, the complexity would be too high compared to the achievable performance gain.

Table 26. Implementation results with 4×4 16-QAM.

Receiver	Gates		Power		Detection rate
	Tree search	LLR	Tree search	LLR	
SSFE	135.2 k	19 k	488.9 mW	79 mW	186 Mbps
SSFE, 2 it.	135.2 k	34.6 k	488.9 mW	158 mW	163 Mbps
8-best	97 k	17.3 k	341.5 mW	68.3 mW	140 Mbps
8-best, 2 it.	97 k	33.1 k	341.5 mW	140.5 mW	126 Mbps
16-best	148.4 k	20.2 k	499.6 mW	79.2 mW	70 Mbps

Table 27. Implementation results with 4×4 64-QAM.

Receiver	Gates		Power		Detection rate
	Tree search	LLR	Tree search	LLR	
SSFE	177.4 k	25.7 k	568.6 mW	110.5 mW	269 Mbps
SSFE, 2 it.	177.4 k	50.4 k	568.6 mW	236.7 mW	222 Mbps
8-best	183.7 k	21.5 k	551.4 mW	87 mW	210 Mbps
8-best, 2 it.	183.7 k	45.2 k	551.4 mW	197.9 mW	180 Mbps
16-best	217.2 k	24.5 k	717.3 mW	96.6 mW	105 Mbps

The complexity-performance trade-off is illustrated in Figure 36. The goodput i.e. the minimum of the transmission throughput and hardware detection rate of information bits in a 20 MHz bandwidth with a 1/2 code rate, is compared to the hardware complexity. The K-best with list size of 16 has a high complexity and low goodput. The goodput of the SSFE with two global iterations is close to that of the 8-best with one iteration with 16-QAM, but has a higher complexity. With 64-QAM, SSFE with two iterations achieves the highest goodput. Extra iterations do not bring any benefit with the K-best tree search as the detection rate is low. Even though the SSFE algorithm does not include sorting, the slicing operation induces extra complexity compared to the K-best algorithm and the difference between the two tree search algorithms remains small.

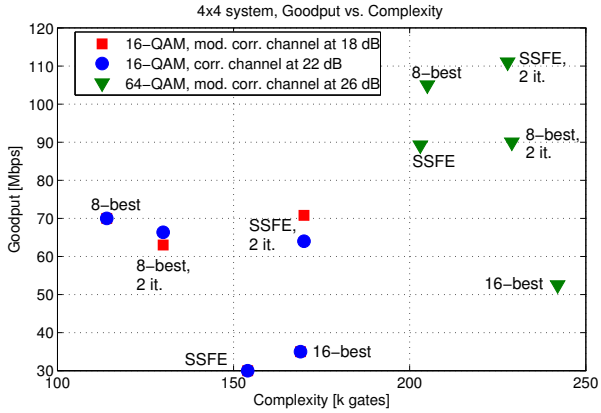

Fig. 36. Complexity-performance trade-off in a 4×4 antenna system.

4.5.6 Receiver adaptation

Architecture

The architecture of the QRD and MMSE calculation for an $N \times N$ MIMO system is presented in Figure 37. The QRD of the matrix is calculated with an algorithm which produces a unitary matrix Q. The input matrix is either the extended channel matrix $\underline{\underline{\mathbf{H}}}$ or the matrix used in the capacity and SINR calculations. The same QRD architecture can be used for both matrices. For example, the Gram-Schmidt process [209] presented in Section 4.2 without column reordering can be used for the QRD. Part of the multipliers can be turned off when calculating capacity because the input matrix is smaller than the extended channel matrix. Another option is to extend the capacity/SINR matrix with zeros and then the QRD architecture can be used in exactly the same way as with the extended channel matrix. The capacity is obtained by multiplying the diagonal elements of $\mathbf{R}$ and taking the logarithm from the product. The SINR for stream n is found by calculating the inverse of the diagonal element (n,n) of matrix $\mathbf{W}$.

The decision on the modulation and coding scheme can be obtained by summing the SINR or capacity of the subcarriers in an OFDM symbol and using a lookup table to select the modulation, code rate and transmission rank based on the sum. The calculation of QRD and capacity can be time interleaved as they are not performed in each frame but in the channel coherence time. If precoding is used, multiplying the channel matrix

with different precoding matrices is added to the left side of the architecture. A separate block can be added to calculate the rank 1 and 2 capacities as matrix inversion is not necessary.

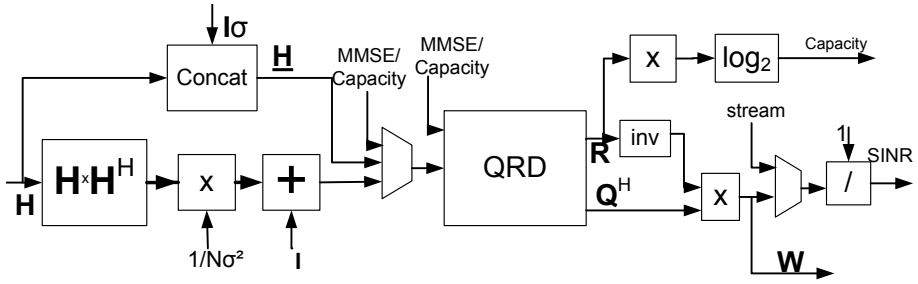

Fig. 37. Architecture of the capacity and MMSE/QRD calculation ([63], published by permission of IEEE).

Implementation results

The LMMSE, SIC and K-best LSD receivers were designed to operate with an adaptive modulation scheme in a 2×2 and a 4×4 antenna system. Therefore, the receivers can be used with QPSK, 16-QAM and 64-QAM. The decoder is not included in the complexity results, but a high throughput turbo decoder [208, 210] can be used to achieve the LTE decoding rate requirement.

The complexities in gate equivalents of the preprocessing, detection and LLR calculation are presented in Table 28 for the 2×2 system and Table 29 for the 4×4 system. The clock frequency was 280 MHz with the K-best LSD and 100 MHz with the other receivers and preprocessing. In the 2×2 case, the MMSE was calculated with the direct matrix inversion and the QRD with the Gram-Schmidt algorithm. The QRD was the most complex block. The latency of the block is the time after which processing of the next input can start. The preprocessing latency can be higher than the detection latency as it has to be performed when the channel realization changes. In the 4×4 system, the QRD is one of the most complex blocks. An 8×16 real valued extended channel matrix is used as an input to the QRD. As the direct matrix inversion for MMSE weight matrix calculation would be more complex in the 4×4 system, the QRD of the extended channel matrix is used to calculate the weight matrix as presented in (19). The

word lengths of the different receivers are mostly 16 bits. In the QRD, some larger inner word lengths were used and if the QRD is used for capacity calculation, the inputs are scaled as the capacity values are larger than the channel values.

Table 28. The 2×2 implementation results for adaptive receiver.

Receiver Block	Complexity (Gates)	Power (mW)	Latency ns
QRD (Gram-Schmidt)	66.6 k	35.1	400
MMSE (direct matrix inversion)	48 k	40	400
Detection and LLR	17.1 k	12.8	10
SIC	19.6 k	24.5	40
4-best LSD	31.7 k	120.6	114
8-best LSD	51.3 k	198	114
LLR for 4-best	12.6 k	50	114
LLR for 8-best	14.4 k	57.4	114
LLR it. for 8-best	18.7 k	79.6	114

Table 29. The 4×4 implementation results for adaptive receiver.

Receiver Block	**Complexity** (Gates)	**Power** (mW)	**Latency** ns
QRD (Gram-Schmidt)	179.8 k	116	4480
$\mathbf{R}^{-1}$ (for MMSE)	43.5 k	31.9	3420
Matrix mult. (for MMSE)	29 k	31.4	3200
Detection and LLR	31 k	33.7	50
SIC	86.3 k	88.7	40
4-best LSD	78.3 k	322.8	114
8-best LSD	126.6 k	496	114
LLR for 4-best	18.2 k	74.5	114
LLR it. for 4-best	41.4 k	216.9	114
LLR for 8-best	21 k	86.2	114

The total complexity and power consumption of the receivers are presented in Tables 30 and 31. The K-best LSD has the highest complexity. In the 2×2 system, the complexity of the SIC receiver is much lower even though the performance is close to that of the K-best LSD.

Table 30. Complexity and decoding rate of 2×2 adaptive receivers.

Receiver	Complexity (Gates)	Power consumption (mW)	Max. det. rate (Mbps)
LMMSE	59.5 k	52.4	600
SIC	84.7 k	77.3	134
4-best	130 k	229	105
8-best	151.7 k	314	105
8-best, 2 it.	156 k	368	97

The difference in complexity between the receivers is smaller in the 4×4 case than in the 2×2 case. Calculating the MMSE weight matrix $\mathbf{W}$ takes almost 90 percent of the gate equivalents in the LMMSE receiver in the 4×4 case. The 2×2 system allowed some simplifications in the implementation and cannot be straightforwardly scaled to all other antenna configurations. The 4×4 implementation could be also scaled to larger antenna configurations.

Table 31. Complexity and decoding rate of 4×4 adaptive receivers.

Receiver	Complexity (Gates)	Power consumption (mW)	Max. det. rate (Mbps)
LMMSE	283.3 k	213	240
SIC	369.6 k	302	202
4-best	305 k	538	210
4-best, 2 it.	329 k	681	180
8-best	356.5 k	723	210

If precoding is used, the complexity of the receiver is increased. The capacity has to be calculated for the sixteen possible precoding matrices in LTE with the different precoding matrix ranks. For rank 4 transmission, the capacity is the same for all

precoding matrices and it has to be calculated only once. The QRD can be used to calculate the determinant, as shown in Figure 37. The matrix multiplications and the low rank determinant calculations add still another 82 k gates to the complexity, as shown in Table 32. Without precoding, the capacity calculations are simpler and most of the complexity comes from the $\mathbf{H}^{\mathrm{H}}\mathbf{H}$ matrix multiplication.

Table 32. Complexity of precoding in a 4×4 system ([63], published by permission of IEEE).

Block	Complexity (Gates)	Power (mW)
Capacity with precoding	81.9 k	39.2
Capacity without precoding	32 k	36

4.6 Discussion

The theoretical complexities of the algorithms were presented. The complexity of the K-best algorithm is close to that of the SIC algorithm with low order modulations, but the difference is greater with higher modulations. The implementation results in Section 4.5 support the theoretical results in Table 4: the receivers have similar complexities with low order modulations, but the complexity of the K-best LSD increases with the modulation order. The LMMSE calculation was implemented as a direct matrix inversion in the 2×2 case, which made the SIC less complex even with low order modulations.

Comparison of both performance and implementation to literature can be difficult as the used channel models, methods and the implementation technologies may be different. Many of the implementations in the literature consider an uncoded system or an uncorrelated channel, where also simple receivers perform well, which can lead to different parameters in the implementation. Also, the word length requirements may vary with different system setups. The parameters used may have even a higher impact on the preprocessing, i.e. the LMMSE filter or the QRD. Depth-first sphere detector implementations in the literature usually report an SNR dependent throughput, which makes the implementation comparison more challenging. The use of a HLS tool in this work also results in an unfavorable comparison to hand-coded results.

The Givens rotation based QRD in [120] uses smaller word lengths than the QRD implementation in this work. The complexity is roughly 100 k gates smaller, but the power consumption is higher by 100 mW. The latency of the QRD is, however, much smaller than that in this work. An MMSE receiver was implemented in [116]. The complexity and power consumption are much higher than those in this work, however, the detection rate is also higher. Nevertheless, a lower detection rate was aimed for in this work.

The hard-output l^2-norm K-best detectors in [211] have a lower complexity, but were implemented with different list sizes and CMOS technology from our work. Other norms were also used in [211] for the Euclidean distance calculation to avoid the squaring operation in the l^2-norm, yet since they were not used in this work as they also have an impact on performance, their implementation is not comparable. The complexity of the receiver increases by roughly 30 percent both in [211] and this work when the list size is doubled. However, the detection rate decreases almost five times in [211], whereas it is only halved in our work. An implementation of a radius adaptive K-best detector was presented in [128]. The complexities of the 64-QAM K-best detectors are similar to those in this work, yet the power consumption is much lower. This can also be due to the different implementation technology. The hard-output K-best detector with on demand node expansion was implemented in [129]. A different implementation technology was used, but the gate count and power consumption were smaller than those in this work. The soft output K-best implementation in [103] with a list size of 5 in a 4×4 16-QAM system has almost a three times lower throughput and half the complexity of our implementation with a list size of 8. A soft output K-best detector is presented in [124]. It achieves a 50 Mb/s throughput with 4×4 64-QAM, list size of 256 and a silicon area of 20 mm^2. In conclusion, numerous existing detection implementations can be found, but a meaningful quantitative comparison in terms of performance and complexity is difficult. Therefore, the performance and complexity of several detection algorithms was compared in this work.

The performance-complexity trade-off of the ASIC implementations in a 2×2 16-QAM in a correlated channel is summarized in Table 33 and in the 4×4 16-QAM case in Table 34. The detection rates of the receivers are almost the same and enough to reach 121 Mbps in the 2×2 case and 230 Mbps in the 4×4 case. Even though the detection rate of the LMMSE receiver is high, the performance degradation in terms of reliable transmission throughput is considerable, in particular at the cell edge, where the available SNR is often low. The term goodput was defined to be the minimum of the

hardware detection rate times the 1/2 code rate and the transmission rate of information bits over the 20 MHz bandwidth times (1−FER).

The LMMSE receiver would require almost 10 dB more transmit power in order to achieve the goodput of the K-best LSD, but the power consumption is much higher with the K-best LSD. The SIC receiver does not achieve the goodput of the K-best LSD, but has a much lower complexity. In the 4×4 antenna case, the SIC and LMMSE receivers do not give much goodput at lower SNRs, yet all the receivers have a high goodput when the SNR is high enough. If the channel is less correlated, the receivers have a more similar performance and less transmit power is needed to achieve a high goodput. The SIC receiver produces the most bits per gate equivalent in the 2×2 antenna system, but in the 4×4 system, the K-best LSD is the most efficient. A part of the performance degradation of the SIC receiver in the 4×4 antenna system is due to the encoding of the streams, which leads to interference cancellation being performed between two layer pairs and the two layer pairs being separated only by the LMMSE equalizer. The SIC receiver would still provide a higher goodput than the LMMSE receiver with a lower power consumption than the K-best LSD, thus, offering a compromise between performance and complexity.

Table 33. The performance-complexity trade-off with 2×2 16-QAM.

Receiver	Complexity (Gates)	Power mW	Goodput at 16 dB	Goodput at 20 dB
LMMSE	60 k	64	0.3 Mb/s	15.7 Mb/s
SIC	85 k	97	6.2 Mb/s	49.4 Mb/s
8-best	170 k	274	17.4 Mb/s	67.3 Mb/s
8-best, 2 iter.	173 k	458	32.4 Mb/s	69.8 Mb/s

Table 34. The performance-complexity trade-off with 4×4 16-QAM.

Receiver	Complexity (Gates)	Power mW	Goodput at 24 dB	Goodput at 28 dB
LMMSE	451 k	598	0.1 Mb/s	84.4 Mb/s
SIC	522 k	686	20.6 Mb/s	133.7 Mb/s
8-best	545 k	1112	113.4 Mb/s	140 Mb/s
8-best, 2 iter.	576 k	1257	128 Mb/s	140 Mb/s

As a final illustration of the performance-complexity trade-off, the required transmit power to satisfy the rate and quality requirements is considered in a simple example case. As the LMMSE and SIC receivers reach their maximum throughput at higher SNRs than the K-best receiver, the transmit power needs to be higher to obtain the highest data rates. The following example case illustrates the distance at which the maximum data rates can be achieved with the different receivers. The power efficiency of the transmitter in transmit power/transmission rate in a 4×4 antenna system with a 20 MHz bandwidth is presented in Figure 38. The needed transmit power was obtained from $L_F + N_R + \text{SNR} + \text{FM}$, where L_F is the free space path loss $20\log(4\pi d/\lambda)$, N_R is the receiver noise floor (kTB + receiver noise figure of 6 dB) and FM is a 30 dB fade margin (λ is the wavelength, d is the distance from the base station, k is Boltzmann's constant, T is the temperature [K] and B is the bandwidth). The SNR is the signal strength at the receiver required to achieve the maximum goodput. A simple path loss model without shadowing or reflections was chosen for simplicity. The required transmit power of the LMMSE receiver is at least twice of that of the K-best LSD. The transmit energy per bit grows with the modulation order and is the same with 64-QAM K-best LSD and 16-QAM LMMSE. The K-best LSD can receive data reliably from a higher distance than the SIC or LMMSE receiver with a fixed transmit power. With 4×4 64-QAM, the LMMSE receiver can receive data at only very short distances with a reasonable transmit power. Therefore, a more complex receiver is needed to receive data from also larger distances.

The previous performance-complexity trade-off results assumed that there is no channel state information at the transmitter. With full or partial transmitter channel state information, low mobility appropriate feedback schemes combined with transmitter precoding could change the conclusions. Therefore, the impact of adaptive modulation

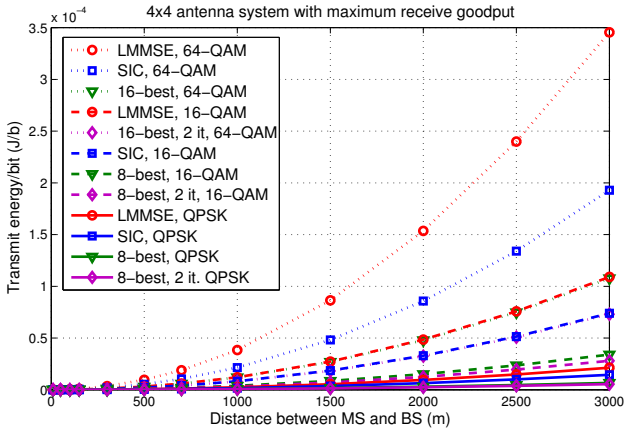

Fig. 38. The transmitter energy consumption per reliably transmitted bit versus the propagation distance ([62], published by permission of IEEE).

and coding with transmission rank adaptation on the performance of different receiver algorithms was studied in Section 4.5.6. The complexities and goodput of the LMMSE, SIC and K-best receivers in a 2×2 antenna system with AMC are summarized in Table 35. The performance differences are smaller with AMC than with fixed modulation and coding schemes. In the low SNRs, the performances of the receivers are similar, but when the transmission rank is increased at the high SNRs, the more complex receivers give a higher goodput. The situation is similar in the 4×4 antenna system, but the differences at high SNRs are larger. A reconfigurable architecture could be used, where a low complexity receiver in the low SNRs and a more complex receiver in the high SNRs would provide the highest goodput with the least amount of power.

Table 35. The 2×2 performance-complexity trade-off.

Receiver	Gates	Goodput at 4 dB	Goodput at 28 dB
LMMSE	60 k	21.9 Mb/s	89 Mb/s
SIC	121 k	30.1 Mb/s	103.2 Mb/s
4-best	193 k	26.5 Mb/s	100.6 Mb/s
8-best	237 k	29.3 Mb/s	113.6 Mb/s
8-best, 2 it.	245 k	30.7 Mb/s	123.4 Mb/s

5 Channel estimation in MIMO-OFDM systems

In this chapter, performance of the LS, MMSE and SAGE channel estimation algorithms is studied using the LTE pilot symbol structure as a benchmark. The fast fading or high mobility scenario with insufficient pilot symbol density and the high pilot overheads from the MIMO pilot symbols are the two main issues considered. The SAGE channel estimator is used in the iterative receiver to improve the performance when the pilot symbol density is too low, i.e. in high velocity cases. MMSE filtering is also used in between pilot symbols to improve the channel estimates and the performance is compared to that of the SAGE estimator. The throughput can be increased by replacing some of the pilot symbols with data symbols and using the SAGE algorithm to compensate for the performance loss caused by the decreased pilot density. The theoretical complexity of the channel estimation algorithms is presented and some complexity-performance trade-off aspects of the SAGE algorithm are considered. The architecture and implementation results in gate counts and power consumption for the pilot symbol based LS, MMSE and the DD SAGE channel estimators are presented for the 2×2 and 4×4 antenna systems. For a more energy efficient solution, a longer latency for the channel estimator is considered. The impact of generating a timely channel estimate for the detector on the performance and complexity is then discussed.

The main contributions of this chapter are the implementation of data aided and decision directed channel estimation algorithms and evaluating the applicability of the channel estimation algorithms for mobile MIMO-OFDM systems with different pilot symbol densities. Although different channel estimation algorithms have been proposed, only few implementations of channel estimation algorithms can be found in the literature. Furthermore, the latency of decision directed channel estimation has not been previously considered. Thus, these are the main themes of this chapter.

The channel estimation algorithms are introduced in Section 5.1. The performances of the algorithms with different channel models are compared in Section 5.2 and some complexity reducing alterations and latency issues are discussed in Section 5.3. The implementation results are presented in Section 5.4 and Section 5.5 includes discussion on the results. The performances of the LS and SAGE algorithms were compared in [67], where the latency of the SAGE estimator was also discussed. The implementation results and the simulation results presented in Section 5.2 have not been previously

published.

5.1 Channel estimation algorithms

The system model was introduced in Section 3.1 and the signal model for channel estimation in Section 3.3. The receiver structure is presented in Figure 39. The LS channel estimator is used in calculating the channel estimates from pilot symbols. The received signal vector is transformed into frequency domain before the LS channel estimation. The LS channel estimate can be filtered with an MMSE filter. The channel impulse response result from the LS or MMSE estimator has to be transformed into frequency domain for the detector with the second fast Fourier transform (FFT). The DD SAGE channel estimator can be used in addition to the LS estimator. The pilot based LS estimator provides initial channel estimates for the SAGE algorithm. The soft symbols are calculated from the decoder outputs as in (31) in Chapter 4 and are transformed into time domain for the SAGE channel estimator. The SAGE channel estimator also takes the time domain received signal as input. The hard outputs from the decoder are not considered for channel estimation as the soft information better represents the reliability of the decision.

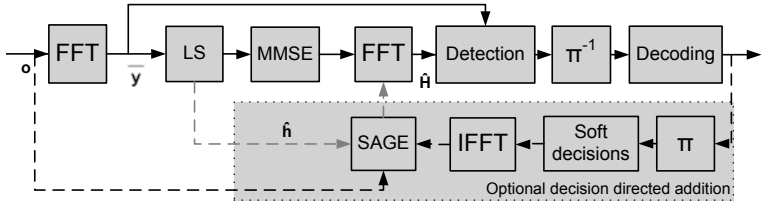

Fig. 39. The receiver structure.

5.1.1 LS channel estimation

The LS estimate of the channel can be calculated as

$$\hat{\mathbf{h}}_{m_R}^{\mathrm{LS}}(n) = (\mathbf{F}^{\mathrm{H}}\mathbf{X}^{\mathrm{H}}(n)\mathbf{X}(n)\mathbf{F})^{-1}\mathbf{F}^{\mathrm{H}}\mathbf{X}^{\mathrm{H}}(n)\overline{\mathbf{y}}_{m_R}(n), \tag{42}$$

where $\mathbf{X}$ contains the pilot symbols or if used in a DD mode, the symbol decisions. The calculation of the LS channel estimate from the pilot symbols is simple as the matrix

inversion can be calculated in advance and the only calculation to be performed in real time is multiplication with the received signal. When using the LS estimator in a DD mode, the $NL \times NL$ matrix inversion induces a high computational complexity.

5.1.2 MMSE channel estimation

In order to exploit the time domain correlation of the channel and to take into account the impact of the noise, the LS channel estimate can be filtered with an MMSE filter [74]

$$\hat{\mathbf{h}}^{\mathrm{MMSE}}_{m_R,m_T,l}(n) = \mathbf{W}^{\mathrm{H}}_{m_R,m_T,l}(n)\hat{\mathbf{h}}^{\mathrm{LS}}_{m_R,m_T,l}, \tag{43}$$

where the LS channel estimate vector for the lth tap from the m_Tth transmit antenna to the m_Rth receive antenna

$$\hat{\mathbf{h}}^{\mathrm{LS}}_{m_R,m_T,l} = [\hat{h}^{\mathrm{LS}}_{m_R,m_T,l}(n_1)...\hat{h}^{\mathrm{LS}}_{m_R,m_T,l}(n_{N_P})]^{\mathrm{T}} \in \mathbb{C}^{N_P \times 1} \tag{44}$$

contains the LS channel estimates from the duration of the filtering window. N_P is the number of OFDM symbols with pilot symbols in a filtering window and $m_T = 1,...,N$ and $m_R = 1,...,M$ are the transmit and receive antenna indices. The MMSE filtering vector $\mathbf{W}_{m_R,m_T,l}(n)$ is [156]

$$\mathbf{W}_{m_R,m_T,l}(n) = \Sigma^{-1}_{\hat{\mathbf{h}}^{\mathrm{LS}}_{m_R,m_T,l}} \Sigma^{\mathrm{H}}_{m_R,m_T,l}, \tag{45}$$

where the cross-covariance matrix between $h_{m_R,m_T,l(n)}$ and $\hat{\mathbf{h}}^{\mathrm{LS}}_{m_R,m_T,l}$ is

$$\Sigma_{m_R,m_T,l} = [\rho(n-n_1)...\rho(n-n_{N_P})]\Sigma_{\mathbf{h}_l} \tag{46}$$

and the auto-covariance matrix is

$$\Sigma_{\hat{\mathbf{h}}^{\mathrm{LS}}_{m_R,m_T,l}} = \begin{bmatrix} \rho(n_1-n_1) & \cdots & \rho(n_1-n_{N_P}) \\ \vdots & \ddots & \vdots \\ \rho(n_{N_P}-n_1) & \cdots & \rho(n_{N_P}-n_{N_P}) \end{bmatrix} \Sigma_{\mathbf{h}_{m_R,m_T,l}} + \Sigma_w. \tag{47}$$

The noise covariance matrix $\Sigma_w = \sigma^2\mathbf{I} \in \mathbb{R}^{N_P \times N_P}$, $\Sigma_{\mathbf{h}_{m_R,m_T,l}} = E(h^*_{m_R,m_T,l}h_{m_R,m_T,l})$ and $\rho(n-n')$ is the temporal correlation between the channel taps, which depends on the lag $n-n'$ between time indices n and n' [156]. In order to avoid the calculation of the spatial correlation $\Sigma_{\mathbf{h}_l}$, it can be left out from (46) and (47). This only has a minor impact on the performance, as presented in Section 5.2. It also enables the use of precalculated MMSE

filter coefficients, where the predetermined values for σ^2 and user velocity are used. The coefficients can be calculated for a set of σ^2 and velocity values and the coefficients closest to the estimated values can be used. Since $\rho(n-n)=1$ and Σ_w contains σ^2 on its diagonal, the precalculated coefficients can be obtained by substituting the known values in (45). The MMSE filter coefficients can be then precalculated as

$$\begin{bmatrix} 1+\sigma^2 & \cdots & \rho(n_1-n_{N_P}) \\ \vdots & \ddots & \vdots \\ \rho(n_{N_P}-n_1) & \cdots & 1+\sigma^2 \end{bmatrix}^{-1} \begin{bmatrix} \rho(n-n_1) \\ \vdots \\ \rho(n-n_{N_P}) \end{bmatrix}, \tag{48}$$

where the temporal correlation is distributed according to Jakes' model and can be written as

$$\rho(n-n') = J_0(2\pi f_d(n-n')T_B) \tag{49}$$

and J_0 denotes the zeroth-order Bessel function of the first kind, f_d is the Doppler frequency and T_B is the OFDM symbol duration.

5.1.3 SAGE channel estimation

The EM algorithms consist of an expectation and a maximization step. The "complete" data is estimated in the expectation step and the channel estimate is updated in the maximization step. The frequency domain SAGE algorithm provides an iterative solution of the decision directed LS estimate in (55). The time domain SAGE algorithm [212] can be used to avoid the matrix inversion required with non-constant envelope modulations in FD SAGE channel estimator. The time domain received signal $\mathbf{o}$ is viewed as the "incomplete" data and $\mathbf{z}$ as the "complete" data, which is iteratively updated along with the channel estimate $\hat{h}_{m_T,m_R,l}(n)$. The time domain SAGE algorithm calculates the channel estimates with iterations

$$\hat{\mathbf{z}}^{(i)}_{m_T,m_R,l} = \bar{\hat{\mathbf{z}}}^{(i)}_{m_T,m_R,l} + [\mathbf{o}_{m_R} - \sum_{m'_T=1}^{M_T} \sum_{l'=0}^{L-1} \bar{\hat{\mathbf{z}}}^{(i)}_{m'_T,m_R,l'}] \tag{50}$$

$$\hat{h}^{(i+1)}_{m_T,m_R,l}(n) = \frac{\bar{\mathbf{x}}^{\mathrm{H}}_{m_T,l} \hat{\mathbf{z}}^{(i)}_{m_T,m_R}(n)}{\bar{\mathbf{x}}^{\mathrm{H}}_{m_T,l} \bar{\mathbf{x}}_{m_T,l}} \tag{51}$$

$$\bar{\hat{\mathbf{z}}}^{(i+1)}_{m_T,m_R,l}(n) = \bar{\mathbf{x}}_{m_T,l} \hat{h}^{(i+1)}_{m_T,m_R,l} \tag{52}$$

$$\bar{\hat{\mathbf{z}}}^{(i+1)}_{m''_T,m_R,l''}(n) = \bar{\hat{\mathbf{z}}}^{(i)}_{m''_T,m_R,l''}. \tag{53}$$

The channel estimator is initialized with the channel estimate $\hat{h}^{(0)}_{m_T,m_R,l}$ from the previous OFDM symbol as

$$\bar{\hat{\mathbf{z}}}^{(0)}_{m_T,m_R,l}(n) = \bar{\mathbf{x}}_{m_T,l}\hat{h}^{(0)}_{m_T,m_R,l}. \tag{54}$$

5.2 Performance comparison

The simulation parameters are presented in Table 36 and the vehicular channel model parameters [213] in Table 1 in Section 3.4. Alternatively, a Winner channel model was used [195]. The Winner channel parameters were presented in Table 2. The detector used in the simulations is a K-best list sphere detector [88] with the list size of 8 in the 2×2 antenna system and 16 in the 4×4 antenna system. The user velocities of 50 km/h and 100 km/h were assumed, where the corresponding Doppler frequencies were 111 Hz and 222 Hz.

Mitigation of inter-carrier interference (ICI) caused by very high mobile velocities is out of the scope of this work. The remaining frequency offset after frequency synchronization may be modeled with increased noise at the receiver [214]. Furthermore, the algorithms considered in this thesis are not among the most suitable algorithms for very high velocities where the ICI would be the most dominant.

The throughput can be increased by using half of the LTE reference signals along with the decision directed channel estimation. The pilot symbols are then transmitted only in the first OFDM symbol in a slot and data is transmitted instead of pilot symbols in the other OFDM symbols which is denoted in the figures as 1 pilot. Channel estimation can be performed over several slots, but this degrades the performance in high velocity scenarios.

In the following simulation results, LS channel estimation is used on the OFDM symbols with pilot symbols and the SAGE algorithm is used on the OFDM symbols without reference signals. The performance of the SAGE algorithm with transmitted data as the feedback, i.e. genie aided SAGE algorithm, is also shown in the figures. With the genie aided mode, pilots are transmitted in one OFDM symbol per slot where the LS estimator is used in estimating the channel. The MMSE channel estimator is precalculated with the velocity of 70 km/h and the SNR of 26.5 dB in the 4×4 antenna system and 16.5 dB in the 2×2 antenna case as they were found to be suitable for most of the simulation cases. MMSE filtering is performed over one slot with the LTE pilot

structure and over two slots with pilots in only one OFDM symbol as the MMSE filter needs at least two channel estimates to perform well. The filtering window is shifted when a new channel estimate is available from the LS estimator in order to obtain the most current estimates. This also decreases the latency from the case where channel estimation is performed on the whole slot before detection. Increasing the size of the filtering window with LTE pilot structure does not improve the performance.

The performances of the LS, the precalculated MMSE and the SAGE algorithms are presented and compared in the following figures. First, the results with 2×2 antenna system with 16-QAM and 100 km/h user velocity are presented in Figure 40 followed by the 4×4 16-QAM results with a 50 km/h user velocity in Figures 41 and 42. Then, results for 4×4 MIMO with 16-QAM, different channel types and 100 km/h user velocity in Figure 43 are discussed. After that, the performance of the algorithms is illustrated in Figure 45 for 4×4 64-QAM and a 50 km/h user velocity, including comparisons of the MMSE estimator with known velocity and SNR and the precalculated MMSE filter with constant velocity and SNR. Spatial correlation is not used in the MMSE filter with the exception of the results with the known spatial correlation in Figure 44. The impact of estimated tap delays is presented in Figure 46 and the performances with the Winner channel model are shown in Figures 47 and 48. The performance with the LMMSE and K-best detectors combined with MMSE and SAGE channel estimators in an uncorrelated channel are compared in Figure 49. The typical urban channels are moderately correlated with base station (BS) azimuth spread of 5 degrees except for the channels in Figures 43 and 49.

Table 36. Simulation parameters.

Coding	Turbo coding with 1/2 code rate
Carrier frequency	2.4 GHz
Modulation scheme	16-QAM, 64-QAM
Number of subcarriers	512 (300 used), 5 MHz bandwidth
Symbol duration	71.4 μs

The performance of the channel estimation algorithms is presented in Figure 40 in a 2×2 antenna system. The communication system performance is usually characterized by frame error rate. The transmission throughput is defined to be equal to the nominal information transmission rate of information bits times $(1 - \text{FER})$. The throughput

increases when half of the LTE reference symbols are used along with the decision directed channel estimation. However, the MMSE estimator performs nearly as well as the SAGE estimator in the 2×2 antenna system. The pilot symbol density is not high enough for the LS estimator to perform well since the channel changes too rapidly between the OFDM symbols containing pilot symbols.

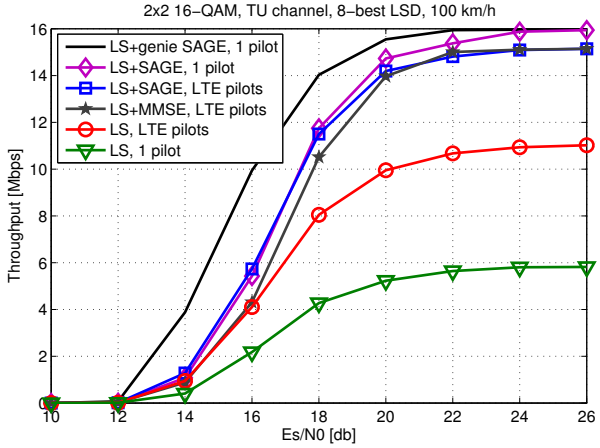

Fig. 40. 2×2 **16-QAM data transmission throughput vs. SNR with different pilot densities and 100 km/h user velocity.**

The same can be seen in Figure 41 with a 4×4 antenna system, where the decision directed channel estimation increases the throughput more than in the 2×2 antenna case already with the LTE pilot symbols. With pilot symbols in one OFDM symbol in a slot, denoted as 1 pilot, pilot symbols for all antennas are transmitted in the 1st OFDM symbol. The MMSE and SAGE estimators are able to compensate for the performance loss from the decreased pilot symbol density, unlike the LS estimator. The performance of the MMSE estimator is almost as good as with the SAGE estimator with the LTE pilot structure, but when the pilot density is decreased, the performance difference is larger.

The simulated mean square error of channel estimation is presented in Figure 42 in the same scenario as in Figure 41. The performance of the SAGE channel estimator is highly dependent on the quality of the data decisions. This can be seen in the MSE as saturation when the data decisions are reliable. The MSE of the LS or MMSE channel estimators does not depend on the data decisions.

The performance with a 100 km/h user velocity is shown in Figure 43 and the MSE

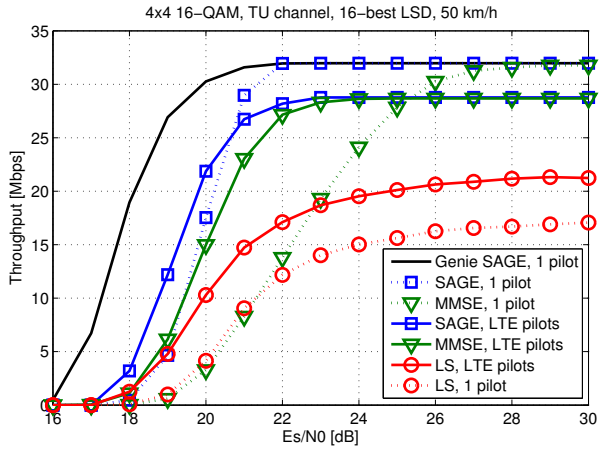

Fig. 41. 4×4 **16-QAM data transmission throughput vs. SNR with different pilot densities and 50 km/h user velocity.**

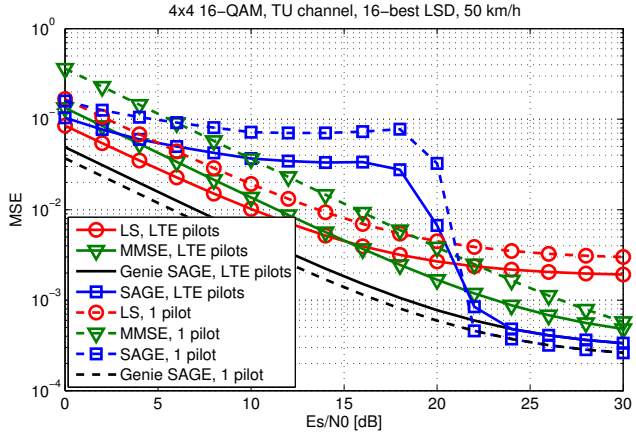

Fig. 42. 4×4 **16-QAM MSE vs. SNR with different pilot densities and 50 km/h user velocity.**

results for the same scenario in Figure 44. Figure 44 includes performance results of the MMSE filter with the known velocity, SNR and spatial correlation. The difference in performance of the MMSE filter with the known parameters is small compared to that of the MMSE filter with fixed parameters. Channels with different amounts of correlation were used. The highly correlated channel is generated with the BS azimuth spread of 2 degrees and the moderately correlated channel with an azimuth spread of

5 degrees. The average channel condition number is 90 for the correlated channel, 30 for the moderately correlated channel and 10 for the uncorrelated channel. The condition number can be calculated as the ratio of the maximum and minimum singular value ς_1/ς_N, where the singular values are obtained from the diagonal matrix Σ with the singular value decomposition of the channel matrix $\mathbf{H} = \mathbf{U}\Sigma\mathbf{V}^{\mathrm{H}}$. The performance is poor in the correlated channel. This is mostly due to the fact that the detector does not perform well in the highly correlated channel. This also has an impact on the performance of the SAGE algorithm as the quality of feedback from the detector is not high. The benefit obtained with the SAGE algorithm increases in the moderately correlated and uncorrelated channels.

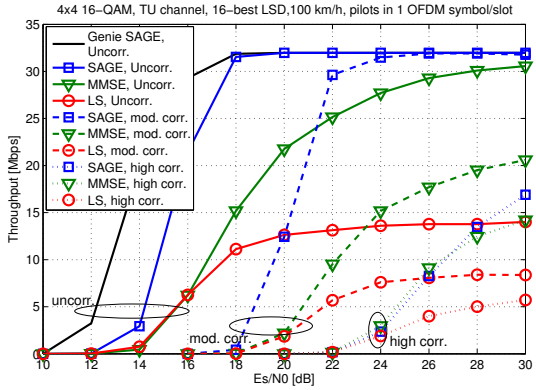

Fig. 43. 4×4 **16-QAM data transmission throughput vs. SNR with different channels and 100 km/h user velocity.**

Transmitting pilot symbols for all four antennas in the 1st OFDM symbol in a slot improves the SAGE estimator performance, especially with high user velocities because there is no need to combine the channel estimate of the two antennas in the current OFDM symbol with the channel estimate of the other two antennas from the previous OFDM symbol. The SAGE estimator also gets a better initial guess of the channel when all pilot symbols are transmitted in the same slot and is able to estimate the channel well in the decision directed mode. With the LTE pilots, the MMSE filter performs well. However, the performance of the MMSE estimator degrades when the pilot symbol density decreases, i.e. the MMSE estimator needs a sufficient pilot symbol density to perform well. The MMSE estimator cannot be used effectively to improve the

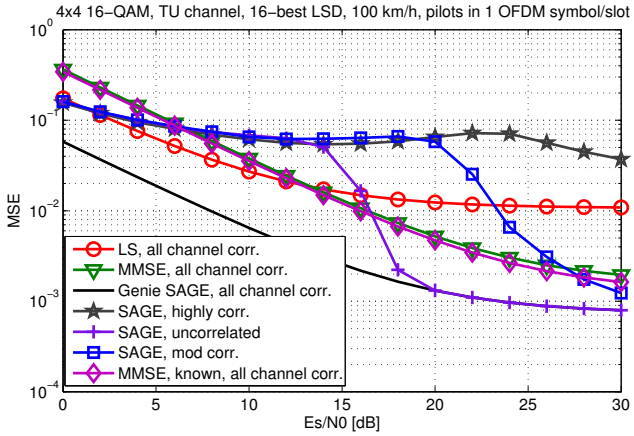

Fig. 44. 4×4 **16-QAM MSE vs. SNR with different channels and 100 km/h user velocity.**

throughput by transmitting less pilots as the SAGE channel estimator.

The performance in a 4×4 antenna system and 64-QAM is presented in Figure 45. Simulations were performed with both precalculated MMSE filter coefficients and with the MMSE filter from (45) using the actual SNR and user velocity. It can be seen that leaving out the spatial correlation $\Sigma_{\mathbf{h}_l}$ from (46) and (47) and using fixed values for the SNR and user velocity has only a minor impact on the performance. Furthermore, the throughput can be increased by decreasing the pilot symbol density and using the SAGE channel estimator.

The channel length and the delays of the taps were assumed to be known in the previous simulation results. However, in practice, they would have to be estimated. Figure 46 shows the performance with estimated channel tap delays where only five taps were estimated when the number of channel taps was six. The tap delays were estimated by calculating a LS estimate $\hat{\mathbf{h}}$ for 20 taps and using the diagonal values $\mathbf{P}_{\mathrm{LS}} = \mathrm{diag}(\hat{\mathbf{h}}^{\mathrm{H}}\hat{\mathbf{h}})$ to determine the strongest paths. Five paths from the estimated paths were used in channel estimation in Figure 46. The genie aided SAGE estimator also uses only five channel taps. The performance degrades with the estimated taps compared to the known tap delays in Figure 41, but the performance difference between the channel estimation algorithms does not change.

Simulations were also performed with an alternative channel model. The Winner suburban macro-cell channel with no line-of-sight (NLOS) was used to generate the

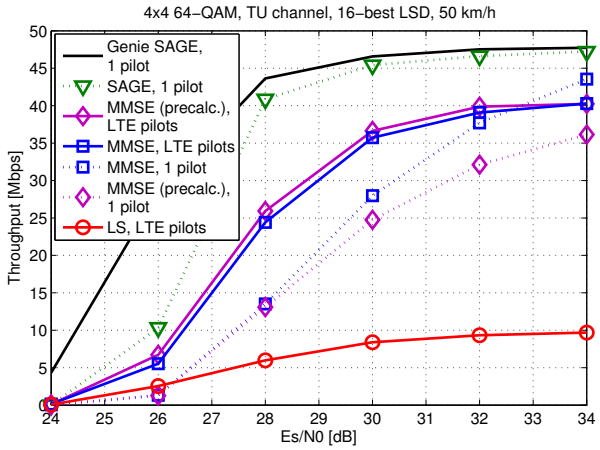

Fig. 45. 4×4 **64-QAM data transmission throughput vs. SNR with different pilot densities and 50 km/h user velocity.**

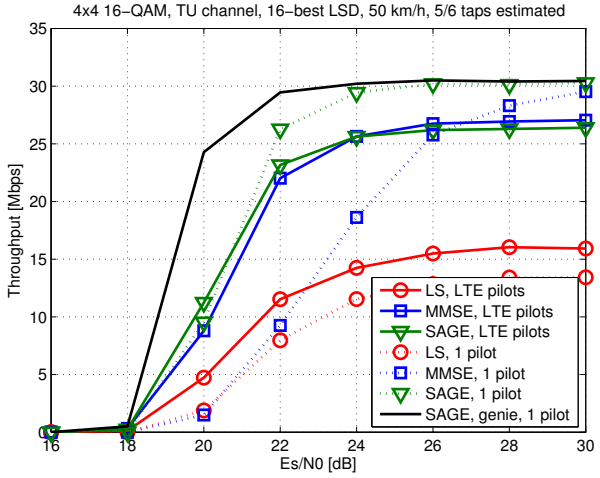

Fig. 46. 4×4 **16-QAM data transmission throughput vs. SNR with estimated channel tap delays and 50 km/h user velocity.**

results in Figure 47 and a line-of-sight (LOS) channel was used for the results in 48. The Winner channel models are based on channel measurements. The suburban macro-cell mobile stations are outdoors and the base stations are above rooftops [195]. The model generates more taps for the LOS channel than the NLOS channel. Even though the LOS channel has a stronger first tap, the NLOS channel has effectively three taps and

the LOS channel has seven taps. The performances of the MMSE and SAGE channel estimators are similar in the NLOS channel, but the SAGE algorithm performs better in the LOS channel with a higher number of taps.

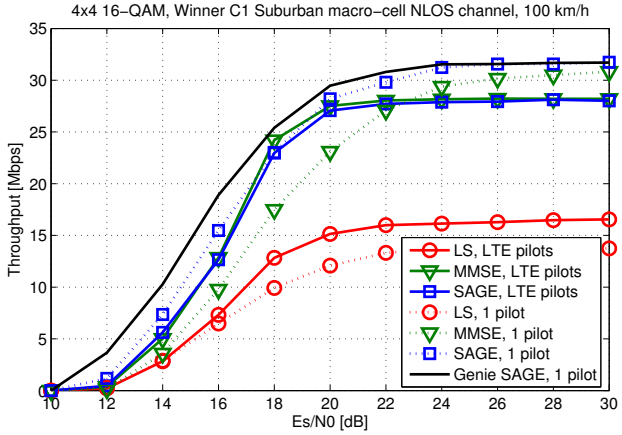

Fig. 47. 4×4 **16-QAM data transmission throughput vs. SNR with the Winner NLOS channel.**

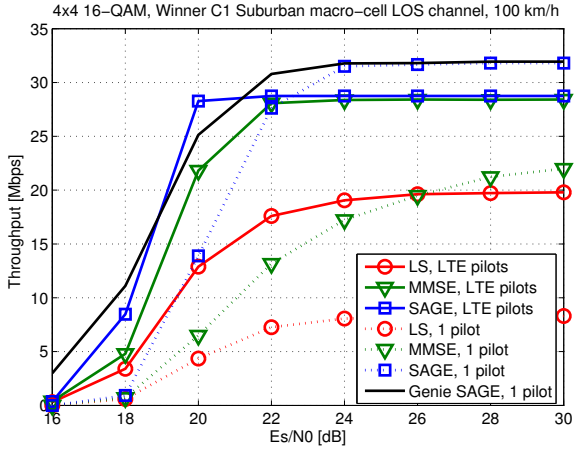

Fig. 48. 4×4 **16-QAM data transmission throughput vs. SNR with the Winner LOS channel.**

The performance of the MMSE and SAGE channel estimators with the LMMSE and K-best detectors are compared in Figure 49 in an uncorrelated channel. In such channels, the performance difference between the LMMSE and K-best detectors is smaller than in a correlated channel, as discussed in Chapter 4. The more low complexity LMMSE detector could be used with the SAGE channel estimator to achieve a similar performance as with the K-best detector and MMSE channel estimator. With a reduced pilot symbol density, SAGE estimator combined with LMMSE detection performs even better than the MMSE estimator with K-best detection. The low complexity of the detector would then balance the complexity difference in the receiver when comparing the SAGE and MMSE channel estimators.

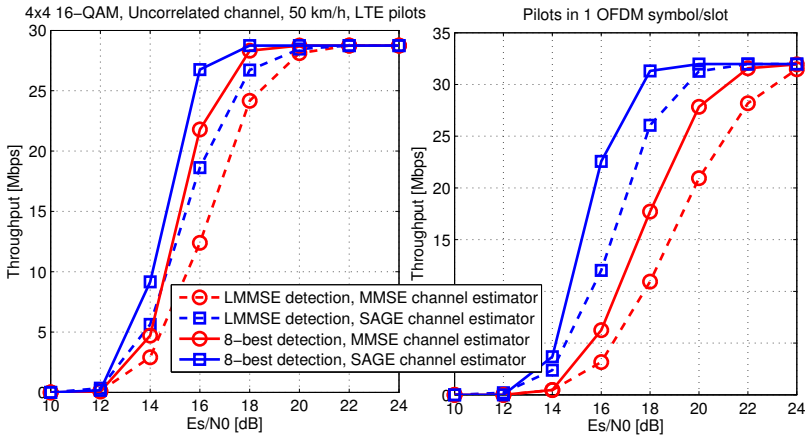

Fig. 49. 4×4 **16-QAM data transmission throughput vs. SNR with uncorrelated channel.**

5.3 Complexity reduction in channel estimation

The complexity of an algorithm can be measured, at least to some extent, by the number multiplications and additions performed during a certain processing time. The complexity of the time domain SAGE algorithm in the number of multiplications is $P(8LNMS_i + 4N)$ and in the number of additions $P((2NL+7)LNMS_i + 2N)$, where P is the number of subcarriers, L is the length of the channel and S_i is the number of SAGE iterations; $2N$ divisions are also needed. The number of multiplications in the LS

channel estimator is $4N_rLN$, where N_r is the number of pilot symbols. The number of multiplications in the decision directed LS estimation would be more than 12 million in a corresponding system when performing the $NL \times NL$ matrix inversion, where $N = 2$, $L = 6$ and $P = 512$ [212]. This is more than 60 times higher than in the DD SAGE estimator. The number of multiplications for obtaining the MMSE channel estimates with precalculated coefficients is $2NMLN_PB_f$, where B_f is the length of the filtering window and N_p is the number of LS channel estimates used in the MMSE filtering.

5.3.1 SAGE feedback reduction

The feedback to the SAGE channel estimator, i.e. the number of data symbols calculated from the decoder outputs, can be reduced. This lowers the complexity of the SAGE estimator, but can cause some performance degradation. Figure 50 shows the performance with different numbers of feedback data symbols used in the SAGE channel estimation. SAGE estimation with three iterations is equivalent to the SAGE estimation with 1 pilot curve in Figure 41. The number of multiplications and the performance degradation with different numbers of iterations S_i, channel taps L and feedback symbols used is presented in Table 37 in a system with 512 subcarriers. With half of the feedback symbols, every other subcarrier is used in the channel estimation. This decreases the complexity of the channel estimation almost by half. The performance can be increased with a higher number of SAGE iterations. In the 2×2 antenna case, a 0.5 dB performance degradation is observed when using every 4th symbol and 2 SAGE iterations. With 3 SAGE iterations, there is no performance degradation compared to using all the symbols. The estimation of the first five channel taps only will decrease the complexity, but the performance will also degrade. A good performance with lower complexity can be achieved by estimating six taps with 1/4 of symbols and 4 SAGE iterations.

As a comparison, there are 4,800 multiplications in the pilot symbol based LS channel estimator in the 2×2 system and 9,600 in the 4×4 system. The number of multiplications in the list sphere detector used in simulations are 142 k in the 2×2 system and 984 k in the 4×4 system [62]. The complexity in terms of multipliers is almost half of that of a sphere detector, but the achievable performance improvement can be significant.

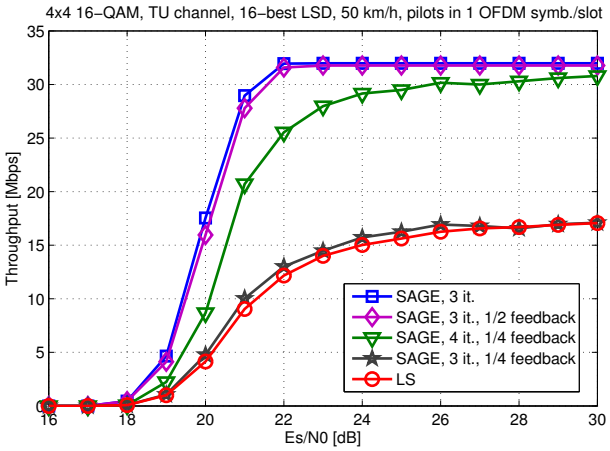

Fig. 50. 4×4 **16-QAM data transmission throughput vs. SNR with different numbers of used symbols and 50 km/h user velocity.**

Table 37. Number of multiplications with different parameters ([67], published by permission of IEEE).

Symbols	S_i	L	Performance degradation	Multiplications
2×2				
512	2	6	-	200704
256	2	6	+-0 dB	100352
128	3	6	+-0 dB	74752
128	2	6	-0.5 dB	50176
4×4				
512	2	6	-	794624
256	3	6	+-0 dB	593920
256	2	6	-[2-4] dB	397312
256	3	5	-[1-2] dB	495616
128	3	6	-[3-5] dB	296960
128	4	6	-0.5 dB	395264

5.3.2 Latency-performance trade-off

The LS channel estimation from the pilot symbols can be performed before detection in order to have a more timely channel estimate. However, the latency requirement of the channel estimator is less strict if channel estimation can be performed during detection. This can also have a major impact on the complexity. The alternative latencies in the receiver are presented in Figure 51. In the top part of the figure, the channel estimators have a latency of one OFDM symbol. Pilot symbols are received in the first OFDM symbol. The LS estimator then calculates the channel estimate during the detection of all data symbols in the first OFDM symbol. The LS channel estimate is used in the detection of the second OFDM symbol and as an input to the MMSE estimator or the SAGE estimator. The SAGE channel estimation can be performed when the decoding of the code word has finished. The data decisions of the first OFDM symbol are used to calculate the SAGE channel estimate while detecting the second OFDM symbol. The channel estimate is then used in the detection of the third symbol. Thus, the channel estimate used in the estimation is an estimate of the channel experienced two OFDM symbols ago. The other alternative is to use the result from the decision directed channel estimation in the detection of the next symbol, as shown in the bottom part of the figure. The channel estimate used in detection corresponds to the channel experienced in the previous OFDM symbol. The MMSE estimator can be used to predict a more current channel estimate from the delayed LS estimates as the coefficients can be adjusted according to the delay of the LS estimate.

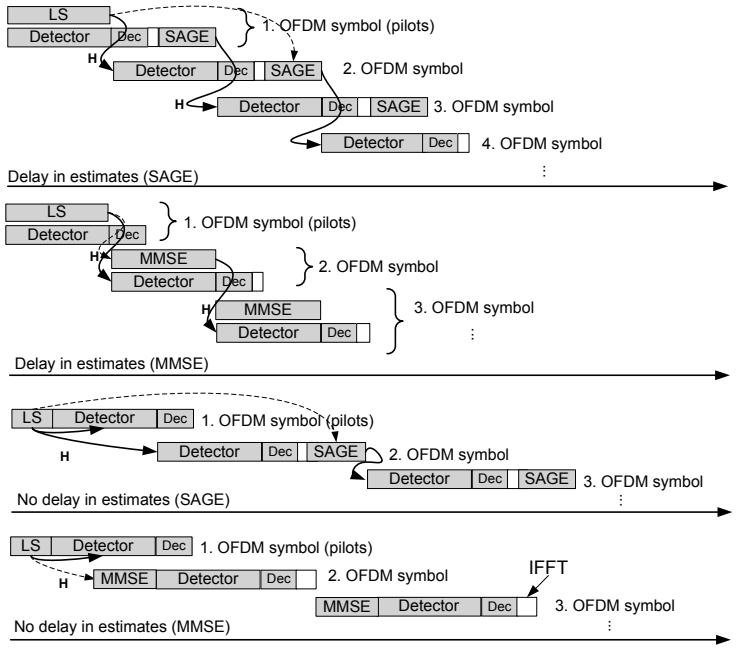

Fig. 51. Receiver latency alternatives; delay/no delay in channel estimation.

The performance of the channel estimators with different delays are presented in Figure 52 with a 50 km/h user velocity. The results with delay in channel estimation are obtained with the scheduling from the top part of Figure 51 and the results with no delay from the bottom part. The LS estimator was used with the LTE pilot structure and the SAGE estimator with a decreased pilot density, i.e. pilot symbols are transmitted in one OFDM symbol per slot. The impact of the delay on the performance increases with the user velocity. With 100 km/h user velocity, the performance degradation is more significant with the delayed channel estimation. The impact is high, especially on the SAGE estimator which is sensitive to the initial guess, i.e. the channel estimate from the previous OFDM symbol.

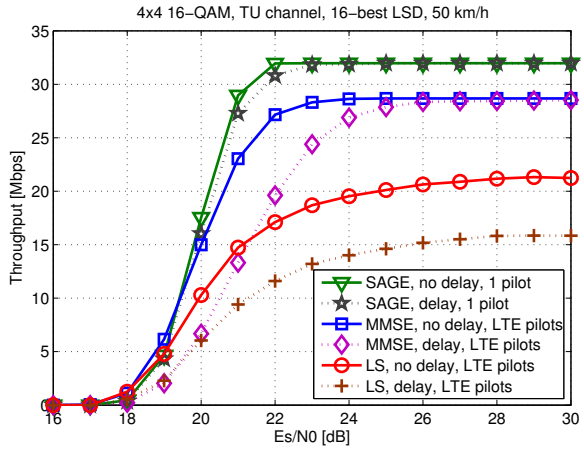

Fig. 52. 4×4 **16-QAM data transmission throughput vs. SNR with different delays and 50 km/h user velocity.**

5.4 Implementation of LS, MMSE and SAGE channel estimation

5.4.1 Architecture and memory requirements

The LS channel estimator includes complex multiplications of the LS coefficients and the received data symbols when performed from the pilot symbols. The calculation of each LNM channel coefficient includes P/N complex multiplications, after which the results are added together. For a 2×2 antenna system, there are 80 channel coefficients to be calculated. If the channel estimate can be obtained with the delay of one OFDM symbol, the latency for the calculation of one channel coefficient is 0.88 μs.

The MMSE channel estimator consists of multiplications of the LS channel estimates with real valued coefficients. Each MMSE channel estimate coefficient $\hat{\mathbf{h}}^{\mathrm{MMSE}}_{m_R,m_T,l}$ is a composite of the N_P LS estimates from the filtering period. With the 4×4 system, $N_P = 3$ and the filtering period is 7 OFDM symbols. The MMSE channel estimator then performs six multiplications and four additions for each complex valued channel coefficient.

The architecture of the SAGE channel estimator for a 2×2 antenna system is presented in Fig 53. Each block corresponds to (50)–(54). The elements of $\bar{\mathbf{x}}_{m_T}$ in each

stream are squared and the results are added together in the symbol multiplication part. The inverses of the results are multiplied with $\bar{\mathbf{x}}_{m_T}$. These calculations from (51) can be performed separately from the iterative channel tap calculations. For each channel tap, N_c iterations are performed. The channel tap iterations are initialized by multiplying the symbol decisions $\bar{\mathbf{x}}_{m_T}$ with the channel taps from the previous OFDM symbol in the block corresponding to (52). In later iterations, the channel taps from previous iterations are used. L multiplication results from N layers corresponding to the channel to each receive antenna are added together and subtracted from the received symbol from each receive antenna. The result is then added to the first $\bar{\mathbf{x}}_{m_T}\hat{h}_{m_T m_R}$ multiplication result in the block corresponding to (50) and multiplied with $\mathbf{x}_i^{-1}$ in the block corresponding to (51). A channel tap is obtained by adding together the results from the N_c iterations. The total number of iterations in calculating all the channel taps is $MNLS_iN_c$.

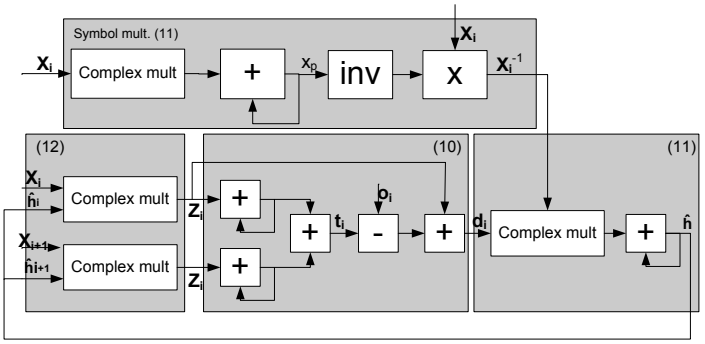

Fig. 53. The architecture of the SAGE channel estimator.

The precision of the variables required to sustain the performance close to that of the floating point variables were determined. The minimum word lengths for the channel estimators are presented in Table 38 in (word length, integer length, sign) format. The word lengths were determined with computer simulations using the same parameters as those in Section 5.2. The performance of the fixed point channel estimators compared to those of the floating point estimators are presented in Figure 54. Some performance degradation is allowed in the fixed point estimators in order to keep the complexity low as reaching the floating point performance may require a considerable increase in the word lengths.

The total number of bits required in the variables, the bits out of the word length used for the integer part and if the variable is signed or unsigned are shown in the table.

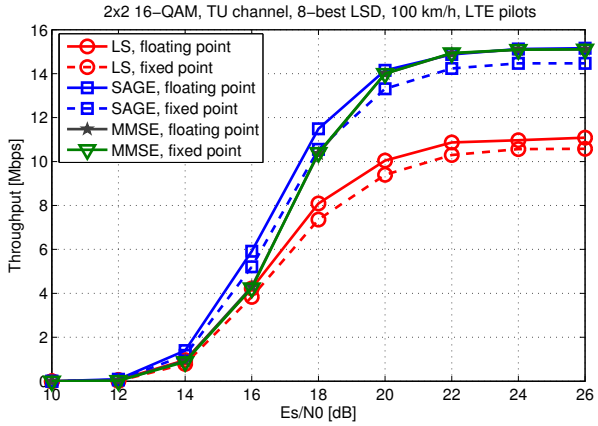

Fig. 54. 2×2 **16-QAM data transmission throughput vs. SNR with fixed word lengths.**

The variables in the SAGE channel estimator correspond to those in Figure 53 and the corresponding block is denoted by (10)-(12). The LS coefficients are the precalculated results of $(\mathbf{F}^H\mathbf{X}^H(n)\mathbf{X}(n)\mathbf{F})^{-1}\mathbf{F}^H\mathbf{X}^H(n)$ from pilot symbols. The received signal vector $\bar{\mathbf{y}}$ is in frequency domain in the LS estimator and $\mathbf{y}_i$ is in time domain in the SAGE channel estimator. The MMSE coefficients are precalculated and real valued.

Table 38. Word lengths in channel estimation.

SAGE		LS		MMSE	
Variable	(W_l, I_l, S_l)	Variable	(W_l, I_l, S_l)	Variable	(W_l, I_l, S_l)
$\bar{\mathbf{X}}_i$ (11)	(8,3,1)	$\bar{\mathbf{y}}$ (FD)	(16,4,1)	MMSE coeff.	(13,2,1)
$\bar{\mathbf{X}}_i^{-1}$ (11)	(12,2,1)	LS coeff.	(12,2,1)	$\hat{\mathbf{h}}_{\mathrm{MMSE}}$	(14,2,1)
x_p (11)	(17,13,0)	$\hat{\mathbf{h}}_{\mathrm{LS}}$	(13,2,1)		
$1/x_p$ (11)	(17,1,0)				
$\hat{\mathbf{h}}_i$ (11),(12)	(18,4,1)				
$\mathbf{t}_i$ (10)	(12,5,1)				
$\hat{\mathbf{z}}_i$ (12)	(12,4,1)				
$\mathbf{o}_i$ (TD) (10)	(8,4,1)				
$\mathbf{d}_i$ (10)	(12,4,1)				

The amount of memory required to store the LS coefficients precalculated from the pilot symbols is 14.4 Kbit assuming that the pilot symbols are the same in each OFDM symbol. The highest amount of memory in the MMSE filter is needed in storing the

LS channel estimates from N_P OFDM symbols. The required amount of memory is 17.5 Kbit in the 4×4 antenna system. In the SAGE channel estimator, the memory requirement for the symbol expectations $\bar{\mathbf{x}}_i$ is 16.4 Kbit in the 2×2 antenna system and 32.8 Kbit in the 4×4 antenna system. The highest amount of memory in the SAGE estimator would be the 1.2 Mbit for storing the interim results for $\hat{\mathbf{z}}_i$ but this is partly included in the following implementation results unlike the previously discussed memory requirements for the LS and MMSE filters.

5.4.2 Implementation results

Catapult ® C Synthesis tool [188] was used in the implementation of the receivers. The Synopsys Design Compiler was used in synthesizing the VHDL along with the UMC 0.18 μm CMOS technology. The FFTs are not included in the complexity estimations. The complexity and power consumption of each channel estimator is comparable only to other channel estimators presented in this work as the results depend on the used implementation method and library. However, a few other channel estimation implementations from the literature will be briefly discussed.

The implementation results for the LS channel estimator and MMSE filter are presented in Table 39 with different processing times. The estimators were implemented for 2×2 and 4×4 antenna systems and for a 5 MHz bandwidth. The processing time of 71 μs corresponds to the case of delay in channel estimates and the shorter processing time corresponds to the no delay case shown in the bottom part of Figure 51. The corresponding performance results were presented in Figure 52. The detector latency was assumed to be half from the 71 μs OFDM symbol duration, but the detector itself is not included in the complexity estimates. The LS estimator latency can then be 38 μs in the 2×2 antenna system and 33 μs in the 4×4 antenna system. The decoder latency [210] is also included in the latency calculations and each codeword is assumed to be mapped to a single slot and not interleaved over multiple slots. The gate count increases with the bandwidth in the LS estimator and the results can be scaled to higher bandwidths. The longer processing delay does not have a major impact on the complexity, but the power consumption can be decreased. This is due to the reduced clock frequencies in the case of the longer processing delay.

Table 39. Synthesis results for the LS and MMSE channel estimators with different latencies.

	No delay		Delay	
	LS	MMSE	LS	MMSE
2×2				
Processing time	38 μs	38 μs	71 μs	71 μs
Clock frequency	95 MHz	95 MHz	51 MHz	51 MHz
Equivalent gates	3763	3213	3730	3213
Power consumption	8.3 mW	5.2 mW	4.8 mW	2.8 mW
4×4				
Processing time	33 μs	33 μs	71 μs	71 μs
Clock frequency	146 MHz	146 MHz	102 MHz	68 MHz
Equivalent gates	3759	4549	3763	4375
Power consumption	13.2 mW	10.2 mW	8.9 mW	4.6 mW

The implementation results for the SAGE channel estimator are presented in Table 40. There are two target processing times for the SAGE estimator. The SAGE channel estimator has 31 μs in the no delay case to calculate the channel estimates in the 2×2 antenna system when the detector latency, the decoder latency of 5 μs, the symbol expectation latency of 1 μs and the IFFT [215] latency of 1 μs is subtracted from the OFDM symbol time. The symbol expectation calculation was implemented with the architecture from [62] and the gate count of 5.5 k gates was added to the SAGE estimator complexity in Table 40. In the 4×4 antenna system, the decoder and IFFT have higher latencies and the processing time for SAGE channel estimation is only 25 μs.

The longer processing times of 64 μs and 59 μs correspond to the case when channel estimation is performed during the detection of the following OFDM symbol. The IFFT complexity was not considered in the total complexity. An IFFT block could be added to the receiver or the FFT with scaling could be reused, timing permitting. The LS estimator would be included in the receiver with SAGE channel estimator and the complexity and power estimates would have to be added together to get the total complexity of the SAGE channel estimator.

Table 40. Synthesis results for the SAGE channel estimator with different latencies.

	Delay	No delay
2×2		
Processing time	64 μs	31 μs
Symbols, S_i	1/2, 3	1/2, 4
Clock frequency	144 MHz	165 MHz
Equivalent gates	34.6 k	58.2 k
Power consumption	93 mW	189 mW
4×4		
Processing time	59 μs	25 μs
Symbols, S_i	1/4, 4	1/4, 4
Clock frequency	104 MHz	147 MHz
Equivalent gates	113.4 k	210 k
Power consumption	257 mW	604 mW

Implementation results for MIMO channel estimators have not been presented extensively in the literature; this is particularly true for decision-directed algorithms. Quantitative comparison to existing work in terms of performance and complexity can be difficult as the simulation setups and system models differ from the ones in this work. Therefore, a thorough performance-complexity comparison to other work is unfeasible and it is one of the reasons different channel estimation algorithms were compared in this work. Comparison in terms of complexity has additional challenges, such as different implementation technologies and methods used. However, a few implementations are briefly introduced.

The approximate linear MMSE channel estimator from [165] uses the noise and correlation in calculating the coefficients. The implementation cost is 49 k gates, but the algorithm is different from the MMSE filter in this work making a comparison difficult. Data carriers are exploited in channel estimation for calculating channel variations in [167]. The algorithm provides better performance in fast fading scenarios, but the complexity of the channel estimator is 1,901 k gates. Furthermore, the implementation was done for a wireless local area network (WLAN) system. An implementation of a decision feedback channel estimator for space-time block code system was introduced in [216]. However, the performance is not comparable to the spatial multiplexing system in this work and the complexity for the one receive antenna implementation of [216] is higher than that of the SAGE estimator implementation for four antennas in this work.

The LS estimator is used throughout this work for obtaining the initial channel estimates from pilot symbols and the SAGE estimator for updating the channel estimates. The use of DD LS estimation would be prohibitive because of the high complexity, as stated in Section 5.2. With higher bandwidths or numbers of antennas, the time in which the SAGE channel estimation should be performed is shorter due to the increased decoder and FFT latencies. This results in higher complexity and power consumption. In terms of throughput per number of gates, the pilot only LS estimator uses the least number of gates per bit. However, in higher velocities, the MMSE and SAGE estimators would greatly improve the performance. Furthermore, the throughput can be increased by decreasing the pilot symbol density and using the SAGE estimator in calculating the channel estimates.

The energy efficiency of the pilot based LS, MMSE and the DD SAGE channel estimators is presented in Table 41. The throughput is achieved in a 4×4 antenna system at 22 dB with 50 km/h user velocity, as illustrated in Figure 52. The throughput with perfect channel state information would be 32 Mb/s with pilot symbols in one OFDM symbol per slot. The power consumption of the LS estimator is included in all the estimators. The MMSE estimator with processing delay has the best energy efficiency, but the SAGE estimator with delay can be used for improved throughput. When using the SAGE channel estimator at the receiver, less transmit power is needed for achieving the required throughput.

Table 41. LS, MMSE and SAGE energy efficiency comparison.

Estimator	Pilots	Delay	Throughput	Energy/bit
LS	LTE	No	17.1 Mb/s	0.77 nJ/b
LS	LTE	Yes	11.6 Mb/s	0.767 nJ/b
MMSE	LTE	No	27.2 Mb/s	0.86 nJ/b
MMSE	LTE	Yes	19.6 Mb/s	0.388 nJ/b
SAGE	1 pilot	Yes	31.2 Mb/s	8.6 nJ/b

5.5 Discussion

The performance of the DD SAGE channel estimation with the possibility of using it to improve the performance from the pilot symbol based estimators was considered. The

least squares estimator was used in obtaining the channel estimates from pilot symbols. Time domain correlation of the channel estimates was exploited in the MMSE filter when calculating estimates for symbols with no pilots. The theoretical complexity of the SAGE algorithm and some complexity reducing modifications were presented. The implementation results for the pilot based LS estimator, the SAGE channel estimator and the MMSE filter were presented.

The complexity and power consumption of the LS and MMSE estimators are low. The delay after which the channel estimates from the SAGE estimator are available for detection has a high impact on the complexity and performance. The complexity and power consumption can be high when using the SAGE estimator with a short processing delay. A good performance-complexity trade-off can be achieved by allowing a longer processing delay for the SAGE estimator.

The MMSE filter and the SAGE estimator improve the pilot symbol based LS estimator performance with high user velocities when the channel changes frequently between pilot symbols. The throughput can be increased by decreasing the pilot symbol density and transmitting data instead of pilot symbols. The SAGE estimator can then be used in calculating channel estimates when pilot symbols are not transmitted. The SAGE channel estimator would be a good choice for systems where training is performed in the beginning of the transmission or less frequently. The MMSE estimator is suitable for systems with high pilot densities as it has a low complexity and it is able to sustain acceptable performance.

6 Interference mitigation in MIMO-OFDM systems

In this chapter, the performance and the complexity of suppressing CCI at the downlink receiver are considered. The main focus is on the 2×4 system where two MIMO streams are transmitted. Interference mitigation is beneficial also in other MIMO cases and the 2×2 and 4×4 schemes are also studied. The LTE standard specifies four antennas in the terminal. The extra degrees of freedom could be used for interference suppression, making the 2×4 system a case of interest. The base station can have more than two transmit antennas, which could be used for multi-user MIMO in the cell or for transmit diversity. However, the suppression of interference from neighboring cells is studied in this work and the aforementioned schemes are not included here. An OFDM system is assumed, but the interference suppression methods could also be extended to uplink where a 2×4 would be even more relevant.

The interference is measured on the pilot subcarriers and the IN-SCM is used in channel estimation and data detection. Noise power level estimation is also performed in the receiver. Both the linear minimum mean square error and the nonlinear maximum likelihood based detector are considered. The received data is whitened before nonlinear detection by using the result of an eigenvalue decomposition. The accuracy of the EVD has an impact on the structure of the covariance matrix. Both the unstructured and structured model for the covariance matrix with different degrees of accuracy are applied and the complexity-performance trade-off is compared. Eigenspace tracking is also used to reduce the complexity of the EVD. Furthermore, an adaptive algorithm for the interference suppression and EVD calculation is proposed in order to achieve a good performance in all interference scenarios.

This chapter discusses the complexity and performance of co-channel interference mitigation since the combination has not been considered in the literature. Different methods and their implementation complexities are compared. Another contribution of the chapter is an adaptive algorithm for CCI mitigation, which obtains a good performance with the possibility for power savings.

The rest of the chapter is organized as follows. The receiver algorithms, including interference mitigation and detection, are introduced in Section 6.1 and some performance results are presented in Section 6.2. The complexities of the different interference

suppression methods are compared in Section 6.3, where the VLSI implementation results are presented. Section 6.4 includes discussion on the results. The results presented in this chapter have not been previously published but a part of the results has been submitted as a journal publication.

6.1 Receiver algorithms

The receiver structure is presented in Fig. 55. The LS channel estimator is used in calculating the channel estimates from pilot symbols. The received signal vector is transformed into frequency domain before the LS channel estimation. The result of the LS estimator is in time domain as shown in (55) and it has to be transformed into frequency domain for the detector with the second FFT. The MMSE filter can be used to filter the LS channel estimates in high velocity scenarios [156]. The CCI block calculates the IN-SCM and the noise variance from the channel estimates, pilot symbols and received signal vectors. Results with decoder feedback are not reported in this work due to the latency and error propagation issues.

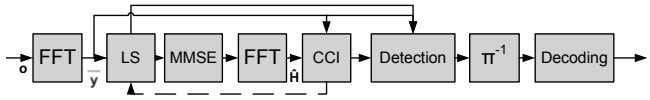

Fig. 55. The receiver structure.

6.1.1 Channel and noise variance estimation

The LS estimate of the channel can be calculated as [74]

$$\hat{\mathbf{h}}_{m_R}(n) = (\mathbf{F}^{\mathrm{H}}\mathbf{X}^{\mathrm{H}}(n)\mathbf{X}(n)\mathbf{F})^{-1}\mathbf{F}^{\mathrm{H}}\mathbf{X}^{\mathrm{H}}(n)\overline{\mathbf{y}}_{m_R}(n), \tag{55}$$

where $\mathbf{X}$ contains the pilot symbols. The calculation of the LS channel estimate from the pilot symbols is simple as the matrix inversion can be calculated in advance and the only calculation to be performed in real time is multiplication with the received signal, as discussed in Chapter 5.

Maximum likelihood channel estimation based on pilot symbols is equivalent to the LS estimation in additive white Gaussian noise when the number of pilot symbols is larger than the channel length. The IN-SCM can be included in the channel estimation.

The ML channel estimates, which can be also seen as weighted LS estimates, can then be calculated as [74, 175]

$$\hat{\mathbf{h}}_{m_R}(n) = (\sum_{k=1}^{P} \mathbf{F}_k^{\mathrm{H}} \mathbf{Q}_{i_k}^{-1} \mathbf{F}_k)^{-1} \sum_{k=1}^{P} \mathbf{F}_k^{\mathrm{H}} \mathbf{Q}_{i_k}^{-1} \overline{\mathbf{y}}_{m_R}(n) \mathbf{x}_k^{\mathrm{H}}(n), \tag{56}$$

where $\mathbf{Q}_i$ is the IN-SCM, $\mathbf{F}_k$ is $\mathbf{f}_k \otimes \mathbf{I}_\mathbf{M}$, $\mathbf{f}_k$ is the kth row of the $P \times L$ truncated Fourier matrix and $\mathbf{x}_k(n)$ is the transmitted pilot signal on the kth pilot subcarrier. The calculation of the channel estimate requires a $ML \times ML$ matrix inversion.

The unbiased noise variance estimate on a receive antenna can be calculated as

$$\gamma_{m_R} = \frac{1}{N_r - 1} \sum_{k=1}^{N_r} |(\mathbf{y}_k(n) - \hat{\mathbf{H}}_k(n)\mathbf{x}_k(n))_{m_R} - \mu|^2, \tag{57}$$

where the variance is calculated over all the pilot subcarriers N_r and μ is the average of the values $(\mathbf{y}_k(n) - \hat{\mathbf{H}}_k(n)\mathbf{x}_k(n))_{m_R}$, $k = 1, ..., N_r$. The noise variance can be averaged over the receive antennas, as well as over consecutive subframes.

6.1.2 Detection

The spatial covariance matrix is needed both in a linear MMSE detector and ML based detector for improved performance. The LMMSE filter can be calculated as

$$\mathbf{W} = (\hat{\mathbf{H}}\hat{\mathbf{H}}^{\mathrm{H}} + \mathbf{Q}_i)^{-1} \hat{\mathbf{H}}^{\mathrm{H}}, \tag{58}$$

where the covariance matrix is used instead of the noise variance matrix $\sigma^2\mathbf{I}$. If the covariance matrix is not available, the LMMSE filter can be approximated using the noise variance estimates as

$$\mathbf{W} = (\hat{\mathbf{H}}\hat{\mathbf{H}}^{\mathrm{H}} + \Gamma)^{-1} \hat{\mathbf{H}}^{\mathrm{H}}, \tag{59}$$

where Γ is a diagonal matrix containing the noise variance estimates γ_{m_R}. The received signal is filtered with the LMMSE filter and the log-likelihood ratios (LLR) can be calculated with a soft demodulator or as bit metric approximations [112], as explained in Section 4.2.

The IN-SCM is needed in the LLR calculation in the nonlinear detector. The log-likelihood ratio $L(b_k)$ for the transmitted bit k can be determined as

$$L_D(b_k|\mathbf{y}) = \ln \frac{\Pr(b_k = +1|\mathbf{y})}{\Pr(b_k = -1|\mathbf{y})}, \tag{60}$$

as presented in (11) in Chapter 4. The likelihood function (13) on any subcarrier can be calculated using the covariance matrix as

$$p(\mathbf{y}|b) = \frac{1}{|\mathbf{Q}_i|}\exp(-||\mathbf{Q}_i^{-1/2}(\mathbf{y}-\hat{\mathbf{H}}\mathbf{x})||^2). \tag{61}$$

6.1.3 Interference estimation and processing

The interference can be measured on the pilot subcarriers by subtracting the estimated channel from the received signal. The IN-SCM on a subcarrier is defined as

$$\mathbf{Q}_i = E[(\mathbf{y}-\mathbf{H}\mathbf{x})(\mathbf{y}-\mathbf{H}\mathbf{x})^{\mathrm{H}}], \tag{62}$$

where $\mathbf{H}$ is the channel matrix in frequency domain and $\mathbf{x}$ contains the transmitted pilot symbol. The IN-SCM estimate

$$\hat{\mathbf{Q}}_i = \frac{1}{T_r}\sum_{n=1}^{T_r}(\mathbf{y}(n)-\hat{\mathbf{H}}(n)\mathbf{x}(n))(\mathbf{y}(n)-\hat{\mathbf{H}}(n)\mathbf{x}(n))^{\mathrm{H}} \tag{63}$$

is obtained by averaging over a training period T_r.

A structured model for the covariance can be applied in order to improve the accuracy of the estimation [174]. The IN-SCM can be modeled as

$$\hat{\mathbf{Q}}_i = \Psi + \hat{\sigma}^2\mathbf{I}, \tag{64}$$

where Ψ has the EVD as $\Psi = \mathbf{V}_m(\delta_m - \hat{\sigma}^2\mathbf{I}_m)\mathbf{V}_m^{\mathrm{H}}$, the eigenvectors $\mathbf{V}_m$ and the eigenvalues δ_m correspond to the m dominant eigenvalues and $\hat{\sigma}^2$ is the average of the last $M-m$ eigenvalues.

The whitening of the channel matrix and the received signal vector in the detector can be performed by multiplying them with the inverse square root of the covariance matrix estimate $\hat{\mathbf{Q}}_i$ as presented in (61). The inverse square root of a Hermitian matrix can be calculated from its eigenvalue decomposition $\hat{\mathbf{Q}}_i = \mathbf{V}\mathbf{D}\mathbf{V}^{\mathrm{H}}$ as

$$\hat{\mathbf{Q}}_i^{-1/2} = \mathbf{V}\mathbf{D}^{-1/2}\mathbf{V}^{\mathrm{H}}, \tag{65}$$

where $\mathbf{D}$ is a diagonal matrix containing the eigenvalues of $\hat{\mathbf{Q}}_i$ and $\mathbf{V}$ contains the corresponding eigenvectors.

The EVD can be calculated by row-cyclic Jacobi sweeping [73] where left and right side transformations are applied. The input matrix is diagonalized iteratively by

applying the transformations on submatrices. The rotations can be calculated with coordinate rotation digital computer (CORDIC) iterations. A more accurate result can be obtained by applying several sweeps of the algorithm. Each sweep makes the input matrix more diagonal and results in more accurate eigenvalues. If the interference level or signal-to-noise ratio is low, the unstructured covariance matrix may give a better performance when the EVD for (65) is calculated with only one sweep. The off-diagonal values are discarded and only the diagonal values are used. The covariance matrix after one sweep can be written as

$$\hat{\mathbf{Q}}_i = \mathbf{V}^{\mathrm{H}}(\mathbf{D} - \mathbf{B_d})\mathbf{V}, \tag{66}$$

where $\mathbf{B}_d$ contains the off-diagonal elements of $\mathbf{D}$. With one sweep of the algorithm, the most significant eigenvalues are obtained, which leads to $\mathbf{Q}_i^{-1/2}$ close to that calculated with the structured covariance matrix.

The accuracy of the EVD with a low number of sweeps may be improved by tracking of eigenspaces [217]. The covariance matrix $\hat{\mathbf{Q}}_i$ can be multiplied from both sides with the previous eigenvector matrix $\mathbf{V}$ before performing the EVD. This makes the covariance matrix more diagonal, which results in the need for fewer sweeps in the EVD. The new covariance matrix before the EVD can be calculated as

$$\tilde{\mathbf{Q}}_i(n+1) = \mathbf{V}^{\mathrm{H}}(n)\hat{\mathbf{Q}}_i(n+1)\mathbf{V}(n) \tag{67}$$

and the eigenvector matrix after the EVD is obtained from

$$\tilde{\mathbf{V}}(n+1) = \mathbf{V}(n)\mathbf{V}(n+1). \tag{68}$$

CCI mitigation adaptation

In order to adapt the CCI calculation, the eigenvalue ratio can be used. The ratio of the maximum eigenvalue to the sum of all eigenvalues

$$\kappa = \delta_{max} / \sum_{i=1}^{M} \delta_i, \tag{69}$$

where δ_{max} is the largest eigenvalue and $\sum_{i=1}^{M} \delta_i$ is the sum of all eigenvalues with different numbers of interferers is presented in Figure 56. The values for κ were obtained after performing one Jacobi sweep in the EVD. A 2×4 MIMO system was assumed, resulting in a 4×4 covariance matrix. The values do not depend on the

modulation scheme of the interference or the desired signal. With low SNR and high signal-to-interference ratio (SIR), the eigenvalue ratio is small. With a low eigenvalue ratio, the interference is not dominating and interference mitigation brings no gain. With high SNR and low SIR, the ratio is close to one when there is only one interfering signal. The ratio decreases when the number of interferers increases. When there is no interference, the ratio is close to 0.5 regardless of the SNR.

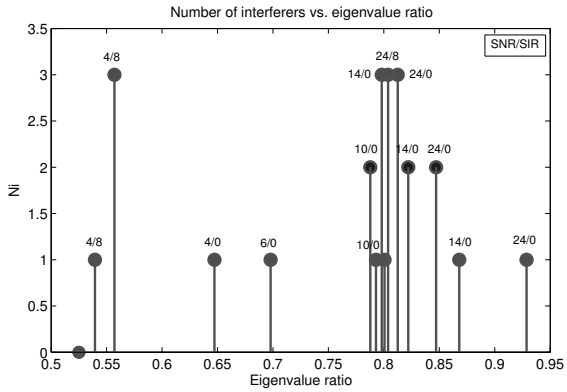

Fig. 56. Eigenvalue ratios with different numbers of interferers.

The proposed adaptation algorithm starts by determining the number of sweeps in the EVD. After the first sweep of the algorithm, the need for an additional sweep can be determined by calculating the eigenvalue ratio. If the ratio indicates more than one interferer being present, i.e. it is within a certain limit, another sweep is performed. With multiple strong interferers, the ratio is within certain limits, as can be seen in Figure 56. The other condition for continuing with the second sweep is a threshold formed by scaling the largest eigenvalue with the noise variance. The second step of the algorithm decides whether interference mitigation is performed. If κ is below a limit, interference is not suppressed.

6.2 Performance examples

The simulation parameters are the same as those used in Chapter 5 and the channel parameters were presented in Table 1. The nonlinear detector used in the simulations is a K-best list sphere detector with the list size of 8 and the LS estimator was used for

channel estimation. As earlier, the transmission throughput is defined to be equal to the information transmission rate of information bits times (1−frame error rate). Decoding was performed over one OFDM symbol in the simulations. The signal-to-interference ratio of 0 dB was assumed in the simulations. With high SIR, the interference can be seen as noise and interference suppression has no major impact on the performance. The estimated IN-SCM from (63) is used in the interference mitigation and the structured model from (64) is fixed to $m-1$ dominating eigenvalues. The EVDs are calculated with transformations using six CORDIC rotations.

The performance with one interferer with SIR of 0 dB is shown in Figure 57. The user velocity is 3 km/h. The interferer is present with probability of one. There is no throughput without interference mitigation. Similar performance is achieved with the structured model, the unstructured model with two sweeps, the adaptive algorithm and the unstructured model with one sweep and eigenspace tracking. The adaptive algorithm does not fully achieve the one sweep EVD performance in the low SNRs, but the performance difference in negligible. The performance improves at high SNRs with the algorithms using more iterations because the estimated covariance matrices are more accurate. At low SNRs, better performance is achieved when just one eigenvalue is used for the covariance matrix.

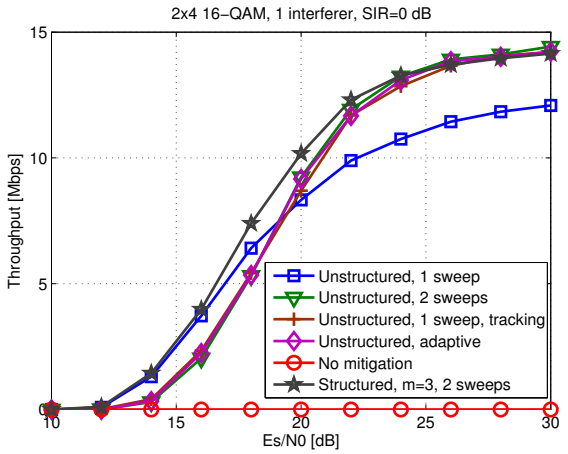

Fig. 57. 2×4 **16-QAM data transmission throughput vs. SNR with one interferer.**

The performance with one interferer present with the probability of 0.5, user velocity of 3 km/h and SIR of 0 dB is presented in Figure 58. In this case, the interference is

either present in all the subcarriers in an OFDM symbol or there is no interference in any of the subcarriers. The structured model has the best performance while the unstructured model with one sweep leads to roughly 2 dB performance degradation. The two sweep case has the worst performance. The eigenspace tracking does not improve the performance. The adaptive algorithm performs well, i.e. no interference mitigation is performed in low SNRs and a one sweep EVD is performed in the high SNRs.

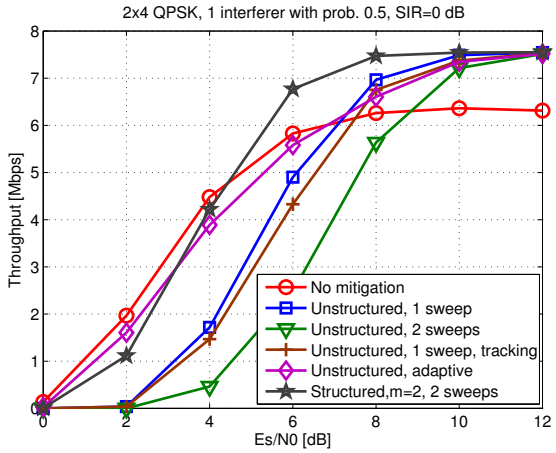

Fig. 58. 2×4 **QPSK data transmission throughput vs. SNR with max. one interferer.**

The performance with maximum of two interferers with a probabilities of 1 and 0.2 and SIR of 0 dB is presented in Figure 59. The user and interference velocity is 50 km/h. The MMSE filter is used to filter the LS channel estimates for improved performance in the high velocity case. The lower velocity cases do not benefit from MMSE filtering. The structured model gives the best performance and the adaptive algorithm and unstructured model perform also well. The performance is poor without interference mitigation.

The structured model or the number of sweeps in the EVD does not have an impact on performance in a 2×2 antenna case, as can be seen in Figure 60. The use of eigenspace tracking does not improve the performance either, as the 2×2 covariance matrix does not require additional accuracy. However, interference mitigation does improve the performance compared to the case of no mitigation. The difference in performance is larger in the 4×4 system. There, the unstructured model with one sweep

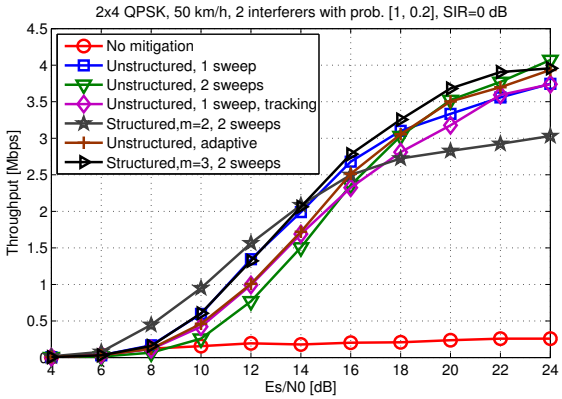

Fig. 59. 2×4 **QPSK data transmission throughput vs. SNR with max. two interferers.**

performs better than the two-sweep case and the adaptive algorithm performs also well. The structured model has the best performance, but the choice of wrong m can degrade the performance.

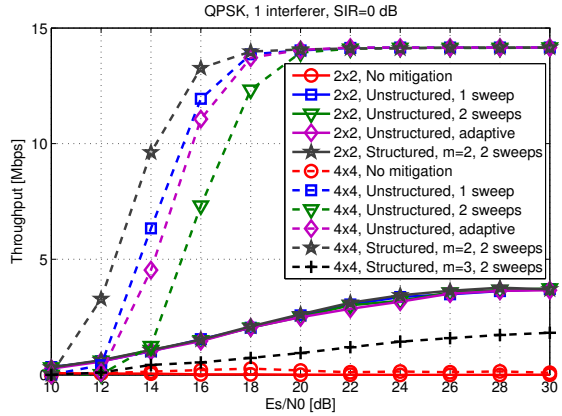

Fig. 60. 2×2 **and** 4×4 **QPSK data transmission throughput vs. SNR with one interferer.**

The performance with a linear MMSE detector is illustrated in Figure 61. One interfering signal is present with a SIR of 0 dB. The interfering signal has a velocity of 50 km/h, while the user velocity is 3 km/h. Using the noise variance estimate from (57)

improves the performance from the no mitigation case where the known SNR is used. The structuring of the covariance matrix with the EVD improves the performance from using the covariance matrix directly in (58). The use of the covariance matrix in the LMMSE filter calculation could have an impact on the complexity due to the possible increase in word lengths.

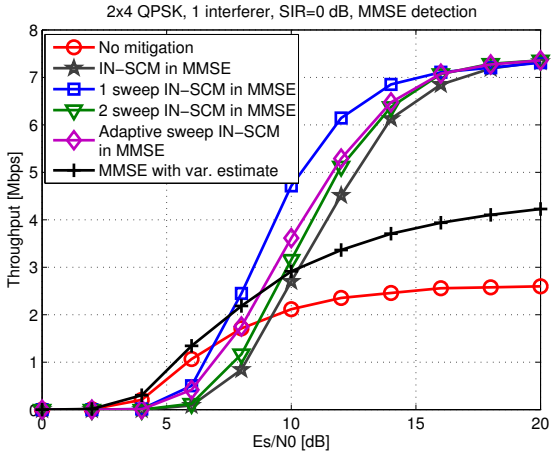

Fig. 61. 2×4 **QPSK data transmission throughput vs. SNR with one interferer and MMSE detection.**

The structured model leads to a good performance in the presented scenarios. However, the number of dominant interferers has to be estimated. This can be done for example with the rank estimation method from [174], but it will add extra complexity to the receiver and may not perform as well as applying a fixed value for the rank. The structured model may not provide a gain compared to the unstructured model when the number of interferers is larger than the difference between the number of transmit and receive antennas. The extra degrees of freedom are helpful in interference mitigation and without them, the structuring of the covariance matrix may not be successful. The unstructured model with one sweep performs well if the interference cannot be estimated accurately, such as in the case of low SNR and multiple interferers.

The impact of including the IN-SCM in the channel estimation as in (56) is presented in Figure 62. The user and interference velocities are 3 and 50 km/h. The channel estimation was performed with the true IN-SCM as well with the estimated covariance matrix. The largest difference in performance can be seen in high SNRs with the

known IN-SCM. However, the calculation of the channel estimate with (56) requires an $ML \times ML$ matrix inversion and the interference would be the strongest in the lower SNRs. There, the performance may even suffer from using the estimated IN-SCM in channel estimation. Therefore, the complexity cost of including the IN-SCM in the channel estimation is high compared to the achievable performance gain.

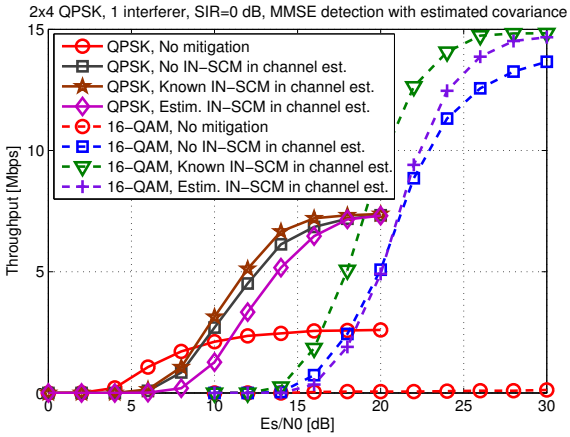

Fig. 62. Impact of IN-SCM in channel estimation on the performance in a 2×4 system.

A comparison of the LMMSE and K-best detectors with one interferer with SIR of 0 dB is given in Figure 63. The K-best detector performs better regardless of the interference mitigation method. Without interference mitigation, the performance with both detectors is poor. Structuring the covariance matrix with one sweep of the EVD improves the performance also in the LMMSE detector.

The results with adaptive modulation and coding are presented in Figure 64. The same setup as in Section 4.4.6 is used with the exception of all the transmission ranks from one to four are possible. The K-best and LMMSE detectors are compared in a case with no interference and one interferer with SIR of 0 dB. LS channel estimation is used. The K-best detector performs better than the LMMSE detector when there is no interference and the SNR is high enough for higher transmission ranks. The results are similar to those in Section 4.4.6, where the channel was assumed to be known in the receiver. With interference from a neighboring cell, the performance of the detectors is similar. The transmission rank in this case is more probably lower even in the high

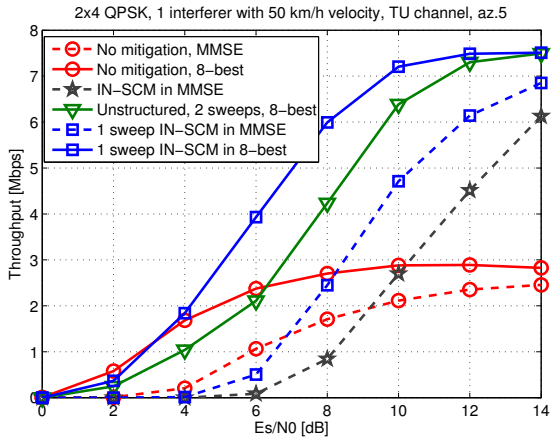

Fig. 63. 2×4 **QPSK data transmission throughput vs. SNR with one interferer and 8-best and MMSE detection.**

SNRs than in the case of no interference.

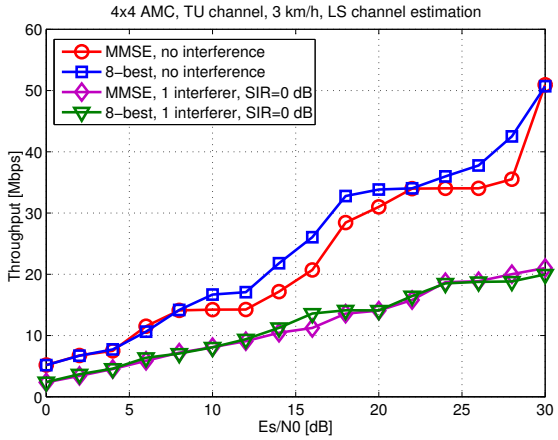

Fig. 64. AMC data transmission throughput vs. SNR with one interferer and 8-best and MMSE detection.

6.3 Implementation results

The top level structure of the CCI mitigation is presented in Figure 65. First, the noise and interference are calculated by subtracting the impact of the channel and the known pilot symbols from the received signal. The IN-SCM and the noise variance are calculated from the resulting vectors as in (63) and (57). The IN-SCM is averaged with the previous covariance matrix estimates. The EVD is performed for the estimated covariance matrix. The resulting eigenvectors $\mathbf{V}$ and the diagonal matrix $\mathbf{D}$ containing the inverse square root of the eigenvectors are used in calculating the inverse square root of $\hat{\mathbf{Q}}_i$. The received signal vector and the estimated channel are whitened with the matrix $\hat{\mathbf{Q}}_i^{-1/2}$ in the case of nonlinear detection. With linear detection, matrix $\hat{\mathbf{Q}}_i$ or its structured model can be used directly in the MMSE filter calculation.

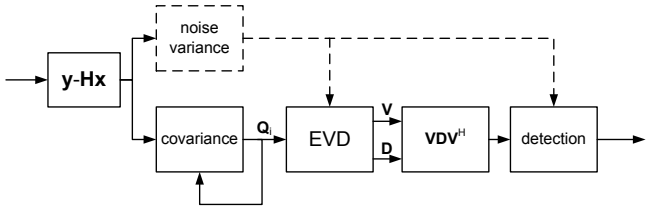

Fig. 65. The structure of the CCI mitigation.

The architecture for the EVD calculation is presented in Figure 66. The architecture has a maximum of two Jacobi sweeps. After the final sweep, the square root operation followed by an inverse is performed on the diagonal values of $\mathbf{D}$. Each sweep consists of three stages which include vectoring and rotation blocks. The angle for the rotation blocks is calculated in the vectoring blocks. The left side transformations for the inner rotations are calculated in the first rotation blocks followed by the right transformation for the matrix to be diagonalized. After the new angle calculation in the vectoring block, the right side Givens transformation are calculated followed by the left side transformations. Each vectoring and rotation block consists of six CORDIC iterations. The vectoring and rotation chain is performed three times in the first stage, two times in the second and once in the last stage. Depending on the sweep and stage of the algorithm, the number of rotations performed for the diagonalized matrix is between two and four.

The EVD algorithm used in the performance simulations was implemented with both

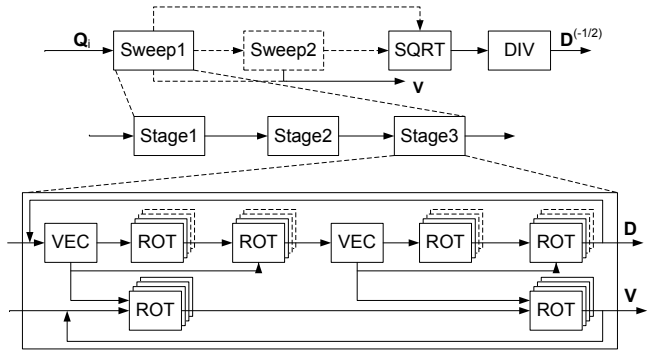

Fig. 66. The architecture of the EVD calculation.

one and two sweeps of the algorithm. The time in which the EVD has to be calculated was assumed to be 0.5 ms. A longer delay could be used for the low user velocity case, but 0.5 ms was found to be sufficient for also higher velocities. In the case of structured covariance matrix, the EVD has to be performed both for the structuring of the matrix, as well as the inverse square root calculation. There, the number of required sweeps is two. The complexity results for the structured model then include two EVD calculation blocks.

The required word lengths were determined via computer simulations. The performance with 20 bit word lengths in the EVD is presented in Figure 67. The sufficient word lengths in the interference and noise variance estimation are from 16 to 18 bits. The word lengths of 18 bits in the EVD would be sufficient in the lower SNR ranges, but 20 bit word lengths are required in the high SNRs. The performance does not degrade when only half of the covariance matrices in a frame are processed. The same covariance matrix is used for six consecutive subcarriers in that case. This will allow a longer latency for the EVD which will lead to a lower complexity or power consumption.

Catapult ® C Synthesis tool [188] was used in the implementation of the EVD. The Synopsys Design Compiler was used in synthesizing the VHDL along with the UMC 0.18 μm CMOS technology. The implementation was done for a 5 MHz bandwidth. With higher bandwidths, more covariance matrices would have to be processed, which would lead to a higher complexity.

The implementation results for the interference and noise variance estimation are presented in Table 42. The delay includes the processing of all the subcarriers, but individual subcarriers can be processed in a pipelined manner. The calculation of $\mathbf{y} - \mathbf{Hx}$ is performed before the noise variance or the IN-SCM can be calculated. The noise

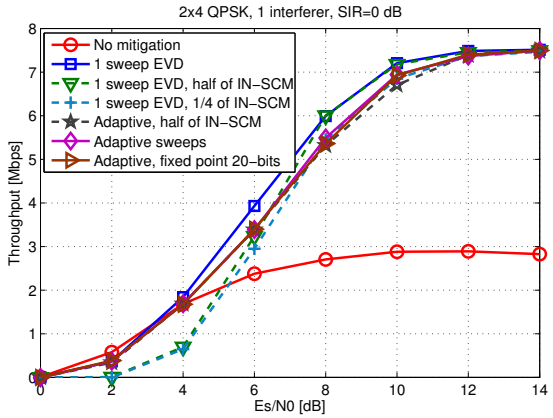

Fig. 67. The impact of complexity reduction and word lengths on the performance.

variance estimator has to process all the subcarriers before the noise estimate is obtained. The covariance calculation block calculates the IN-SCM matrices. The calculation of $\mathbf{VDV}^{\mathrm{H}}$ is performed after the EVD to form the inverse square root matrix. The implementation results do not include the use of the IN-SCM in detection.

Table 42. Implementation results for the interference estimation.

	Delay (cycles)	Delay (μs)	Gates	Power
$\mathbf{y} - \mathbf{Hx}$	627	12.5	7424	11 mW
Noise var. est.	1704	34	7117	4 mW
Covariance	3151	63	11.3 k	8.4 mW
$\mathbf{VDV}^{\mathrm{H}}$	2850	92	44 k	33.5 mW

The implementation results for the EVD are presented in Table 43 with different numbers of sweeps of the algorithm. The complexity of the algorithm with one or two sweeps is roughly the same, but the clock frequency is higher with the two sweep case. The structured model consists of two EVDs with two sweeps.

Table 43. Implementation results for the EVD.

	Unstr. 1 sw	Unstr. 2 sw	Struct. 2 sw
Delay (cycles)	783	1543	1543
Clock frequency	79 MHz	155 MHz	155 MHz
Gates	71 k	64 k	128.1 k
Power consumption	45.7 mW	78.5 mW	157 mW

Complexity comparison of different interference mitigation methods are presented in Table 44. The complexity includes the calculation of the covariance matrix as in (62), the eigenvalue decomposition and the calculation of the inverse square root from the results of the EVD. The adaptive algorithm also includes the noise variance estimate calculation and the eigenvalue ratio calculation. The tracking method includes the multiplication of the covariance matrix with the previous matrix $\mathbf{V}$ and the updating of $\mathbf{V}$ as in (67) and (68). The memory requirement for the eigenspace tracking is higher than that of the other methods because of the need to store the previous matrices $\mathbf{V}$. The power consumption for the adaptive algorithm is obtained for the two sweep case. The adaptive algorithm can obtain some power saving when performing only one sweep with a reasonable complexity while maintaining a good performance.

Table 44. Complexity of interference mitigation.

	Unstr. 1 sw	Adaptive sweep	Tracking
Gates	134 k	145 k	180 k
Power consumption	98 mW	145 mW	117 mW
Memory (bits)	54.4 k	54.4 k	83.2 k

6.4 Discussion

The interference and noise spatial covariance matrix was used for both channel estimation and detection. Both the unstructured and structured covariance matrix were considered and some complexity reducing techniques were presented. Interference mitigation was found to be crucial if strong interference is present. The accuracy of the EVD affects the

performance. The less accurate EVD performs better in scenarios where the quality of the covariance matrix is low. There, a lower number of estimated parameters leads to fewer erroneous parameters. An adaptive algorithm was proposed to control the interference suppression and the number of iterations performed in the EVD. Noise variance estimation was included in the adaptive algorithm. The algorithm performs well in all interference scenarios. Eigenspace tracking was also applied to lower the complexity of the EVD and was found to perform well in some scenarios.

The EVD required for the structuring of the covariance matrix, as well as for the inverse square root calculation was implemented with a high level synthesis tool to obtain the complexity numbers. The use of the structured model leads to a good performance at the expense of high complexity. Eigenspace tracking performs well, but has a higher complexity and memory requirements than the adaptive algorithm, which can be used to achieve a good performance while obtaining power savings.

7 Conclusions and future work

The thesis concentrated on finding feasible algorithms for a MIMO mobile receiver while improving the error rate performance and throughput. Data detection, channel estimation and interference mitigation were considered. The aim was to develop algorithms and architectures to meet the high performance and low power consumption requirements of the future mobile communication systems, as stated in Chapter 1. The performance of the algorithms was studied through computer simulation and the complexity and power consumption results were obtained via VLSI implementations. The previous and parallel work on detection, channel estimation and interference mitigation was introduced in Chapter 2. The system, signal and channel models for detection and channel estimation were presented in Chapter 3.

The performances and implementation complexities of the LMMSE, SIC, non-iterative and iterative K-best LSD receivers for MIMO–OFDM communications were compared in Chapter 4. The emphasis was on LTE specific system parameters and latency requirements. The SIC receiver was shown to outperform the K-best LSD with horizontal encoding in channels with low spatial correlation, but the result is reversed in channels with significant spatial correlation; the SIC receiver is not practically suitable for vertically encoded MIMO communications. Soft information feedback from the FEC decoder to the K-best LSD stage was also considered as a strategy to improve the performance. It provides up to 2 dB performance improvement. The choice of the receiver algorithm is emphasized when the number of antennas increases and the channel condition number is high. There, the nonlinear ML or MAP based receivers clearly outperform the linear receivers, but the price is remarkably increased computational complexity and power consumption.

The considered receivers were synthesized to an FPGA and an ASIC to get a solid ground for implementation complexity comparison. A modification on the tree search of the K-best LSD was presented to simplify its implementation with no compromise in its error rate performance. Thus, it can achieve double detection rate compared to the original K-best algorithm. On the selected FPGA, the SIC receiver is fast enough to process the number of subcarriers defined in the LTE standard for 20 MHz bandwidth with all modulations and 2×2 and 4×4 antenna configurations. The K-best LSD suffers from the timing bottleneck caused by the sorter, but the required detection rates

can be achieved by utilizing multiple detection blocks in parallel.

ASIC implementation results were also provided. The receivers were designed to have a detection rate, which would be enough for the LTE 20 MHz bandwidth. The K-best LSD was found to be more than twice as complex as the SIC receiver in the 2×2 antenna case, but in the 4×4 case, the complexity difference was smaller. The latency of the SIC receiver does not depend on the used modulation and it can be employed with higher order modulations. The latency of the K-best LSD increases with the modulation and the list size in both FPGA and ASIC implementations.

The detectors with the highest goodput and the lowest complexity on ASIC with correlated, moderately correlated and uncorrelated channels with a given SNR are presented in Table 45. It can be seen that the simpler LMMSE and SIC receivers can be used in the uncorrelated channel, but in the correlated channel, the K-best LSD gives the best goodput. The detector and the modulation order could be changed adaptively with the channel conditions and SNR in order to achieve the best possible goodput with the least amount of receive power.

Table 45. The detector with the best goodput (QAM constellation Ω) ([62], published by permission of IEEE).

SNR	Correlated	Mod. correlated	Uncorrelated
2×2 system			
2 dB	it. 16-best (4)	it. 16-best (4)	it. 16-best (4)
10 dB	16-best (4)	16-best (4)	LMMSE (4)
15 dB	SIC (4)	SIC (16)	SIC (16)
20 dB	it. 8-best (16)	SIC (64)	SIC (64)
4×4 system			
10 dB	it. 8-best (4)	8-best (4)	LMMSE (4)
15 dB	8-best (4)	LMMSE (4)	SIC (16)
20 dB	LMMSE (4)	8-best (16)	SIC (64)
25 dB	it. 8-best (16)	LMMSE (16)	LMMSE (64)

To obtain an insight of the impact of transmitter channel state information into the performance of the detector algorithms, the LMMSE, SIC and K-best detectors were further evaluated in a system with adaptive modulation and coding. The capacity metric was considered here, but the idea was to study the impact of adaptation on the receiver.

The use of other metrics would be an interesting topic of further study. The performance of the detectors was similar in the low SNR region, where the adaptation resulted in low rank transmission. The K-best detector improved the performance from LMMSE and SIC detectors in the high SNRs, where full rank transmission was used. The ASIC implementation results for detectors supporting all three modulation schemes were presented and were found to be similar to those of the fixed modulation schemes. In conclusion, a simple detector can be used for a low cost receiver, but the peak data rates may not be achieved. For a high performance receiver, a more complex detector algorithm is needed.

Chapter 5 focused on channel estimation. The aim was to address the performance degradation of a system with periodic pilot symbols, such as most of the mobile communication systems, when the user velocity is high or when the pilot overhead decreases the throughput. The performance and complexity of the LS, MMSE and the decision directed SAGE channel estimators were compared. The LS and MMSE estimators have a low complexity and power consumption. The SAGE estimator has a much higher power consumption. The MMSE filter and the SAGE estimator can be used to improve the pilot symbol based LS estimator performance. The pilot symbol based LS estimator does not achieve a sufficient throughput with high user velocities when the channel changes frequently between pilot symbols. The throughput increases when the pilot symbol density is decreased and data is transmitted instead of pilot symbols. The SAGE channel estimator compensates for the missing pilot symbols and maintains the improved throughput with lower amount of pilot symbols. The performance and energy efficiency of the channel estimators are summarized in Table 46 with different channels and pilot symbol densities. The energy efficiency is defined as power consumption per correctly received bit. The SAGE estimator has the highest goodput with low pilot symbol density, while the MMSE estimator performs the best in most cases with LTE pilots. The LS estimator has the best energy efficiency in most cases, but the difference in power consumption between the LS and MMSE estimators is small. The SAGE channel estimator would be a good choice for systems where training is performed in the beginning of the transmission. The MMSE estimator performs well in systems with high pilot densities, while the complexity and power consumption are low.

Table 46. The channel estimator with the highest goodput or best energy efficiency.

Channel	Velocity	Highest goodput	Most energy efficient
LTE pilots			
Uncorrelated	50 km/h	MMSE	LS
Winner C1 NLOS	100 km/h	MMSE	MMSE
Mod. corr. TU	50 km/h	SAGE	LS
Mod. corr. TU	100 km/h	MMSE	MMSE
Low pilot symbol density			
Uncorrelated	50 km/h	SAGE	LS
Winner C1 NLOS	100 km/h	SAGE	MMSE
Mod. corr. TU	50 km/h	SAGE	LS
Mod. corr. TU	100 km/h	SAGE	LS

Interference mitigation was considered in Chapter 6. The aim was to mitigate the co-channel interference at the receiver in case no coordinated transmission strategies were in place in the network. The interference and noise spatial covariance matrix measured on the pilot subcarriers was utilized in channel estimation and detection. Without interference mitigation, the performance of the receiver suffers if strong interference is present. An adaptive algorithm was proposed to control the performance and power consumption of the interference mitigation. The algorithm utilizes also noise variance estimation. The algorithm was found to perform well in all scenarios and it can be applied to both linear and nonlinear detection. Implementation results for different interference mitigation algorithms were also provided. All the methods can be implemented at a fairly low cost, but adaptation is required to achieve a good performance in every interference case while obtaining power savings. Finally, detection in an adaptive transmission system, channel estimation and interference mitigation were combined. The performance of the LMMSE and K-best detectors were compared with and without a strong interferer present in the system. Without interference, the same conclusions can be drawn as in Chapter 4: the performances are similar in low SNRs but the K-best detector performs better in high SNRs with higher transmission ranks. When there is interference present, the transmission adaptation does not result in high rank transmissions and the performance of the algorithms do not differ greatly.

One promising topic for further study would be the design and implementation of a reconfigurable overall architecture which would adaptively switch using a simple or a more complex detector depending on the transmission requirements, available SNR, channel properties, etc. This architecture could provide the best performance in all transmission scenarios while minimizing the power consumption. The receiver could be also further optimized for interference scenarios. Also, the combination of detection, channel estimation and interference mitigation from Chapters 4-6 could be optimized to obtain area and power savings. In conclusion, it can be seen that the wireless systems are designed with a simple receiver in mind, but more complex receiver algorithms are still needed to achieve the high data rates in difficult environments. Furthermore, since even higher data rates are planned for the future wireless systems, the use of simple receiver algorithms may not suffice.

References

1. Dahlman E, Parkvall S, Sköld J & Beming P (2008) 3G Evolution HSPA and LTE for Mobile Broadband. Academic Press, 2nd edition.
2. Goldsmith A (2005) Wireless Communications. Cambridge University Press, New York, USA.
3. 3rd Generation Partnership Project (3GPP); Technical Specification Group GSM/EDGE Radio Access Network (2005) Physical layer on the radio path; general description (release 4). Technical report, 3rd Generation Partnership Project (3GPP).
4. De Vriendt J, Laine P, Lerouge C & Xu X (2002) Mobile network evolution: a revolution on the move. IEEE Commun. Mag. 40(4): 104–111.
5. 3rd Generation Partnership Project (3GPP); Technical Specification Group Radio Access Network (2002) High speed downlink packet access: Physical layer aspects (3G TS 25.858 version 5.0.0). Technical report, 3rd Generation Partnership Project (3GPP).
6. 3rd Generation Partnership Project (3GPP); Technical Specification Group Radio Access Network (2004) FDD enhanced uplink; overall description; stage 2 (3G TS 25.309 version 6.1.0). Technical report, 3rd Generation Partnership Project (3GPP).
7. Juntti M, Vehkaperä M, Leinonen J, Zexian V, Tujkovic D, Tsumura S & Hara S (2005) MIMO MC-CDMA communications for future cellular systems. IEEE Commun. Mag. 43(2): 118–124.
8. 3rd Generation Partnership Project (3GPP); Technical Specification Group Radio Access Network (2007) Evolved universal terrestrial radio access E-UTRA; term evolution (lte) physical layer; general description (release 8) TS 36.201 (version 8.0.0). Technical report.
9. 3rd Generation Partnership Project (3GPP); Technical Specification Group Radio Access Network (2006) Requirements for evolved UTRA (E-UTRA) and evolved UTRAN (E-UTRAN) (TR 25.913 version 7.3.0 (release 7)). Technical report, 3rd Generation Partnership Project (3GPP).
10. 3rd Generation Partnership Project (3GPP); Technical Specification Group Radio Access Network (2010) Evolved universal terrestrial radio access E-UTRA; lte physical layer; general description (release 10) TS 36.201 (version 10.0.0). Technical report.
11. IEEE 80216 Broadband Wireless Access Working Group (2010). IEEE 802.16m system description document.
12. Wang F, Ghosh A, Sankaran C, Fleming P, Hsieh F & Benes S (2008) Mobile WiMAX systems: performance and evolution. IEEE Commun. Mag. 46(10): 41 –49.
13. Fu IK, Chen YS, Cheng P, Yuk Y, Y Kim R & Kwak JS (2010) Multicarrier technology for 4G WiMax system [WiMAX/LTE Update]. IEEE Commun. Mag. 48(8): 50–58.
14. Mogensen P, Koivisto T, Pedersen K, Kovacs I, Raaf B, Pajukoski K & Rinne M (2009) LTE-advanced: The path towards gigabit/s in wireless mobile communications. Proc. Int. Conf. on Wireless. Aalborg, Denmark, 147–151.

15. Lunttila T, Kiiski M, Hooli K, Pajukoski K, Skov P & Toskala A (2009) Multi-antenna techniques for LTE-advanced. Proc. Int. Symp. Wireless Pers. Multimedia Commun. Sendai, Japan.
16. Gesbert D, Shafi M, Shiu D, Smith PJ & Naguib A (2003) From theory to practice: An overview of MIMO space-time coded wireless systems. IEEE J. Select. Areas Commun. 21(3): 281–302.
17. Paulraj A, Nabar RD & Gore D (2003) Introduction to space-time wireless communications. Cambridge University Press, Cambridge, U.K.
18. Winters JH, Salz J & Gitlin RD (1994) The impact of antenna diversity on the capacity of wireless communication systems. IEEE Trans. Commun. 42(2/3/4).
19. Bölcskei H (2006) MIMO-OFDM wireless systems: Basics, perspectives, and challenges. IEEE Trans. Commun. 13(4): 31–37.
20. Foschini G (1996) Layered space–time architecture for wireless communication in a fading environment when using multi-element antennas. Bell Labs Tech. J. 1(2): 41–59.
21. Telatar IE (1995) Capacity of multi-antenna Gaussian channels. Technical report, Bell Laboratories. Internal Tech.Memo, pp. 1–28.
22. Wolniansky PW, Foschini GJ, Golden GD & Valenzuela RA (1998) V-BLAST: An architecture for realizing very high data rates over the rich-scattering wireless channel. International Symposium on Signals, Systems, and Electronics (ISSSE). Pisa, Italy, 295–300.
23. Foschini G, Chizhik D, Gans M, Papadias C & Valenzuela R (2003) Analysis and performance of some basic space-time architectures. IEEE J. Select. Areas Commun. 21(3): 303–320.
24. Seshadri N & Winters JH (1993) Two signaling schemes for improving the error performance of frequency-division-duplex (FDD) transmission systems using transmitter antenna diversity. Proc. IEEE Veh. Technol. Conf. Secaucus, USA, 508–511.
25. Tarokh V, Seshadri N & Calderbank AR (1998) Space-time codes for high data rate wireless communication: Performance criterion and code construction. IEEE Trans. Inform. Theory 44(2): 744–765.
26. Alamouti S (1998) A simple transmit diversity technique for wireless communications. IEEE J. Select. Areas Commun. 16(8): 1451–1458.
27. Tarokh V, Jafarkhani H & Calderbank AR (1999) Space-time block codes from orthogonal designs. IEEE Trans. Inform. Theory 45(5): 1456–1467.
28. Rashid-Farrokhi F, Liu KJR & Tassiulas L (1998) Transmit beamforming and power control for cellular wireless systems. IEEE J. Select. Areas Commun. 16(8): 1437–1450.
29. Visotsky E & Madhow U (1999) Optimum beamforming using transmit antenna arrays. Proc. IEEE Veh. Technol. Conf. Houston, TX, vol. 1, 851 – 856.
30. Zheng L & Tse DNC (2003) Diversity and multiplexing: A fundamental tradeoff in multiple-antenna channels. IEEE Trans. Inform. Theory 49(5): 1073–1096.
31. Heath RW Jr & Love D (2005) Multimode antenna selection for spatial multiplexing systems with linear receivers. IEEE Trans. Signal Processing 53(8): 3042–3056.
32. Cavers JK (1972) Variable-rate transmission for rayleigh fading channels. IEEE Trans. Commun. COM-20(1): 15–22.
33. Jungnickel V, Haustein T, Pohl V & von Helmolt C (2003) Link adaptation in a multi-antenna system. Proc. IEEE Veh. Technol. Conf. Jeju, Korea, vol. 2, 862–866.
34. Hayes JF (1968) Adaptive feedback communications. IEEE Trans. Commun. Technol. COM-16(1): 29–34.

35. Goldsmith A & Varaiya P (1997) Capacity of fading channels with channel side information. IEEE Trans. Inform. Theory 43(6): 1986–1992.
36. Goldsmith A (1997) The capacity of downlink fading channels with variable rate and power. IEEE Trans. Veh. Technol. 46(3): 569–580.
37. Catreux S, Erceg V, Gesbert D & Heath RW Jr (2002) Adaptive modulation and MIMO coding for broadband wireless data networks. IEEE Commun. Mag. 40(6): 108–115.
38. Choi YS & Alamouti SM (2008) A pragmatic PHY abstraction technique for link adaptation and MIMO switching. IEEE J. Select. Areas Commun. 26(6): 960–971.
39. Chae CB, Forenza A, Heath RW Jr, McKay MR & Collings IB (2010) Adaptive MIMO transmission techniques for broadband wireless communication systems. IEEE Commun. Mag. 48(5): 112–118.
40. Forenza A, McKay MR, Pandharipande A, Heath RW Jr & Collings IB (2007) Adaptive MIMO transmission for exploiting the capacity of spatially correlated channels. IEEE Trans. Veh. Technol. 56(2): 619–630.
41. Hwang T, Yang C, Wu G, Li S & Ye Li G (2009) OFDM and its wireless applications: A survey. IEEE Trans. Veh. Technol. 58(4): 1673–1694.
42. Chang RW (1966) Synthesis of band-limited orthogonal signals for multichannel data transmission. Bell Syst. Tech. J. 45: 1775–1797.
43. Saltzberg B (1967) Performance of an efficient parallel data transmission system. IEEE Trans. Commun. Technol. 15(6): 805–811.
44. Weinstein SB & Ebert PM (1971) Data transmission by frequency division multiplexing using the discrete Fourier transform. IEEE Transactions on Communication Technology 19(5): 628–634.
45. Cimini LJ (1985) Analysis and simulation of a digital mobile channel using orthogonal frequency division multiplexing. IEEE Trans. Commun. 33(7): 665–675.
46. Chuang J (1987) The effects of time delay spread on portable radio communications channels with digital modulation. IEEE J. Select. Areas Commun. 5(5): 879–889.
47. Wang Z & Giannakis GB (2000) Wireless multicarrier communications. IEEE Signal Processing Mag. 17(3): 29–48.
48. Cooley JW & Tukey JW (1965) An algorithm for the machine calculation of complex Fourier series. Math. Comp. 19(90): 297–301.
49. Duhamel P (1990) Algorithms meeting the lower bounds on the multiplicative complexity of length-2^n DFTs and their connection with practical algorithms. IEEE Trans. Acoust., Speech, Signal Processing 38(9): 1504–1511.
50. Kaiser S (1999) Performance of multi-carrier CDM and COFDM in fading channels. Proc. IEEE Global Telecommun. Conf. Rio de Janeireo , Brazil, vol. 1b, 847–851.
51. Willink TJ & Wittke PH (1997) Optimization and performance evaluation of multicarrier transmission. IEEE Trans. Inform. Theory 43(2): 426–440.
52. Warner W & Leung C (1993) OFDM/FM frame synchronization for mobile radio data communication. IEEE Trans. Veh. Technol. 42(3): 302–313.
53. van de Beek J, Sandell M & Borjesson P (1997) ML estimation of time and frequency offset in OFDM systems. IEEE Trans. Signal Processing 45(7): 1800–1805.
54. Raleigh GG & Cioffi JM (1998) Spatio-temporal coding for wireless communication. IEEE Trans. Commun. 46(3): 357–366.

55. Sampath H, Talwar S, Tellado J, Erceg V & Paulraj A (2002) A fourth-generation MIMO-OFDM broadband wireless system: Design, performance, and field trial results. IEEE Commun. Mag. 40(9): 143–149.
56. IEEE Standard 80216 (2004). IEEE standard for local and metropolitan area networks part 16: Air interface for fixed broadband wireless access systems.
57. Caire G, Ramprashad S, Papadopoulos H, Pepin C & Sundberg CE (2008) Multiuser MIMO downlink with limited inter-cell cooperation: Approximate interference alignment in time, frequency and space. Proc. Annual Allerton Conf. Commun., Contr., Computing. Urbana-Champaign, Illinois, USA, 730–737.
58. Jungnickel V, Schellmann M, Thiele L, Wirth T, Haustein T, Koch O, Zirwas W & Schulz E (2009) Interference-aware scheduling in the multiuser MIMO-OFDM downlink. IEEE Commun. Mag. 47(6): 56–66.
59. 3rd Generation Partnership Project (3GPP); Technical Specification Group Radio Access Network (2011) Feasibility study for further advancements for E-UTRA (LTE-advanced) (release 10). Technical report.
60. Sawahashi M, Kishiyama Y, Morimoto A, Nishikawa D & Tanno M (2010) Coordinated multipoint transmission/reception techniques for LTE-advanced [coordinated and distributed MIMO]. IEEE Wireless Commun. Mag. 17(3): 26–34.
61. 3rd Generation Partnership Project (3GPP); Technical Specification Group Radio Access Network (2010) Evolved universal terrestrial radio access E-UTRA; physical channels and modulation (release 10) TS 36.211 (version 10.0.0). Technical report.
62. Ketonen J, Juntti M & Cavallaro J (2010) Performance-complexity comparison of receivers for a LTE MIMO-OFDM system. IEEE Trans. Signal Processing 58(6): 3360–3372.
63. Ketonen J, Juntti M & Cavallaro JR (2009) Receiver implementation for MIMO-OFDM with AMC and precoding. Proc. Annual Asilomar Conf. Signals, Syst., Comp. Pacific Grove, USA, 1268–1272.
64. Ketonen J, Myllylä M, Juntti M & Cavallaro JR (2008) ASIC implementation comparison of SIC and LSD receiver for MIMO-OFDM. Proc. Annual Asilomar Conf. Signals, Syst., Comp. Pacific Grove, USA, 1881–1885.
65. Ketonen J, & Juntti M (2008) Performance comparisons of SIC and K-best LSD receivers for a MIMO-OFDM system. Proc. Int. Symp. Wireless Pers. Multimedia Commun. Saariselkä, Finland, 1–5.
66. Ketonen J & Juntti M (2008) SIC and K-best LSD receiver implementation for a MIMO-OFDM system. Proc. European Sign. Proc. Conf. Lausanne, Switzerland, 1–5.
67. Ketonen J, Juntti M & Ylioinas J (2010) Decision directed channel estimation for reducing pilot overhead in LTE-A. Proc. Annual Asilomar Conf. Signals, Syst., Comp. Pacific Grove, USA, 1503–1507.
68. Ketonen J, Juntti M, Ylioinas J & Cavallaro J (2012) Decision-directed channel estimation implementation for spectral efficiency improvement in mobile MIMO-OFDM. IEEE Trans. Circuits Syst. I, submitted .
69. Ketonen J, Juntti M, Ylioinas J & Cavallaro JR (2012) Implementation of LS, MMSE and SAGE channel estimators for mobile MIMO-OFDM. Proc. Annual Asilomar Conf. Signals, Syst., Comp., submitted.
70. Ketonen J & Juntti M (2012) Adaptive receiver for co-channel interference suppression in MIMO-OFDM. Signal Processing, Elsevier, submitted .

71. Ketonen J & Juntti M (2012) Receiver implementations for co-channel interference suppression in MIMO-OFDM. Proc. Annual Asilomar Conf. Signals, Syst., Comp., submitted.
72. Lupas R & Verdú S (1989) Linear multiuser detectors for synchronous code-division multiple-access channels. IEEE Trans. Inform. Theory 34(1): 123–136.
73. Golub GH & Loan CFV (1996) Matrix Computations, 3rd ed. The Johns Hopkins University Press, Baltimore.
74. Kay SM (1993) Fundamentals of Statistical Signal Processing: Estimation Theory. Prentice-Hall, Englewood Cliffs, NJ, USA.
75. Vehkaperä M, Tujkovic D, Li Z & Juntti M (2005) Receiver design for spatially layered downlink MC-CDMA system. IEEE Trans. Veh. Technol. 54(3): 1042–1055.
76. Artes H, Seethaler D & Hlawarsch F (2003) Efficient detection algorithms for MIMO channels: A geometrical approach to approximate ML detection. IEEE Trans. Signal Processing 51(11): 2808–2820.
77. Foschini GJ & Gans MJ (1998) On limits of wireless communications in a fading environment when using multiple antennas. Wireless Pers. Commun., Kluwer 6: 311–335.
78. Golden GD, Foschini CJ, Valenzuela RA & Wolniansky PW (1999) Detection algorithm and initial laboratory results using V-BLAST space-time communication architecture. IEE Electron. Lett. 35(1): 14–16.
79. Chin W, Constantinides A & Ward D (2002) Parallel multistage detection for multiple antenna wireless systems. Electronics Letters 38(12): 597 –599.
80. Wübben D, Seethaler D, Jalden J & Matz G (2011) Lattice reduction: A survey with applications in wireless communications. IEEE Signal Processing Mag. 28(3): 70–91.
81. Ma X & Zhang W (2008) Performance analysis for MIMO systems with lattice-reduction aided linear equalization. IEEE Trans. Commun. 56(2): 309 –318.
82. Fincke U & Pohst M (1985) Improved methods for calculating vectors of short length in a lattice, including a complexity analysis. Math. Comput. 44(5): 463–471.
83. Viterbo E & Bouros J (1999) A universal lattice code decoder for fading channels. IEEE Trans. Inform. Theory 45(5): 1639–1642.
84. Schnorr CP & Euchner M (1994) Lattice basis reduction: Improved practical algorithms and solving subset sum problems. Math. Programming 66(2): 181–191.
85. Agrell E, Eriksson T, Vardy A & Zeger K (2002) Closest point search in lattices. IEEE Trans. Inform. Theory 48(8): 2201–2214.
86. Damen MO, Gamal HE & Caire G (2003) On maximum–likelihood detection and the search for the closest lattice point. IEEE Trans. Inform. Theory 49(10): 2389–2402.
87. Anderson J & Mohan S (1984) Sequential coding algorithms: A survey and cost analysis. IEEE Trans. Commun. 32(2): 169–176.
88. Wong K, Tsui C, Cheng RK & Mow W (2002) A VLSI architecture of a K-best lattice decoding algorithm for MIMO channels. Proc. IEEE Int. Symp. on Circuits and Systems. Scottsdale, AZ, vol. 3, 273–276.
89. Mohan S & Anderson J (1984) Computationally optimal metric-first code tree search algorithms. IEEE Trans. Commun. 32(6): 710 – 717.
90. Murugan A, Gamal HE, Damen M & Caire G (2006) A unified framework for tree search decoding: rediscovering the sequential decoder. IEEE Trans. Inform. Theory 52(3): 933–953.

91. Xu W, Wang Y, Zhou Z & Wang J (2004) A computationally efficient exact ML sphere decoder. Proc. IEEE Global Telecommun. Conf. vol. 4, 2594–2598.
92. Zhao W & Giannakis GB (2005) Sphere decoding algorithms with improved radius search 53(7): 1104–1109.
93. Vikalo H & Hassibi B (2006) On joint detection and decoding of linear block codes on Gaussian vector channels. IEEE Trans. Signal Processing 54(9): 3330 –3342.
94. Berrou C, Glavieux A & Thitimajshima P (1993) Near Shannon limit error correcting coding and decoding: Turbo codes. Proc. IEEE Int. Conf. Commun. Geneva, Switzerland, vol. 2, 1064–1070.
95. Hagenauer J, Offer E & Papke L (1996) Iterative decoding of binary block and convolutional codes. IEEE Trans. Inform. Theory 42(2): 429–445.
96. Hagenauer J (1997) The turbo principle: Tutorial introduction and state of the art. Proc. Int. Symb. on Turbo Codes. Brest, France.
97. Bahl LR, Cocke J, Jelinek F & Raviv J (1974) Optimal decoding of linear codes for minimizing symbol error rate. IEEE Trans. Inform. Theory 20(2): 284–287.
98. Tüchler M, Singer A & Koetter R (2002) Minimum mean squared error equalization using a priori information. IEEE Trans. Signal Processing 50(3): 673–683.
99. Wautelet X, Dejonghe A & Vandendorpe L (2004) MMSE-based fractional turbo receiver for space-time BICM over frequency-selective MIMO fading channels. IEEE Trans. Signal Processing 52(6): 1804–1809.
100. Sellathurai M & Haykin S (2002) TURBO-BLAST for wireless communications: Theory and experiments. IEEE Trans. Signal Processing 50(10): 2538–2546.
101. Reed MC (1999) Iterative Receiver Techniques for Coded Multiple Access Communication Systems. Ph.D. thesis, The University of South Australia, Australia.
102. Hochwald B & ten Brink S (2003) Achieving near-capacity on a multiple-antenna channel. IEEE Trans. Commun. 51(3): 389–399.
103. Guo Z & Nilsson P (2006) Algorithm and implementation of the K-best sphere decoding for MIMO detection. IEEE J. Select. Areas Commun. 24(3): 491–503.
104. Wang L, Xu L, Chen S & Hanzo L (2008) Apriori-LLR-threshold-assisted K-best sphere detection for MIMO channels. Proc. IEEE Veh. Technol. Conf. Singapore, 867–871.
105. Studer C, Burg A & Bolcskei H (2008) Soft-output sphere decoding: algorithms and VLSI implementation. IEEE J. Select. Areas Commun. 26(2): 290–300.
106. Mennenga B, Fritzsche R & Fettweis G (2009) Iterative soft-in soft-out sphere detection for MIMO systems. Proc. IEEE Veh. Technol. Conf. Barcelona, Spain.
107. Zhao M, Shi Z & Reed M (2008) The performance of sphere decoders for iterative spatial multiplexing MIMO receiver. Proc. Int. Symb. on Turbo Codes. Lausanne, Switzerland, 113–117.
108. Hagenauer J & Kuhn C (2007) The list-sequential (LISS) algorithm and its application. IEEE Trans. Commun. 55(5): 918 –928.
109. Myllylä M, Juntti M & Cavallaro J (2009) Architecture design and implementation of the increasing radius - list sphere detector algorithm. Proc. IEEE Int. Conf. Acoust., Speech, Signal Processing. Taipei, Taiwan, 553–556.
110. Wübben D, Böhnke R, Kühn V & Kammeyer K (2003) MMSE extension of V-BLAST based on sorted QR decomposition. Proc. IEEE Veh. Technol. Conf. Orlando, Florida, vol. 1, 508–512.

111. Bittner S, Zimmermann E & Fettweis G (2006) Low complexity soft interference cancellation for MIMO-systems. Proc. IEEE Veh. Technol. Conf. Melbourne, Australia, vol. 4, 1993 –1997.
112. Collings I, Butler M & McKay M (2004) Low complexity receiver design for MIMO bit-interleaved coded modulation. Proc. IEEE Int. Symp. Spread Spectrum Techniques and Applications. Sydney, Australia, 1993–1997.
113. Zimmermann E & Fettweis G (2006) Unbiased MMSE tree search detection for multiple antenna systems. Proc. Int. Symp. Wireless Pers. Multimedia Commun. San Diego, USA.
114. Burg A, Haene S, Perels D, Luethi P, Felber N & Fichtner W (2006) Algorithm and VLSI architecture for linear MMSE detection in MIMO-OFDM systems. Proc. IEEE Int. Symp. on Circuits and Systems. Kos, Greece.
115. Khan Z, Arslan T, Thompson J & Erdogan A (2006) Area power efficient VLSI architecture for computing pseudo inverse of channel matrix in a MIMO wireless system. Proc. IEEE Int. Conf. on VLSI Design. Hyderabad, India.
116. Yoshizawa S, Yamauchi Y & Miyanaga Y (2008) A complete pipelined MMSE detection architecture in a 4x4 MIMO-OFDM receiver. Proc. IEEE Int. Symp. on Circuits and Systems. Seattle, USA.
117. Myllylä M, Juntti M, Limingoja M, Byman A & Cavallaro JR (2006) Performance evaluation of two LMMSE detectors in a MIMO-OFDM hardware testbed. Proc. Annual Asilomar Conf. Signals, Syst., Comp. Pacific Grove, USA, 1161–1165.
118. Luethi P, Studer C, Duetsch S, Zgraggen E, Kaeslin H, Felber N & Fichtner W (2008) Gram-Schmidt-based QR decomposition for MIMO detection: VLSI implementation and comparison. Proc. of IEEE Asia Pacific Conference on Circuits and Systems. Macao, 830 –833.
119. Wang JY, Lai RH, Clien CM, Ting PA & Huang YH (2010) A 2×2 - 8×8 sorted QR decomposition processor for MIMO detection. IEEE Asian Solid State Circuits Conference. Beijing, China, 1–4.
120. Huang ZY & Tsai PY (2011) Efficient implementation of QR decomposition for gigabit MIMO-OFDM systems. IEEE Trans. Circuits Syst. I 58(10): 2531–2542.
121. Patel D, Shabany M & Gulak P (2009) A low-complexity high-speed QR decomposition implementation for MIMO receivers. Proc. IEEE Int. Symp. on Circuits and Systems. Taipei, Taiwan, 33–36.
122. Studer C, Fateh S & Seethaler D (2011) ASIC implementation of soft-input soft-output MIMO detection using MMSE parallel interference cancellation. IEEE J. Solid-State Circuits 46(7): 1754 –1765.
123. Garrett D, Davis L, ten Brink S, Hochwald B & Knagge G (2004) Silicon complexity for maximum likelihood MIMO detection using spherical decoding. IEEE J. Solid-State Circuits 39(9): 1544–1552.
124. Chen S, Zhang T & Xin Y (2005) Breadth-first tree search MIMO signal detector design and VLSI implementation. Proc. IEEE Military Commun. Conf. Atlantic City, USA, 1470–1476.
125. Wenk M, Zellweger M, Burg A, Felber N & Fichtner W (2006) K-best MIMO detection VLSI architectutes achieving up to 424 mbps. IEEE Trans. Commun. : 1151–1154.
126. Milliner D & Barry J (2007) A layer-adaptive M algorithm for multiple-input multiple-output channel detection. Proc. IEEE Works. on Sign. Proc. Adv. in Wirel. Comms. Helsinki, Finland, 1 –5.

127. Mondal S, Eltawil A & Salama K (2009) Architectural optimizations for low-power K-best MIMO decoders. IEEE Trans. Veh. Technol. 58(7): 3145–3153.
128. Shen CA & Eltawil A (2010) A radius adaptive K-best decoder with early termination: Algorithm and VLSI architecture. IEEE Trans. Circuits Syst. I 57(9): 2476–2486.
129. Shabany M & Gulak PG (2012) A 675 mbps, 4×4 64-QAM K-best MIMO detector in 0.13 μm CMOS. IEEE Trans. VLSI Syst. 20(1): 135 –147.
130. Shen CA, Eltawil A, Mondal S & Salama K (2010) A best-first tree-searching approach for ML decoding in MIMO system. Proc. IEEE Int. Symp. on Circuits and Systems. Paris, France, 3533–3536.
131. Burg A, Borgmann M, Wenk M, Zellweger M, Fichtner W & Bölcskei H (2005) VLSI implementation of MIMO detection using the sphere decoding algorithm. IEEE J. Solid-State Circuits 40(7): 1566–1577.
132. Radosavljevic P & Cavallaro J (2006) Soft sphere detection with bounded search for high-throughput MIMO receivers. Proc. Annual Asilomar Conf. Signals, Syst., Comp. Pacific Grove, USA, 1175–1179.
133. Yang CH & Markovic D (2009) A flexible DSP architecture for MIMO sphere decoding. IEEE Trans. Circuits Syst. I 56(10): 2301 –2314.
134. Yang T, Yuan J, Shi Z & Reed M (2008) Convergence behavior analysis and detection switching for the iterative receiver of MIMO-BICM systems. IEEE Trans. Veh. Technol. 57(4): 2642–2648.
135. Li M, Bougart B, Lopez E & Bourdoux A (2008) Selective spanning with fast enumeration: A near maximum-likelihood MIMO detector designed for parallel programmable baseband architectures. Proc. IEEE Int. Conf. Commun. Beijing, China, 737 – 741.
136. Amiri K, Cavallaro JR, Dick C & Rao RM (2009) A high throughput configurable SDR detector for multi-user MIMO wireless systems. J Sign. Process. Syst. .
137. Bhagawat P, Dash R & Choi G (2009) Systolic like soft-detection architecture for 4x4 64-QAM MIMO system. Design, Automation and Test in Europe Conference and Exhibition. Nice, France, 870–873.
138. Siti M & Fitz M (2006) A novel soft-output layered orthogonal lattice detector for multiple antenna communications. Proc. IEEE Int. Conf. Commun. Istanbul, Turkey, 1686 –1691.
139. Tomasoni A, Siti M, Ferrari M & Bellini S (2007) Turbo-LORD: A MAP-approaching soft-input soft-output detector for iterative MIMO receivers. Proc. IEEE Global Telecommun. Conf. Washington, DC, USA, 3504–3508.
140. Meyr H, Moeneclaey M & Fechtel SA (1998) Digital Communication Receivers: Synchronization, Channel Estimation and Signal Processing. John Wiley and Sons, New York, USA.
141. Tse D & Viswanath P (2005) Fundamentals of Wireless Communication. Cambridge University Press, Cambridge, UK.
142. Ozdemir MK & Arslan H (2007) Channel estimation for wireless OFDM systems. IEEE Communications Surveys & Tutorials 9(2): 18–48.
143. Shin C, Heath RW & Powers EJ (2007) Blind channel estimation for MIMO-OFDM systems. IEEE Trans. Veh. Technol. 56: 670–685.
144. Zhou S, Muquet B & Giannakis GB (2002) Subspace-based (semi-) blind channel estimation for block precoded space-time OFDM. IEEE Trans. Signal Processing 50(5): 1215–1228.
145. Cavers JK (1991) An analysis of pilot symbol assisted modulation for Rayleigh fading channels. IEEE Trans. Veh. Technol. 40(4): 686–693.

146. Tong L, Sadler BM & Dong M (2004) Pilot-assisted wireless transmissions: general model, design criteria, and signal processing. IEEE Signal Processing Mag. 21(6): 12–25.
147. Hassibi B & Hochwald BM (2003) How much training is needed in multiple–antenna wireless links? IEEE Trans. Inform. Theory 49(4): 951–963.
148. Barhumi I, Leus G & Moonen M (2003) Optimal training design for MIMO–OFDM systems in mobile wireless channels. IEEE Trans. Signal Processing 51(6): 1615–1624.
149. Adireddy S, Tong L & Viswanathan H (2002) Optimal placement of training for frequency selective block–fading channels. IEEE Trans. Inform. Theory 48(8): 2338–2353.
150. Li Y (2002) Simplified channel estimation for OFDM systems with multiple transmit antennas. IEEE Trans. Wireless Commun. 1(1): 67–75.
151. Morelli M & Mengali U (2001) A comparison of pilot-aided channel estimation methods for OFDM systems. IEEE Trans. Signal Processing 49(12): 3065–3073.
152. van de Beek JJ, Edfors O, Sandell M, Wilson S & Borjesson P (1995) On channel estimation in OFDM systems. Proc. IEEE Veh. Technol. Conf. Chicago, IL, USA, vol. 2, 815–819.
153. Edfors O, Sandell M, van de Beek JJ, Wilson S & Börjesson P (1998) OFDM channel estimation by singular value decomposition. IEEE Trans. Commun. 46(7): 931–939.
154. Rinne J & Renfors M (1996) Pilot spacing in orthogonal frequency division multiplexing systems on practical channels. IEEE Trans. Consumer Electron. 42(3): 959–962.
155. Li Y, Cimini LJ & Sollenberger NR (1998) Robust channel estimation for OFDM systems with rapid dispersive fading channels. IEEE Trans. Commun. 46(7): 902–915.
156. Miao H & Juntti M (2005) Space-time channel estimation and performance analysis for wireless MIMO-OFDM systems with spatial correlation. IEEE Trans. Veh. Technol. 54(6): 2003–2016.
157. Zhao M, Shi Z & Reed M (2008) Iterative turbo channel estimation for OFDM system over rapid dispersive fading channel. IEEE Trans. Wireless Commun. 7(8): 3174 –3184.
158. Dempster AP, Laird NM & Rubin DB (1977) Maximum likelihood from incomplete data via the EM algorithm. J. Royal Stat. Soc. 39(1): 1–38.
159. Fessler J & Hero A (1994) Space-alternating generalized expectation-maximization algorithm. IEEE Trans. Signal Processing 42(10): 2664–2677.
160. Xie Y & Georghiades CN (2003) Two EM–type channel estimation algorithms for OFDM with transmitter diversity. IEEE Trans. Commun. 51(1): 106–115.
161. Panayirci E, Şenol H & Poor H (2010) Joint channel estimation, equalization, and data detection for OFDM systems in the presence of very high mobility. IEEE Trans. Signal Processing 58(8): 4225–4238.
162. Ylioinas J & Juntti M (2009) Iterative joint detection, decoding, and channel estimation in turbo coded MIMO-OFDM. IEEE Trans. Veh. Technol. 58(4): 1784–1796.
163. Zou H & Daneshrad B (2004) VLSI implementation for a low power mobile OFDM receiver ASIC. Proc. IEEE Wireless Commun. and Networking Conf. Atlanta, USA, vol. 4, 2120–2124.
164. Haene S, Burg A, Felber N & Fichtner W (2008) OFDM channel estimation algorithm and ASIC implementation. European Conf. Circuits and Systems for Communications. Bucharest, Romania, 270–275.
165. Simko M, Wu D, Mehlfuehrer C, Eilert J & Liu D (2011) Implementation aspects of channel estimation for 3GPP LTE terminals. Proc. European Wireless Conf. Vienna, Austria.

166. Löfgren J, Mehmood S, Khan N, Masood B, Awan M, Khan I, Chisty N & Nilsson P (2009) Hardware implementation of an SVD based MIMO OFDM channel estimator. NORCHIP. Trondheim, Norway, 1–4.
167. Sun MF, Juan TY, Lin KS & Hsu TY (2009) Adaptive frequency-domain channel estimator in 4×4 MIMO-OFDM modems. IEEE Trans. VLSI Syst. 17(11): 1616 –1625.
168. Winters JH (1984) Optimum combining in digital mobile radio with cochannel interference. IEEE J. Select. Areas Commun. 2(4): 528–539.
169. Jeremic A, Thomas TA & Nehorai A (2004) OFDM channel estimation in the presence of interference. IEEE Trans. Signal Processing 52(12): 3429–3439.
170. Dai H, Molisch AF & Poor HV (2004) Downlink capacity of interference-limited MIMO systems with joint detection. IEEE Trans. Wireless Commun. 3(2): 442 – 453.
171. Li Q, Zhu J, Guo X & Georghiades C (2007) Asynchronous co-channel interference suppression in MIMO OFDM systems. Proc. IEEE Int. Conf. Commun. Glasgow, Scotland, 5744–5750.
172. Thomas TA & Vook FW (2003) Asynchronous interference suppression in broadband cyclic-prefix communications. Proc. IEEE Wireless Commun. and Networking Conf. New Orleans, USA, vol. 1, 568–572.
173. Larsson EG (2003) Semi-structured interference suppression for orthogonal frequency division multiplexing. Proceedings of IEEE ISSPIT. Darmstadt, Germany, 435–438.
174. Jöngren G, Astely D & Ottersten B (2000) Structured spatial interference rejection combining. Proc. European Sign. Proc. Conf. Tampere, Finland.
175. Raghavendra M, Juntti M & Myllylä M (2009) Co-channel interference mitigation for 3G LTE MIMO-OFDM systems. Proc. IEEE Int. Conf. Commun. 1 –5.
176. Cavallaro JR & Luk FT (1988) CORDIC arithmetic for an SVD processor. Journal of Parallel and Distributed Computing 5(3): 271–290.
177. Cavallaro J, Keleher M, Price R & Thomas G (1989) VLSI implementation of a CORDIC SVD processor. University/Government/Industry Microelectronics Symposium. Westborough, MA, USA, 256–260.
178. Studer C, Blosch P, Friedli P & Burg A (2007) Matrix decomposition architecture for MIMO systems: Design and implementation trade-offs. Proc. Annual Asilomar Conf. Signals, Syst., Comp. Pacific Grove, CA, USA, 1986–1990.
179. Dickson K, Liu Z & McCanny J (2004) QRD and SVD processor design based on an approximate rotations algorithm. IEEE Workshop on Signal Processing Systems. Austin, TX, USA, 42–47.
180. Ahmedsaid A, Amira A & Bouridane A (2003) Improved SVD systolic array and implementation on FPGA. IEEE Int. Conf. Field-Programmable Technology. Tokyo, Japan, 35–42.
181. Szecowka P & Malinowski P (2010) CORDIC and SVD implementation in digital hardware. Int. Conf. Mixed Design of Integrated Circuits and Systems. Warsaw, Poland, 237–242.
182. Martin G & Smith G (2009) High-level synthesis: Past, present, and future. Design Test of Computers, IEEE 26(4): 18–25.
183. Casseau E, Gal L, Bomel P, Jego C, Huet S & Martin E (2005) C-based rapid prototyping for digital signal processing. Proc. European Sign. Proc. Conf. Antalya, Turkey.
184. Coussy P, Gajski D, Meredith M & Takach A (2009) An introduction to high-level synthesis. Design Test of Computers, IEEE 26(4): 8–17.
185. Fingeroff M (2010) High-Level Synthesis Blue Book. Xlibris Corporation.

186. Cong J, Liu B, Neuendorffer S, Noguera J, Vissers K & Zhang Z (2011) High-level synthesis for FPGAs: From prototyping to deployment. IEEE Trans. Computer-Aided Design of Integrated Circuits and Systems 30(4): 473–491.
187. Myllylä M (2011) Detection algorithms and architectures for wireless spatial multiplexing in MIMO-OFDM systems, vol. C380 of Acta Universitatis Ouluensis, Doctoral thesis.
188. Mentor Graphics (2012). Catapult C Synthesis Overview, Tech. Rep., http://www.mentor.com/esl/catapult/overview.
189. 3rd Generation Partnership Project (3GPP); Technical Specification Group Radio Access Network (2008) Evolved universal terrestrial radio access E-UTRA; physical channels and modulation (release 8) TS 36.211 (version 8.5.0). Technical report.
190. 3rd Generation Partnership Project (3GPP); Technical Specification Group Radio Access Network (2011) Evolved universal terrestrial radio access E-UTRA; multiplexing and channel coding (release 10) TS 36.212 (version 10.3.0). Technical report.
191. Benedetto S, Divsalar D, Montorsi G & Pollara F (1997) A soft-input soft-output maximum APP module for iterative decoding of concatenated codes. IEEE Commun. Lett. 1(1): 22–24.
192. Almers P, Bonek E, Burr A, Czink N, Debbah M, Degli-Esposti V, Hofstetter H, Kyösti P, Laurenson D, Matz G, Molisch AF, Oestges C, & Özcelik H (2007) Survey of channel and radio propagation models for wirelessmimo systems. EURASIP J. Wireless Comm. and Netw. : 1–19.
193. Yu K & Ottersten B (2002) Models for MIMO propagation channels, a review. Wireless communications and mobile computing : 1–14.
194. Kunnari E & Iinatti J (2007) Stochastic modelling of Rice fading channels with temporal, spatial and spectral correlation. IET Communications 1(2): 215–224.
195. Hentilä L, Kyösti P, Käske M, Naradzic M & Alatossava M (2007) MATLAB implementation of the WINNER phase II channel model. Technical report, Available: https://www.ist-winner.org/phase_2_model.html.
196. 3rd Generation Partnership Project (3GPP); Technical Specification Group Radio Access Network (2002) Radio transmission and reception (3G TS 45.005 version 5.4.0 (release 5)). Technical report, 3rd Generation Partnership Project (3GPP).
197. Qiao D, Choi S & Shin KG (2002) Goodput analysis and link adaptation for IEEE 802.11a wireless LANs. IEEE Trans. Mobile Comput." 1(4): 278–292.
198. Robertson P, Villebrun E & Hoeher P (1995) A comparison of optimal and sub-optimal MAP decoding algorithms operating in the log domain. Proc. IEEE Int. Conf. Commun. : 1009–1013.
199. Hassibi B (2000) A fast square-root implementation for BLAST. Proc. Annual Asilomar Conf. Signals, Syst., Comp. Asilomar, USA, vol. 2, 1255–1259.
200. Golub GH & Loan CFV (1989) Matrix Computations, 2nd edn. The Johns Hopkins University Press, Baltimore.
201. Döhler R (1991) Squared Givens rotation. IMA Journal of Numerical Analysis 11: 1–5.
202. Wübben D, Böhnke R, Kühn V & Kammeyer KD (2003) MMSE extension of V-BLAST based on sorted QR decomposition. Proc. IEEE Veh. Technol. Conf. Orlando, Florida, USA, vol. 1, 508–512.
203. El-Amawy A & Dharmarajan K (1989) Parallel VLSI algorithm for stable inversion of dense matrices. Computers and Digital Techniques, IEE Proceedings E 136(6): 575–580.

204. Tüchler M, Singer AC & Koetter R (2002) Minimum mean squared error equalisation using a priori information. IEEE Trans. Signal Processing 50(3): 673–683.
205. Myllylä M, Antikainen J, Juntti M & Cavallaro J (2007) The effect of LLR clipping to the complexity of list sphere detector algorithms. Proc. Annual Asilomar Conf. Signals, Syst., Comp. Pacific Grove, USA, 1559–1563.
206. Parhami B (2000) Computer Arithmetic: Algorithms and Hardware Designs. Oxford University Press, New York, USA.
207. Myllylä M, Juntti M & Cavallaro JR (2007) Implementation aspects of list sphere detector algorithms. Proc. IEEE Global Telecommun. Conf. Washington, D.C., USA, 3915–3920.
208. Sun Y & Cavallaro J (2011) Efficient hardware implementation of a highly-parallel 3GPP LTE/LTE-advance turbo decoder. Elsevier Integration, the VLSI journal 44(4): 305–315.
209. Wübben D, Böhnke R, Rinas J, Kühn V & Kammeyer KD (2001) Efficient algorithm for decoding layered space-time codes. IEE Electronic Letters 37(22): 1348–1349.
210. Sun Y, Zhu Y, Goel M & Cavallaro J (2008) Configurable and scalable high throughput turbo decoder architecture for multiple 4G wireless standards. IEEE Int. Conf. on Application-specific Systems, Architectures and Processors (ASAP). Leuven, Belgium, 209–214.
211. Burg A (2006) VLSI Circuits for MIMO Communication Systems. Ph.D. thesis, ETH Zurich, Switzerland.
212. Ylioinas J, Raghavendra MR & Juntti M (2009) Avoiding matrix inversion in DD SAGE channel estimation in MIMO-OFDM with M-QAM. Proc. IEEE Veh. Technol. Conf. Anchorage, USA, 1–5.
213. 3rd Generation Partnership Project (3GPP); Technical Specification Group Radio Access Network (2003) Spatial channel model for multiple input multiple output (MIMO) simulations (3G TS 25.996 version 6.0.0 (release 6)). Technical report, 3rd Generation Partnership Project (3GPP).
214. Lee J, Lou HL, Toumpakaris D & Cioffi J (2006) SNR analysis of OFDM systems in the presence of carrier frequency offset for fading channels. IEEE Trans. Wireless Commun. 5(12): 3360–3364.
215. Babionitakis K, Manolopoulos K, Nakos K & Chouliaras V (2006) A high performance VLSI FFT architecture. IEEE International Conference on Electronics, Circuits and Systems. Nice, France, 810–813.
216. Chen HY, Ku ML, Jou SJ & Huang CC (2010) A robust channel estimator for high-mobility STBC-OFDM systems. IEEE Trans. Circuits Syst. I 57(4): 925–936.
217. Schäfer F, Stege M, Michalke C & Fettweis G (2003) Efficient tracking of eigenspaces and its application to MIMO-systems. Proc. IST Mobile & Wireless Telecommun. Summit. Aveiro, Portugal.

Book orders:
Granum: Virtual book store
http://granum.uta.fi/granum/

UNIVERSITY OF OULU P.O.B. 7500 FI-90014 UNIVERSITY OF OULU FINLAND

ACTA UNIVERSITATIS OULUENSIS

ISBN 978-951-42-9856-1 (Paperback)
ISBN 978-951-42-9857-8 (PDF)
ISSN 0355-3213 (Print)
ISSN 1796-2226 (Online)

UNIVERSITY of OULU
OULUN YLIOPISTO